Molecular Dissection of the *Shigella* Type III Secretion System Sorting Platform

By

Shoichi Tachiyama
B.Sc., Teikyo University, 2012

Submitted to the graduate degree program in Molecular Biosciences and the Graduate Faculty of the University of Kansas in partial fulfillment of the requirements for the degree of Doctor of Philosophy.

_____

Chair: Dr. William Picking

_____

Co-Chair: Dr. Mark Richter

_____

Co-Chair: Dr. Roberto N. De Guzman

_____

Dr. Josephine Chandler

_____

Dr. C. Russell Middaugh

Date Defended: 29 April 2020

The dissertation committee for Shoichi Tachiyama certifies that this is the approved version of the following dissertation:

Molecular Dissection of the *Shigella* Type III Secretion System Sorting Platform

_____

Chair: Dr. William Picking

Date Approved: 29 April 2020

Abstract

Shigella flexneri is a Gram negative bacterium that invades human intestinal epithelial cells and causes bacillary dysentery (shigellosis). An alarming feature of *Shigella* species is that as few as 10 organisms is a large enough dose to cause disease, and the transmission between humans, especially children, occurs easily by the fecal to oral route or by consumption of contaminated water. Moreover, the CDC has reported increased rates of antibiotic resistance among *Shigella* species and this has complicated treatment strategies. Thus, developing anti-infective strategies that target important virulence factors may be an attractive new treatment strategy. One target for such agents is the type III secretion apparatus (T3SA), so-call injectisome, of *Shigella*. *Shigella* uses its T3SA to contact and directly translocate effector proteins into eukaryotic host cells. These effector proteins then alter host cell functions so that *Shigella* is able to enter and survive within the cytoplasm of intestinal epithelial cells. Because of its central role in *Shigella* virulence, the T3SA is a reasonable target for developing new anti-infective therapeutics, however, to generate such agents it will be important to better understand the architecture and molecular functions of the various moving parts of the T3SA, which is still not completely understood. Recently, cryo-electron tomography (cryo-ET) has revealed the overall architecture of the *in situ Shigella* T3SA, which is now known to be composed of four distinct parts: 1) a cytoplasmic sorting platform (SP) located within the bacterial cytoplasm that participates in the selection of effector proteins and provides the energy needed for translocation; 2) a basal body that spans the bacterium's two membranes and cell wall and upon which the entire T3SA is built; 3) an extracellular needle that is an elongated polymer that extends outward from the basal body; and 4) a needle tip complex that makes contact with the host cell and is needed for insertion of a translocon pore within the

host membrane. A prominent feature of the SP are pod-like structures that are present with an evenly spaced six-fold symmetry. Each pod is connected to a centrally located ATPase called Spa47 via radial spokes consisting of a protein called MxiN. Directly above the hexameric Spa47 ATPase is MxiA, which forms the export gate for the effector protein secretion. The Spa47 and MxiA complexes are associated with a connecting Spa13 stalk. The pod structures associate with the cytoplasmic portion of the basal body via the cytoplasmic domain of MxiG (here called $MxiG^{Cyt}$). Along with MxiJ, MxiG forms the inner membrane ring (IR) of the basal body. The periplasmic domain of MxiG ($MxiG^{Peri}$) has a densely packed 24-fold symmetry with the smaller $MxiG^{Cyt}$ having a less densely packed but evenly spaced 24-fold symmetry. It is anticipated that the symmetry transition between $MxiG^{Cyt}$ and the pods has an important role in the dynamic mechanisms responsible for secretion, however, to dissect this process, we need to generate a deeper understanding of the protein components of the pod structures and the structural features that guide their interactions.

The positions of Spa33 and MxiN within the SP have been determined using cryo-ET, however, the protein MxiK is known to be part of the SP, but its location within this complex has not yet been determined. We hypothesize that MxiK occupies a density near the IR where it acts as an adaptor between $MxiG^{Cyt}$ (basal body) and the Spa33 density of the SP pods. To localize the position of MxiK, we generated a library of bacteriophage T4 lysozyme (T4L) insertion mutants of MxiK for functional and structural analysis. Many of these insertion mutants continue to be active in restoring type III secretion to a *Shigella mxiK* null mutant and one of these (MxiK-T4L-C) was used for cryo-ET studies to observe where the additional electron density from T4L appeared within the SP. Identification of the T4L density helped us to confirm the position of MxiK as being within the pod component that forms the interface with $MxiG^{Cyt}$. Moreover, the

MxiK electron density suggested it is either lobed or possibly has two domains. To confirm the position of MxiK within the SP (between Spa33 and $MxiG^{Cyt}$), the SP interactome was determined using a bacterial adenylate cyclase two-hybrid (BACTH) system with the identified interactions confirmed, when possible, using Biolayer Interferometry (BLI). Both approaches indicated that MxiK's binding partners are $MxiG^{Cyt}$ and Spa33, with the latter being the dominant component of the pod structures. Spa33, in turn, interacts with MxiN. Here I will combine all of the available *in vivo, in vitro,* and *in situ* data to provide a definitive description of the architecture of the *Shigella* T3SA sorting platform.

The pod structures that make up the *Shigella* T3SA sorting platform are now proposed to be composed of a single copy of MxiK and a heterotrimeric Spa33 complex with both MxiK and Spa33 being essential for the assembly and stability of the overall SP structure. Consistent with this, cryo-ET images of the T3SA formed by a *mxiK* null *S. flexneri* strain completely lacks the entire SP and all of the extracellular components of the T3SA. These data indicate that MxiK is key component of the pods and is required for pod assembly as it forms the IR-SP interface. Thus, we propose that disruption of MxiK interactions with $MxiG^{Cyt}$ or Spa33 are potential targets for new T3SA-targeting anti-infective agents. In this investigation, we identify the molecular basis for interactions between Spa33 and MxiK, as well as between MxiK and $MxiG^{Cyt}$, using both insertional and site-directed mutagenesis. From the MxiK-T4L insertion and Ala substitutional mutant libraries, two regions of MxiK completely disrupted the type III secretion system (T3SS) activities and these disruptions were not due to protein misfolding based on circular dichroism (CD) spectroscopy data. Subsequent BACTH analysis for these mutations revealed that both regions of MxiK are essential for the MxiK interactions in the SP.

In parallel experiments, we investigated the structural bases for MxiK binding to MxiG^{Cyt}. Based on the MxiG^{Cyt} structure, this protein is a β-rich forkhead-associated (FHA) domain. Canonical FHA domains recognize phosphorylated threonine residues to promote specific protein-protein interactions, however, a previous study and work presented here show that while MxiG^{Cyt} is involved in protein-protein interactions, this does not occur via phosphothreonine recognition. In fact, when we introduced a continuous string of Ala residues into the MxiG^{Cyt} 61-66 loop together with Ala residues in the 81-85 loop region, we found that MxiG^{Cyt} interactions with MxiK were eliminated and *Shigella* hemolytic activity was lost. As importantly, cryo-ET analysis showed that while this mutation allowed for T3SA basal body formation, it did not allow for SP assembly or formation of the extracellular needle. These data suggest that MxiG interacts with MxiK via loop regions on its MxiG^{Cyt} domain and the loss of this interaction gives rise to a *mxiG* null mutation phenotype. In this investigation, we demonstrate the position of all major SP components using cryo-ET with confirmatory biochemical analyses. Our next goal will be to determine high-resolution protein structures for these components such as MxiK and MxiN. Such structures are not available for most of the SP components. This information will be needed to rationally design new anti-infective agents.

Acknowledgements

I would like to thank my two mentors, Dr. William Picking and Dr. Wendy Picking. Dr. William Picking gave me a lot of grateful advice and encouragement for not only my project, but also for becoming a successful researcher. Moreover, he supported the preparation of my presentations in local and international conferences as well as in the Department of Molecular Biosciences program at the University of Kansas. In our laboratory meetings, Dr. Wendy Picking gave me insightful suggestions to solve my experimental problems, and she supported and provided helpful instruments to use and useful materials for this PhD work. I could spend an enjoyable and grateful time in the Picking's lab, and I will never forgot this precious time in my life.

I sincerely appreciate Dr. Jun Liu and Dr. Chang Yunjie in Department of Microbial Pathogenesis at Yale School of Medicine for visualizing the *Shigella* type three secretion apparatus using cryo-ET techniques. My PhD work would have never been successful without this collaboration work about their *in situ* experiments. I would also like to thank my committee members, Dr. Josephine Chandler, Dr. Roberto De Guzman, Dr. Mark Richter, and Dr. C. Russell Middaugh. All of my committee members gave me warm encouragement in every committee meeting. Moreover, I would like to appreciate Dr. Scott Lovell in Protein Structure Laboratory at the University of Kansas and Dr. Minli Xing in the NMR Laboratory at the University of Kansas. Both structural biologists gave me a lot of constructive comments for the protein crystal screening and NMR experiments.

In the Picking laboratory, I obtained generous support and constructive advice for my PhD work from all the laboratory members. Dr. Meenakumari Muthuramalingam and Qi Zheng gave me a lot of advice to solve many experimental problems in my projects. Sierra Walton who is an undergraduate student in Picking's laboratory had prepared most of the common chemical stocks, and my research data in here have been supported by her assistance. I would also like to acknowledge former laboratory members, especially Dr. Michael Barta who taught me the background for this MxiK project and helped with the biophysical experiments and taught me protein purification and Dr. Olivia Arizmendi who explained and showed me important *Shigella* assays in this investigation.

Lastly, I really would like to thank my parents. My parents had financially supported to enter the Molecular Biosciences program and gave me a lot of encouragement to complete this valuable academic career. I also would like to thank my sister who introduced me to Kansas and the University of Kansas after completion of my prior degree. Again, my PhD work would not have been successful without all of these supports.

Table of Contents

List of Figures

List of Table

Chapter 1 Introduction

1.1 *Shigella*

During a 19th century epidemic of dysentery in Japan, the Japanese microbiologist, Dr. Kiyoshi Shiga, identified an etiologic microbe as the cause of the outbreak. In Japanese, the term for dysentery is *sekiri* which means the red diarrhea, which describes one of the symptoms (bloody diarrhea) of the infection. At the time, Dr. Shiga had isolated and characterized the microbe from stool, and he named it *Bacillus dysenteriae* (1). Later, other investigators identified similar organisms, and the genus name was changed to *Shigella* in the 1930 edition of *Bergey's Manual of Determinative Bacteriology* (2). Dr. Shiga also found that the microbe produces toxins that contribute to the symptoms of dysentery. These toxins are now called Shiga toxins. *Shigella* and its bacterial products have now been examined and characterized for more than 100 years (1,2).

Shigella spp. are members of the Gram-negative *Enterobacteriaceae* that cause bacillary dysentery (shigellosis). *Shigella spp.* are classified into four subgroups, and each subgroup has serotypes based on the O-antigen structure of its lipopolysaccharide (LPS): subgroup A is *Shigella dysenteriae* which has 15 serotypes; subgroup B is *S. flexneri* that has 14 serotypes; subgroup C *is S. boydii* that has 20 serotypes; subgroup D is *S. sonnei* that has a single serotype (3). According to the CDC, 80-165 million patients are infected annually by *Shigella* with up to 600,000 patients succumbing to the illness (4). People in developing countries, especially Africa and South Asia, are at especially high risk for shigellosis with *S. flexneri* being the dominant species. Although the U.S. is highly developed (industrialized) with numerous public health measures in place, almost a half million people can be expected to contact shigellosis annually with almost 75% of the cases caused by *S. sonnei* and 12% caused by *S. flexneri* (5). In addition to these four *Shigella* species,

antibiotic resistant species have been recently reported with increasing frequency. Traditionally, ampicillin and trimethoprim-sulfamethoxazole are first choice antibiotics to treat *Shigella* infections, however, the National Antimicrobial Resistance Monitoring System for Enteric Bacteria (NARMS) and CDC have reported that a high number of *Shigella* isolates are now harboring resistance to these antibiotics (6,7). Ciprofloxacin and azithromycin are alternative medicines for the treatment of the infection, but some cases of *Shigella* infections show resistance to these antibiotics. The numbers of antibiotic resistant *Shigella* isolates continue to increase each year (6,7). Therefore, new antibiotics are needed for the treatment of *Shigella* infections.

Based on phylogenetic analyses, *Shigella* is known to have evolved as a group within the *Escherichia coli*, which have adapted to growth within the intracellular environment of human cells (8). Interestingly, the pathogen does not express common adhesion proteins, does not generate flagella for bacterial motility, and it lacks the proteins expected to be needed for forming biofilms (9). On the other hand, *Shigella* carries a very large (almost 200 kb) virulence plasmid that encodes nearly all of the proteins needed for its pathogenesis (8). Importantly, proteins for a type III secretion apparatus (T3SA) and effector proteins that alter host cell functions are encoded within a 31 kb entry region on this plasmid (8). Expression of these genes is regulated by proteins encoded on the chromosome and these are, in turn, regulated by environmental factors such as temperature and osmotic changes (9). For instance, once inside the human body, *Shigella* is exposed to an elevated temperature and the osmolarity of the gastrointestinal tract. This environmental change results in the expression of VirF which induces VirB expression (8). VirB then induces the expression of other regulators to enhance expression of virulence effector and T3SA genes (9). In addition to the T3SS, the virulence plasmid also encodes proteins such as SepA

and IcsA, which are part of the type 5 (autotransporter) secretion system (T5SS) (3). These plasmid-encoded proteins contribute to and are important for the pathogenesis of shigellosis.

1.2 Pathogenesis

Shigellosis is one of the common foodborne illnesses and it is characterized by diarrhea with blood, fever, and stomach cramps over several days. *Shigella* contaminated food and water are common infection sources. Since a small number of organisms is capable of causing this disease (10), *Shigella* infections spread quickly by fecal to oral transmission, especially among children. After *Shigella* enters the human body, there are four main steps in its pathogenesis; uptake into the submucosa region, invasion of intestinal epithelial cells, replication in the host cell, and direct spreading into adjacent cells (Fig. 1.1) (8).

In the human body, *Shigella* reaches the stomach first. This organ provides a rigorous acidic environment that contributes to what can be referred to as the chemical immune system, however, *Shigella* expresses periplasmic proteins that provide acid resistance for survival within the stomach (8,9,11). This is probably why a low dose of the organisms is sufficient to cause this disease. Next, *Shigella* passes through the small intestine, possibly with the help of poorly characterized *Shigella* enterotoxins called ShET-1 and ShET-2 (12), and reaches and colonizes the thick mucus layer of the colon where a low oxygen environment leads to regulation of the fumarate-nitrate regulator (FNR). FNR regulates expression for the *Shigella* type III secretion system (T3SS) genes (3,9,13). To cross the intestinal epithelial barrier, *Shigella* induces cytoskeletal rearrangements within microfold or M-cells so that *Shigella* is introduced to the submucosa. Although other invasion pathways have been reported recently, the M-cell associated

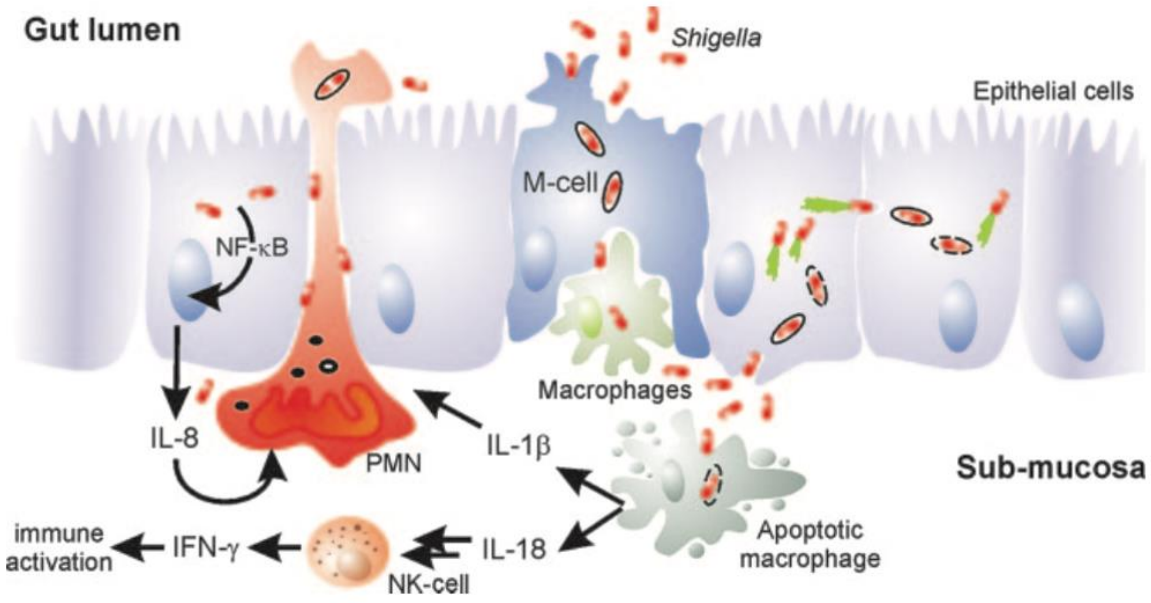

Figure 1.1. Pathogenesis of *Shigella* species.

This figure illustrates the overall pathogenesis of *Shigella* species. *Shigella* is taken up into the sub-mucosa region via M-cells, then the pathogens stimulate apoptosis in macrophages to survive at this region. Surviving *Shigella* alter the actin cytoskeleton in epithelial membrane to enter these host cells. Alteration of cytoskeleton is then used for motility in epithelial cells. Apoptotic macrophages produce cytokines to induce inflammation that cause disruption to the mucosa.

This figure is from Gunnar. N. Schroeder et al. [2008] Clinical Microbiology Reviews 21:134-56.

pathway is thought to be the primary one for initial *Shigella* invasion of the colonic epithelium (14). In this pathway, *Shigella* is transcytosed across the epithelial cell layer and released at the intraepithelial pocket which is a macrophage-rich region. At this point, *Shigella* induces macrophage cell death as part of a strategy to avoid the host innate immune system and to enable it to remain free within the submucosal region (Fig. 1.1) (8). After escaping from macrophages, *Shigella* makes contact with host epithelial cells on their basal side via the T3SA and delivers effector molecules to trigger cytoskeletal changes that let the pathogen enters these intestinal cells. Previous studies showed that components of lipid rafts on the host cell membranes are targets for the initial adherence and for triggering bacterial entry (15). Secreted T3SS proteins such as IpaC and VirA are responsible for the actin rearrangement and microtubule destabilization. This promotes host cell membrane ruffling and is an initial step of bacterial entry (16-18). *Shigella* immediately lyses the resulting phagocytic vacuolar membrane to release the bacterium into the host cytoplasm (8,19).

Once in the cytoplasm of the epithelial cell, *Shigella* cells is protected from the host immune response and this is where bacterial replication will occur (8). However, *Shigella* also needs to protect itself from innate immune responses while in its intracellular niche. For example, autophagy is how a host cell might eliminate unwanted components from the cytoplasm so that a cell can maintain homeostasis. Misfolded proteins and microbes in the eukaryotic cell cytoplasm, for instance, are carried into lysosome which contain enzymes for degradation processes (20). To escape from the host autophagy systems, *Shigella* secretes IcsB and VirG from T3SS (8,21). VirG is an effector protein that forms a complex with Atg5 of the host cell. Since this complex potentially induces autophagy, IcsB interacts with VirG to inhibit formation of the VirG-Atg5 complex (22). Therefore, IcsB is required to block the autophagy system and allow survival in the

host cytoplasm (22). After escaping from autophagy, *Shigella* migrates within the host cytoplasm. For intracellular migration/motility, the microbe induces host actin rearrangement at one pole of the bacterium (noting that *Shigella* does not possess flagella). Previous *in vitro* experiments have shown that an outer membrane protein, IcsA (also called VirG), alters host cell signals to activate the Arp2/3 actin nuclear complex for the rearrangement (8). Moreover, one of the effector proteins from the T3SS, VirA, acts as cysteine protease to degrade α-tubulin to cause microtubule destabilization, which contributes to the bacterial intracellular motility and spreading into adjacent cells (8,23).

In establishing the infection, *Shigella* must initially overcome extracellular components of the host innate immune responses, as well. At the subepithelial dome of colonic lymphoid follicles, macrophages are poised to engulf invading bacteria to digest them and present them to the adaptive immune system (Fig. 1.1) (8). This would prevent the *Shigella* invasion of the epithelial layers and submucosa. To survive this attack by the innate immune system, *Shigella* has evolved specific defense mechanisms, including the use of secreted effector proteins (secreted via the T3SS) that induce programmed macrophage death following ingestion of the bacterium. For instance, IpaB, which is a key effector and translocator protein secreted by the T3SS, binds to and activates caspase-1 to cause macrophage death (24). In addition to this function, IpaB forms integral oligomers in the phagosomal membrane within the macrophage to cause the destabilization of these eukaryotic cell membranes. Destabilization of the membrane furthers induces the inflammasome to activate caspase-1 that leads the macrophage death (25). Other types of macrophage death caused by *Shigella* infection have also been reported, so IpaB is not the only *Shigella* component that can lead to macrophage death. A second T3SS secreted protein, IpaD, has been demonstrated to cause macrophage apoptosis via caspase-mediated pathways that elicit

mitochondrial damage (26). Furthermore, bacterial components such as LPS and LPS-derived lipid-A can also cause the macrophage death via caspase-1 independent pathways (27). This type of macrophage killing is usually related to post-inflammatory events caused by the macrophage due to the release of several proinflammatory cytokines such as IL-1β (27). Another result of the eventual inflammation caused by *Shigella* infection is the transmigration of polymorphonuclear leukocytes (PMN) or neutrophils across epithelial tight junctions. This post-inflammatory events facilitate additional *Shigella* entry into the submucosa region (28,29). Ultimately, these inflammatory events lead to major tissue damage and thus they not only are related to *Shigella* survival, but they also give rise to the symptoms of shigellosis (8).

1.3 *Shigella* Type III secretion system and its architecture

As described above, the *Shigella* T3SS injectisome is the primary factor required for *Shigella* pathogenesis. Proteins for the T3SA, and most of the effector proteins that are secreted by it, are encoded within the entry region of the large virulence plasmid (8). The effector proteins are directly translocated via the T3SA into eukaryotic cells to alter host cell functions as an essential step in establishing *Shigella* infection. Because the injectisome represents a unique protein nanomachine found in important Gram-negative bacterial pathogens, it is thought to be one possible target for new anti-infective therapeutics. Despite the T3SS's contributions to *Shigella* pathogenesis, its functions and the structures for the proteins in the T3SA are still poorly understood. One reason for this is that the T3SA is a relatively complex protein assembly that spans the bacterial envelop (two cell membranes and a cell wall), which makes it difficult to visualize the detailed architecture and protein structures without new technologies such as high-resolution electron microscopy.

In the late 1990's, first direct observation of the T3SA from *Salmonella typhimurium* was reported using electron microscopic techniques. It was found to have a cylindrical and symmetrical structure imbedded in the inner and outer bacterial membranes (30). Later, the *Shigella* T3SA was also observed using electron microscopy techniques. Electron microscopy had finally allowed visualization of the architecture of *Shigella* T3SA, however, viewing the injectisome required its extraction from the bacterium (31). Thus, the cytoplasmic components that only loosely associate with the envelope-spanning injectisome could not be observed at that time. Because of this, the injectisome was only roughly described as having three main parts, including an envelope-spanning component (the basal body), an external needle with associated tip complex, and a cytoplasmic "bulb" (Fig. 1.2) (8,31). The basal body is associated with the inner- and outer membranes and crosses the cell wall via a series of ring structures. The outer membrane ring that is almost 130 Å in diameter with a 115 Å height, and the inner membrane ring is almost 220 Å in diameter and 112 Å height (32). The total height of the complete basal body is approximately 300 Å (32). The needle is made of a small protein (around 10 kDa), MxiH, that is not homologous to sequences found within the related flagella T3SS (33). The needle is a helical polymer of MxiH, and its size is almost 500 Å in length with a 70 Å diameter (33-35). The needle has an inner channel through which effector proteins pass through to host cells. This channel is approximately 20 Å diameter (33-35). At end of the needle, invasion plasmid antigen (Ipa) proteins secreted from the bacterial cytoplasm via the apparatus form what is called the tip complex, which contacts and ultimately forms a translocon pore within the host cell membrane (Fig. 1.2) (8). The maturation process for the *Shigella* tip complex was first described by the Picking laboratory. First, IpaD associates with MxiH and forms a pentamer at the needle tip where it prevents premature translocation of effector proteins (36,37). When the IpaD oligomer makes contact with small

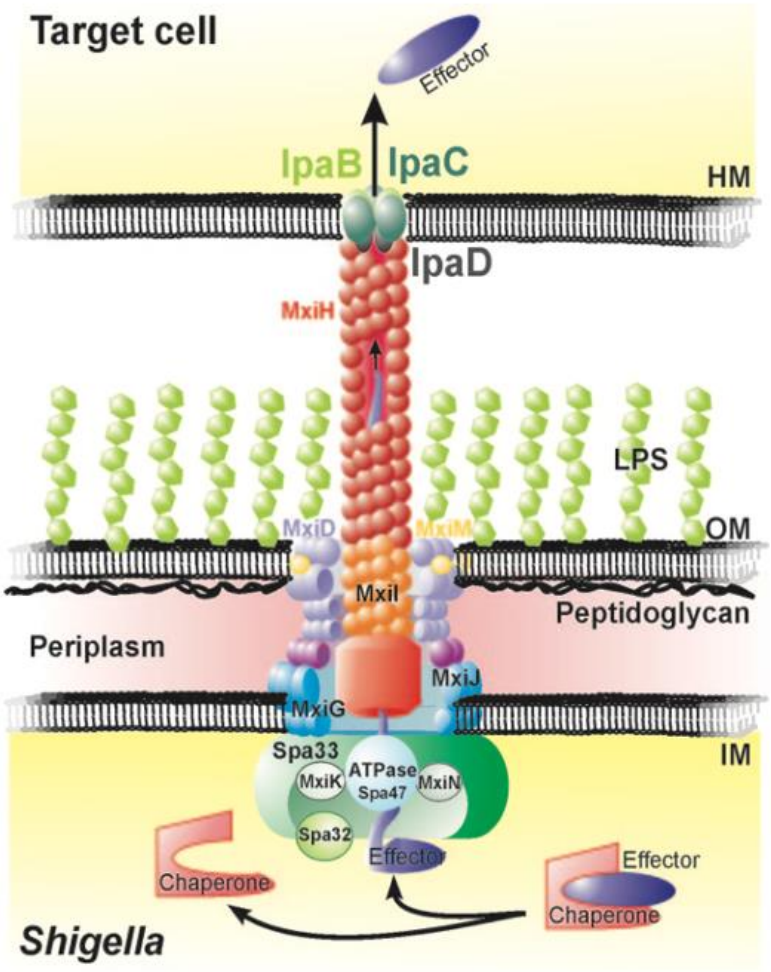

Figure 1.2. Architecture of T3SS.

This is a cartoon to illustrate the architecture of T3SS. T3SA had been thought to be composed of mainly three parts; the envelope spanning basal body (MxiG, MxiJ, MxiD, and MxiM), the needle (MxiH and MxiI) with the tip complex (IpaB, IpaC, and IpaD), and the cytoplasmic bulk (MxiK, MxiN, Spa32, Spa33, and Spa47). Since the cytoplasmic side of T3SA had not been observed using electron microscopy, an architecture of this part was not clear.

This figure is from Gunnar. N. Schroeder et al. [2008] Clinical Microbiology Reviews 21:134-56.

compounds present in the host gastrointestinal tract such as bile salts, the conformation of IpaD is altered and this results in the recruitment of a second tip protein, IpaB, to the needle surface (36,38,39). IpaB is the first true translocator protein to be presented at the needle tip. IpaB subsequently recruits IpaC to be secreted once it makes contact with the host cell membrane so that the mature translocon pore can be formed as a channel in the host membrane to allow effector injection into the host cell (40,41). Recent *in vitro* studies suggest that this translocon on the host membrane forms 30 to 50 Å diameter pores that allow effector proteins to pass through into the host cytoplasm (40,42). Hence, IpaD (and probably IpaB) probably acts as a sensor of host cell contact, and then IpaB and IpaC are required to create a pore in the host cell membrane for effector protein delivery.

1.4 Cytoplasmic sorting platform of the *Shigella* type III secretion system

Prior to this work, the detailed architecture of the cytoplasmic portion of the T3SA had not been observed because purification of the T3SA from *S. flexneri* using osmotic shock results in a T3SA injectisome preparation lacking the cytoplasmic components remaining as part of the complex. To overcome this problem, Hu and coworkers used a plasmid, pBS58, which over-expresses the *E. coli* cell division genes *ftsQ, ftsA*, and *ftsZ* to cause asymmetric bacterial cell division, thus producing "mini-cells (43-45)." The *in situ* T3SA present within these very small (approximately 200 nm) mini-cells possesses the bacterial cytoplasmic components of the injectisome, thereby allowing us to visualize the T3SA complete architecture (Fig. 1.3A) (45). Moreover, the use of high-throughput cryo-electron tomography (cryo-ET) with subtomogram averaging made it possible to observe high resolution (~3 nm resolution) images for the cytoplasmic assembly (45). The cytoplasmic side of T3SA is called cytoplasmic sorting platform

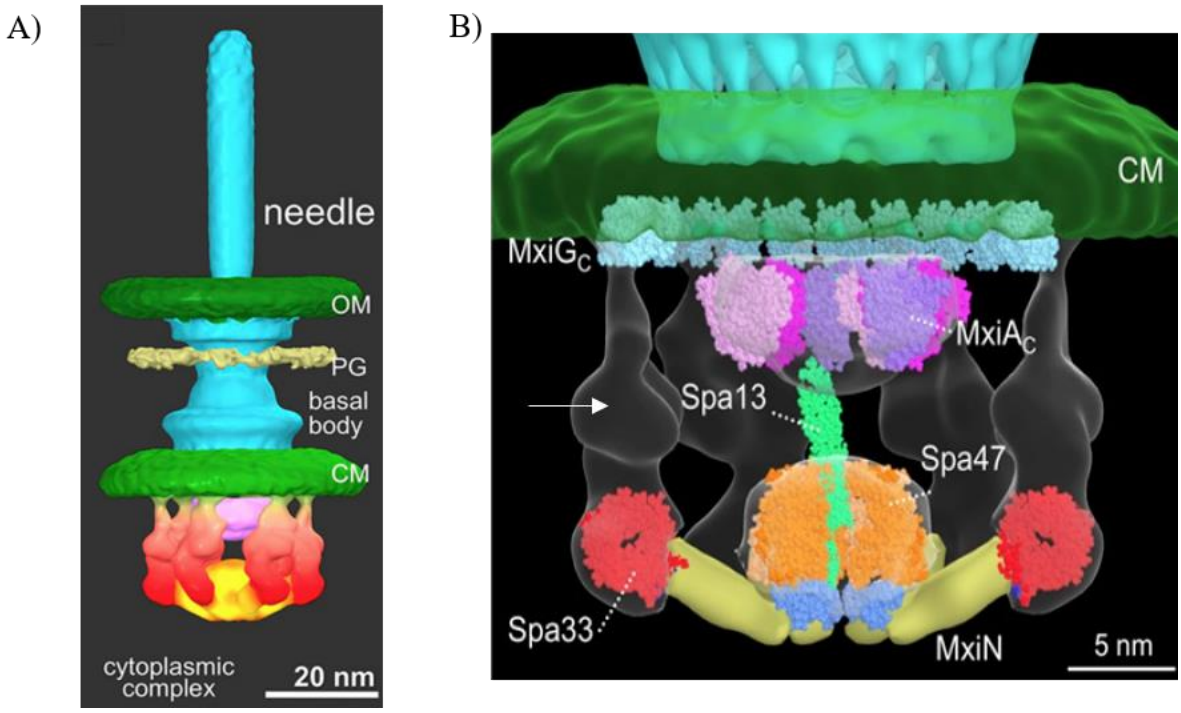

Figure 1.3. Surface rendering images of T3SA and its cytoplasmic sorting platform.

A) A 3D surface rendering image of T3SA from cryo-ET. T3SA in mini-cells allows us to visualize its cytoplasmic side, which called the cytoplasmic sorting platform (SP). B) This is an image of the SP part. Hu at el. used different information such as X-ray structures, homologous architecture, and evolutional information to localize cytoplasmic proteins into this image. The arrow indicates the hypothesized location of MxiK based on our preliminary data.

(This image is from B. Hu et al., [2015] PNAS 112:1047-52)

(SP), and its overall size is approximately 320 Å in diameter and 240 Å in height (45).The SP associates with the cytoplasmic exposed portion of the basal body inner membrane ring. The SP is made up of pod-like structures that are observed an immediately beneath the bacterial inner membrane (Fig. 1.3B). At the bottom part of the SP, each pod structure associates with a central hub using radial spoke-like structures (Fig. 1.3B) (45).

The architecture of the related bacterial flagella T3SSs shares many of the structural features of the *Shigella* T3SA SP, and this has allowed us to localize some protein components and tentatively assign functions within the SP. Based on the architecture of the flagella export apparatus, the Spa47 hexamer position is located on the central hub at bottom part of the SP (45,46). Recent *in vitro* experiments suggest that Spa47 (the central hub) has ATPase activity that is essential for *Shigella* pathogenesis by providing the energy needed for T3SS activities such as driving translocation and/or removing chaperones from effector proteins prior to their secretion (47-50). Association with cytoplasmic chaperones is a common theme for proteins to be secreted by the T3SS. IpaB and IpaC, for instance, bind with the chaperone IpgC in the bacterial cytoplasm which prevents their premature export (41). To pass through the basal body and needle, both proteins need to be separated from IpgC, which remains in the cytoplasm. It is believed that the energy from the Spa47 ATPase is used for this process (48,51). IpaB and IpaC may then be partially unfolded so that they are able to migrate to the tip complex, form the translocon, and elutes host cells via the 2.0 nm diameter inner channel of the translocon (51,52). The N-terminus of Spa47 interacts with a homo dimer of MxiN with the latter then forming the spoke-like structures at the bottom of the SP. A recent study showed that MxiN acts as a regulator of Spa47 enzymatic activity (53). Spa47 also connects with the export gate channel protein, called MxiA, of the basal body via the Spa13 stalk protein (45). Although the translocation mechanisms for the

virulence effector proteins by the SP are still unclear, functions of the flagella system suggest that SP uses both ATPase activity and the proton motive force for protein selection and secretion processes (54,55).

Outside of the central hub and beneath the bacterial inner membrane, pod-like structures form with a six-fold discontinuous symmetry that is analogous to but distinct from the C-ring in the flagella type III secretion apparatus. Each pod connects with Spa47 via MxiN at the bottom part of the SP (45). The top part of each pod interfaces with the cytoplasmic side of the inner membrane ring in the basal body. In 2015, Hu et al. tried to piece together the protein components of the SP using high-resolution structures from homologous proteins to dock into electron densities obtained using cryo-ET. All SP components or homologs except for the pod structures had been determined at that time (45). Since the Spa33 homologue is the flagella C-ring complex, formed by FliN and FliM, which is localized beneath the cytoplasmic side of the flagella inner membrane ring, Spa33 was presumed to be one component of the pod-like structures, however, the precise makeup of the pods is still unclear due to the absence of structural information (45). It is important to understand this unknown region because it is key for SP functions. Also, the pods are known to form an interface with the cytoplasmic domain of the basal body inner-membrane ring protein, MxiG, (the cytoplasmic domain of MxiG is called $MxiG^{Cyt}$), which has major mechanistic implications (45).

As part of the basal body, MxiG crosses the bacterial cytoplasmic membrane as part of the inner membrane ring, along with MxiJ, having a continuous 24-fold symmetry (56). The smaller MxiG cytoplasmic domain also has 24-fold symmetry on the cytoplasmic side of the inner membrane, but it is not as tightly packed as the periplasmic domain (57). In contrast to the symmetrical structure of MxiG, the SP pods form a six-fold symmetrical discontinuous structure

rather than a true ring (45). Since two different symmetrical structures create the interface between the basal body and SP, the unknown regions within the pods that interface with MxiG^{Cyt} are proposed to have an important role in T3SS dynamics and function. In fact, a *spa33* null *Shigella* mutant is not able to form a functional T3SS and it lacks the entire SP and the external needle as seen by cryo-ET imaging (45). In contrast, a *mxiN* null *Shigella* strain is also nonfunctional, however, it only lacks the central hub, stalk and radial spokes (Spa47, Spa13 and MxiN) within the SP with remnants of the pods still visible (45). These mutagenesis and the cryo-ET experiments have laid the foundation for better describing the associations within the intact SP with the inner-membrane ring, an association that is required for the translocation of needle proteins and translocator proteins for generating a fully functional T3SS (45). To better understand how this symmetry transition between the pod structures and the inner-membrane ring contributes to T3SS structure and function, the MxiG^{Cyt} binding partner present within the unknown densities in the SP needs to be identified and this interaction characterized. One of the candidate proteins that is a known pod component, but whose position is not known, is MxiK. Its position has not been determined in previous cryo-ET studies. Although the MxiK position is still unclear, preliminary experiments suggest that this protein contributes to SP assembly and T3SS functions because a cryo-ET image of the *in situ* T3SA from a *mxiK* null *Shigella* strain shows same architecture as the T3SA from the *spa33* null strain (45). Unfortunately, structural information for MxiK and its homologous proteins in the SctK family are not described because these proteins tend to be difficult to purify from *E. coli* expression strains. This makes it difficult to characterize SctK family proteins.

1.5 Structural details for MxiG and Spa33

The basal body is embedded within the two bacterial membranes and the periplasmic cell wall. The inner membrane ring of the basal body is formed in part by MxiG, which has transmembrane helix that connects its periplasmic domain with the cytoplasmic domain that forms an interface with the pod structures of the SP. A top view of cryo-ET images revealed that the inner membrane ring directly overlays with the pod structures beneath (57). MxiG spans the bacterial cytoplasmic membrane and has a continuous 24-fold symmetry with its three domains – the N-terminal domain (residues 1 – 126) that is the cytoplasmic domain ($MxiG^{Cyt}$) and is located on the cytoplasmic side of the inner membrane, a transmembrane helix, and a periplasmic domain (56). Based on previous studies for *Salmonella typhimurium* T3SA, the cytoplasmic domain is believed to be flexible due to a linker to the transmembrane helix which, potentially allows for conformational changes within this portion of the inner membrane ring (58,59). At the C-terminal side (residues 142 – 371), the MxiG periplasmic domain is located within the *Shigella* periplasm (56). It is this domain that, with MxiJ, forms the stable inner membrane ring within the basal body. The two hydrophilic domains are connected with by an α-helical transmembrane domain (residues 127 – 141) that is just long enough to span on the bacterial inner membrane (56). Although structures for the MxiG transmembrane and periplasmic domains have not yet been determined, the structure of $MxiG^{Cyt}$ has been solved using NMR and the x-ray crystallography and these structures are available (see below) in the protein data bank (PDB).

The first $MxiG^{Cyt}$ structure was published at 2011 using NMR spectroscopy. This structure of $MxiG^{Cyt}$ (residues 6 – 112) was fit into electron densities from electron microscopy studies to determine its stoichiometry, which led to the first report that is has 24-fold symmetry within the inner membrane ring of the basal body (56). The NMR structure also revealed that $MxiG^{Cyt}$ is a

globular, β-sheet rich structure (one α-helix and nine β-sheets) that falls into the structural family of forkhead-associated (FHA) domains (PDB ID: 2XXS) (56). This FHA domain contains conserved structural motifs for this family of protein domains which were identified as recognizing phosphorylated threonine residues as part of its many molecular functions in prokaryotic and eukaryotic cells (60,61). In the $MxiG^{Cyt}$ structure, several of these structural motifs are apparent, however, *in vitro* and *in vivo* experiments suggests that the conserved residues involved in phosphothreonine binding for the canonical FHA domain are not essential for $MxiG^{Cyt}$ functions (56). In contrast, Barison et al. reported a high resolution x-ray crystal structure of $MxiG^{Cyt}$ (residue 1 – 126) that possesses one α-helix and 11 β-sheets (PDB ID: 4A4Y). Although the crystal structure is largely in agreement with the $MxiG^{Cyt}$ NMR structure, they suggested that $MxiG^{Cyt}$ has FHA domain functions, including the ability to interact with a phosphorylated Spa33 peptides based on surface plasmon resonance (SPR) data (62). To support these data, they reported a positive interaction between $MxiG^{Cyt}$ and Spa33 using pull down assays (62). In addition to these *in vitro* experiments, introducing substitutional mutations for residues they believed contained the conserved motifs of the FHA domain reduced *Shigella* T3SS activities such as secretion of Ipa proteins and invasion of mammalian cells (62). Currently, both investigations have conflicted arguments that the conserved structural motifs in $MxiG^{Cyt}$ have either the canonical or non-canonical FHA domain function that contributes to T3SS functions. To better understand $MxiG^{Cyt}$ and how it associates with proteins within the SP for T3SS activities, additional experiments are needed which will be described here.

Beneath the $MxiG^{Cyt}$ ring are the pod structures of the SP. Although the components of the SP are known, most of their structures and interactions are still unclear. The predominant protein of the pods is believed to be Spa33, which has protein homologues in the flagellar C-ring (45).

Interestingly, *spa33* encodes an internal translation initiation site where ribosomes can bind to produce a shorter fragment (residue 192 – 293) of the full length Spa33 protein (63). This genetic mechanism is shared within homologous proteins such as YscQ and SpaO that are from the *Yersinia pseudotuberculosis* T3SA and the *Salmonella typhimurium* T3SA, respectively (64,65). Therefore, *S. flexneri* is believed to express both the full-length and the C-terminal fragment of Spa33 (63). We have found that this short fragment of Spa33 associates with the full-length Spa33 to form a Spa33 complex. Based on MS analysis, the stoichiometry of this complex is a 1:2 ratio for the full-length Spa33 and two C-terminal fragments of the protein (63). This number is in agreement with YscQ and SpaO complexes with the SP of *Yersinia* and *Salmonella*, respectively (63-65).

The structure of full-length Spa33 and its complex have not been determined, however, a part (residue 208 – 293) of the Spa33 C-terminal fragment structure is available in PDB (PDB ID: 4TT9) (63). The length of this fragment is 86 residues which are equivalent to the C-terminal residues of the full-length protein (63). The overall structure of this domain is globular in shape, and it is similar to the surface presentation of antigen (SpoA) domain that is a highly conserved structure within FliN and the C-terminal portion of YscQ and HrcQ that are from the flagellar C-ring, the T3SA of *Yersinia pseudotuberculosis*, and the T3SA of the plant pathogen *Pseudomonas syringae*, respectively (63,64,66). Based on amino acid sequence alignment between the full length Spa33 and short fragment Spa33, the Spa33-containing pod may contain one full-length Spa33 whose SpoA domain interacts with a homodimer comprised of the short Spa33 C-terminal domain (SpoA domain) (63). Indeed, SpoA domains in FliN and FliM from the flagella C-ring, as well as SpaO from the *S. typhimurium* T3SA, are involved in interactions that allow oligomers formation and which are important for their functions (66,67). Importantly, current preliminary data suggest

that *S. flexneri* expressing the Spa33 C-terminal domain, but not the full length of Spa33, is not able to restore T3SS activities while a mutant that is lacking the short fragment of Spa33 complex in T3SA showed minimal such T3SS activities. Indeed, removal of the equivalent short domain of SsaQ, a homologues from the T3SS encoded by *Salmonella* Pathogenicity Island 2, showed low efficiency in effector secretion and invasion of mammalian cell levels (68). Moreover, the SsaQ C-terminal domain appears to stabilize the full-length of SsaQ, but it may not be involved as part of the T3SA assembly (68). The SsaQ data suggest that the C-terminal fragment from these homologous proteins may act as chaperone-like proteins for the full length protein to be imported into the fully functional T3SA (68).

For future investigation, the precise location of Spa33 and its binding partner(s) is needed to understand how the pod structures in the SP contribute to T3SS activities. Based on the previous cryo-ET images and a co-crystallization of SpaO and OrgB peptide (45,67), it is possible that MxiN is one of the Spa33 binding partners within the SP. In addition to MxiN, recent reports on the *S. typhimurium* T3SA suggest that in *Shigella* MxiK is also a part of the pod structure and it is a candidate protein for interacting with Spa33, however, clear evidence for MxiK's position and its binding partner(s) has not yet been reported.

1.6 *Salmonella* Type III secretion apparatus

Salmonella enterica is also a member of the Gram-negative *Enterobacteriaceae* and it causes gastroenteritis (salmonellosis). The CDC estimates that it causes almost 1.2 million of food borne illnesses and almost 450 deaths each year in the US (69). As with *S. flexneri*, *S. enterica* possesses T3SSs that are essential for its pathogenesis. Interestingly, this pathogen encodes several

pathogenicity islands on its chromosome, and two different types of T3SSs are encoded in *Salmonella* pathogenicity island (SPI)-1 and SPI-2, respectively (70). T3SS-1 from SPI-1 is needed for bacterial entry into eukaryotic cells and the activation of pro-inflammatory events. Meanwhile, T3SS-2 from SPI-2 is used for the modulating the host intracellular environment (70). T3SS-1 is functionally and structurally very similar to the *Shigella* T3SS. Effector proteins from T3SS-1, for instance, alter actin filaments to cause host membrane ruffing and destabilization of the tight junctions in the epithelial layer that are responsible for causing macrophage killing and for bacterial entry into epithelial cells (71,72).

Recently, the architecture of T3SS-1 has been studied using cryo-ET to provide the overall structure for the entire T3SA, including the SP. Hu et al. used cryo-ET techniques to show that the overall SP structure of T3SS-1 is very similar that of *Shigella* T3SS (59). The *Salmonella* T3SA also has pod-like structures that form a discontinuous six-fold symmetry and is connected with a central ATPase hexamer at the bottom via radial spoke-like structures (59). The pod-like structures interface with the cytoplasmic domain of inner membrane ring of the basal body. The dominant pod structure here is from SpaO (homologous to Spa33 in *S. flexneri*), which interacts with OrgB (homologous to MxiN in *S. flexneri*) and OrgA (homologous to MxiK in *S. flexneri*). OrgB is the spoke-like structure that connects InvC (homologous to Spa47 in *S. flexneri*) and SpaO in the pod structure (59,73). Moreover, recent mass spectrometry analyses was used to show that SpaO in each pod structure forms an oligomer that contains both full length and short fragments (C-terminal domains) of SpaO. As described above, the *spaO* gene also possesses an internal translation initiation site to produce two different sized SpaO proteins from the single gene (65,67,74). Interestingly, a *S. enterica* mutant expressing T3SS-1 without the short C-terminal fragment of SpaO shows only moderately reduced levels of T3SS activities, suggesting the C-terminal

fragment is probably only contributing to the stabilization of full length SpaO (65). The stoichiometry of the SpaO complex with OrgB and InvC is that two short fragments of SpaO bind to a single full-length SpaO to form an oligomer that allows formation of the SP pod (74). This heteromultimeric complex connects with a single InvC via an OrgB homodimer (74). Since InvC is a hexamer within the central hub of the SP, the six-fold symmetry of the pods allows each to connect via the OrgB spokes with the InvC ATPase. In addition to the MS analyses, Bernal et al. used the small-angle X-ray scattering (SAXS) to develop overall architecture model that is in agreement with previous cryo-ET images for the SP in the T3SA from *S. enterica* and *S. flexneri* (74). Currently, cryo-ET and SAXS have revealed an overall architecture for the SP, although high resolution structural information for most of the components is not yet available. What remains to be determined is the precise role of the Spa33/SpaO C-terminal domains in SP assembly and function. The studies cited above for Tejero et al. indicate that these C-terminal domains may only be needed as chaperones, however, conflicting data from McDowell et al. suggest they may be an actual structural components of the functional pods (63,65).

Generally speaking, architectures of T3SSs appear to be shared among homologous Gram-negative bacterial pathogens. In fact, cryo-ET images of T3SSs from *S. enterica* and *S. flexneri* have shown similar structures for each T3SA (45,59). Interestingly, *Salmonella* PrgH (homologous to MxiG in *S. flexneri*) in the inner membrane ring of T3SA-1 are present in 24 copies, but appear to bunch up to form six-fold symmetrical clusters with each cluster composed of four $PrgH^{Cyt}$ domains (59). This occurs where they interact with the MxiK homologue OrgA, however, no such clustering is observed in *Shigella*. Importantly, when the proteins make up the pod structure are removed from the *Salmonella* SP, PrgH forms 24-fold symmetry which is evenly spaced (59). This is the same symmetrical structure as formed by MxiG in the T3SA of wild-type *Shigella*

(45,56,57,62). This observation allowed Hu et al. to hypothesize that formation of the pod structures in the SP leads to conformational changes within the inner membrane ring for the translocation of needle and tip complex proteins during maturation of the T3SA (59).

Based on these data from *S. flexneri* and *S. enterica*, the pod-like structures contribute to assembly of the SP and this is required for a functional T3SS. In this process, all components involved in pod assembly are essential. Since pod-like structures had been observed from T3SA from *mxiN* null *S. flexneri* strain, the radial spoke-like structures within the SP form independent of formation of the six-fold symmetrical pods, but is still needed for localization of the ATPase within the SP (45). Because the T3SA from a *mxiK* null *S. flexneri* strain lack the entire SP and external needle, and this is the same phenotype seen for the T3SA from a *spa33* null *S. flexneri* strain (45), MxiK and its homologous proteins probably are a part of or are needed interacting partners with the Spa33 pods. We hypothesize that MxiK acts as adaptor between the inner membrane ring (MxiG) and the Spa33 pods in the functional SP. This association between the SP and basal body is somehow involved in conformational changes within the inner membrane ring that are the basis for T3SA function.

Chapter 2 Material and Methods

Materials:

Shigella flexneri 2a 2457T and *S. flexneri mxiK* null strains were from Dr. A. Allaoui (Université Libre de Bruxelles, Bruxelles, Belgium). *Shigella flexneri* 5 M90T and *S. flexneri mxiG* null SF703 strains were from Dr. John Rohde (Dalhousie University, Halifax, Nova Scotia, Canada). Sheep red blood cells were purchased from Colorado Serum Co. Denver, CO. For cloning, all oligonucleotide primers were purchased from Integrated DNA Technologies (Coralville, IA), and DNA sequencing was done by GenScript (Piscataway, NJ) and was used to confirm genes sequences. BACTH System Kit from Euromedex (Souffelweyersheim, France) was purchased for all BACTH experiments in this investigation. All cryo-ET experiments were performed in the laboratory of Dr. Jun Liu (Department of Microbial Pathogenesis, Yale University School of Medicine, New Haven, CT). Some of these cryo-ET methods are described here, however, all of these procedures were carried out in the Liu laboratory. 600 MHz NMR spectroscopy was carried out in the Biomolecular NMR Laboratory at University of Kansas. All materials and chemicals were purchased form MidSci, Inc. (Valley Park, MO) and Fisher Scientific (St. Louis, MO).

Buffers and reagents: See Appendix A

Sequences of primers used: See Appendix B

Growth conditions for *S. flexneri*

S. flexneri and its mutants were streaked onto trypticase soy agar (TSA) plates containing 0.025 % (w/v) Congo red (CR) with appropriate antibiotics and grown at 37 °C for overnight. *Shigella* with an active T3SS grow as red colonies on TSA plus CR. Red colonies from the plates were inoculated into trypticase soy broth (TSB) with the appropriate antibiotics, and then bacterial cultures were grown at 37 °C with shaking at 200 rpm.

Cloning for T4L insertion MxiK in pWPsf4

The gene for bacteriophage T4 lysozyme (T4L) was amplified using PCR with primers that encode a two amino acid linker. After the amplification, PCR products were purified using the agarose gel electrophoresis and QIAquick Gel extraction kit (QIAGEN). This purified PCR product was used for subsequent fusion or insertion of the gene into selected sites of *mxiK* from *Shigella*. For *mxiK* amplification, *mxiK* in the plasmid vector pWPsf4 was used as template, and primers were designed to allow T4L insertion using inverse PCR (75). The PCR products from the *mxiK* amplification were also purified using the QIAquick Gel extraction kit and QIAquick PCR purification kit (QIAGEN). The primers for the *mxiK* amplification contained 15 nucleotides homologous to the T4L gene and the linker. Thus, the PCR products are complementary at their respective 5' and 3' ends. 5× In-Fusion HD Enzyme Premix (Takara Bio) was used to ligate the sequences give the final gene for the T4L and *mxiK* fusion in pWPSf4 genes (at 50 °C for 15 min). This mixture was directly used for transformation into the *Escherichia coli* Novablue Singles cloning strain (Millipore Sigma). The cloned plasmids from these competent cells were then extract using QIAprep Spin Miniprep Kit (250) (QIAGEN) for DNA sequence confirmation.

Cloning wild-type *mxiK* and *mxiK-t4L* fusion genes into Bacterial Adenylate-Cyclase Two Hybrid (BACTH) plasmids and pT7HMT

Wild-type *mxiK* and *mxiK-T4L* fusion genes in pWPsf4 were used as template for PCR with primers encoding restriction sites. After purifying the PCR products, vectors for BACTH experiment (pKT25, pKNT25, pUT18, and pUT18C) and the purified PCR products were digested with BamHI and KpnI (New England BioLabs) and the products were purified by QIAquick PCR purification kit (250) (QIAGEN) (76). Clonables 2× Ligation Premix (Millipore Sigma) was used to ligate the PCR products into the plasmids at 15 °C for 15 min. These reaction mixtures were directly transformed into the *E. coli* Novablue Singles (Millopore Sigma) cloning strain with the plasmids then isolated for DNA sequence confirmation.

For cloning *mxiK* mutant genes into pT7HMT (77), the same procedures were used as for cloning into the BACTH plasmids, except for the restriction enzymes used. These PCR products and the empty pT7HMT were treated with BamHI and NotI (New England Biolabs).

Cloning of the MxiK point mutant

Primers containing desired point mutation were designed for the inverse PCR. These primers and wild-type *mxiK* in pWPsf4 (the template) were used to amplify a mutated version of *mxiK*. The PCR products were purified using the agarose gel electrophoresis and QIAquick Gel extraction (250) (QIAGEN). Dpn-1 (New England Biolabs) was used to digest the template, and then the QIAquick PCR purification kit (QIAGEN) was used for the purification of PCR products. Finally, purified PCR products were transformed into *E. coli* Novablue Singles (Millipore Sigma) for subsequent DNA sequencing.

Cloning for continuous Ala substitutional mutants for MxiK and MxiG in pWPsf4

Primers for nucleotides that encoded strings of Ala were designed to replace specific regions within MxiK or MxiG using inverse PCR. The wild-type genes (*mxiK* and *mxiG*) in pWPsf4 were used as templates for inverse PCR products containing homologous nucleotides at 5' and 3' ends. The agarose gel electrophoresis and QIAquick gel extraction kit (250) (QIAGEN) were used to purify the PCR products, which were then digested with Dpn-1 (New England Biolabs). The reaction mixtures were purified by QIAquick PCR purification kit (QIAGEN). The final product was treated with 5× In-Fusion HD Enzyme Premix (Takara Bio) to ligate the 5' and 3' ends. The reaction mixtures were transformed into the competent cells for DNA sequencing as already described.

Preparing *S. flexneri mxiK* null and *mxiG* null competent cells

Both *mxiK* null and *mxiG* null *S. flexneri* strains were grown in TSB with kanamycin (50 µg/mL) at 37 °C with 200 rpm shaking until OD_{600} reach between 0.4 and 0.7. When these cultures reached appropriate bacterial densities, they were harvested by centrifugation at 3756 ×g for 15 min at 4 °C. Bacterial pellets were washed with ice cold sterile diH_2O twice, and then washed with ice cold sterile 10 % (v/v) glycerol. At the end of washing, bacterial pellets were resuspended with the 10 % (v/v) glycerol and then stored in 100 µL aliquots. These competent cells were stored at -80 °C.

Electroporation of *S. flexneri* complement strains

Two µL pWPsf4 was added to 50 µL of *S. flexneri* null strains were put into 1.7 mL sterile Eppendorf tubes. The mixture was transferred into an electroporation cuvette (Fisher Scientific),

and a MicroPulser apparatus (Bio-red Laboratories) was used for the transformation. One mL of Lysogeny Broth (LB) medium was added to the cuvette and then the transformed bacterial culture were transferred into new 1.7 mL Eppendorf tube and incubated at 37 °C with 200 rpm shaking for an hour. The bacterial were then spread on TSA plates with kanamycin (50 µg/mL) and ampicillin (100 µg/mL) to obtain isolated single colonies.

Preparing *S. flexneri* mutants with pBS58 for cryo-ET

Mini-cell strains of *S. flexneri* were prepared by transforming them with the plasmid pBS58 (45). pBS58 is a low copy number plasmid that continuously expresses the *E. coli* cell division genes *ftsQ*, *ftsA* and *ftsZ* which cause aberrant cell division (44). Transformants were grown on TSA plates with kanamycin (50 µg/mL) to select for Tn deletions in SP protein null strains and spectinomycin (100 µg/mL) to select for pBS58. A single colony from these plates was inoculated into TSB with both antibiotics to prepare competent cells for electroporation which is described above. After preparing these competent cells of the *Shigella* null strains, *mxiK* or *mxiG* mutant genes in pWPsf4 were used to transform these competent cells using the electroporation. These transformants were grown on TSA plates with kanamycin (50 µg/mL), ampicillin (100 µg/mL) and spectinomycin (100 µg/mL). Isolated single colonies from these plates were inoculated into TSB with these three antibiotics to prepare glycerol stock. To enrich for mini-cells, the culture was centrifuged at 1000 ×g for 5 min to remove the large cells, and the supernatant fraction was further centrifuged at 20,000 ×g for 10 min to collect the mini-cells for cryo-ET analysis. All of the cryo-ET work was done in the laboratory of our collaborator Dr. Jun Liu (45,57).

Measuring overnight steady state secretion

Isolated colonies of different *Shigella* strains from Congo-red plates were grown in TSB with the appropriate antibiotics at 37 °C with 200 rpm shaking for overnight. The overnight cultures were centrifuged with 3756 ×g for 15 min at 4 °C to obtain supernatants. One mL of 100 % (w/v) trichloroacetic acid (TCA) was added into nine mL of each supernatant sample (78), and then they were incubated on ice for 30 min. Precipitated proteins in the supernatants were harvested using centrifugation at 11,963 ×g for 15 min at 4 °C. The pellets were washed with 10 mL of 5 % (w/v) TCA, and then centrifuged at 11,963 ×g for 15 min at 4 °C. These pellets were washed with 2 mL of ice cold acetone twice and then pellets were dissolved in with 400 µL of phosphate-buffered saline (PBS). To prepare samples for SDS-PAGE and immunoblot analysis, 200 µL of 3× SDS-PAGE sample buffer was added and 10 µL of each sample was loaded into 10 % SDS-PAGE gels. To compare the levels of secreted Ipa proteins, an immunoblot assay was performed using primary antibodies against IpaB (see below). Samples were also loaded onto another 10 % SDS-PAGE gel which was stained with Coomassie blue to visualize all protein bands. A band at 100 kDa was a protein called SepA that is secreted independent of the T3SS and this was used as a loading control.

Immunoblot assay for Ipa proteins

For immunoblot analysis, the proteins from an unstained SDS-PAGE (10 % gel) were transferred to a nitrocellulose membrane with 1.3 A at 25 V for 7 min using Trans-Blot Turbo (Bio-Rad Laboratories). Then the membrane was incubated with a blocking buffer (Li-COR) for an hour at room temperature. After discarding the blocking buffer, the primary antibody mixture which contains antibodies against recognize IpaB, IpaC, and IpaD was added and the membrane was incubate an hour at room temperature. Tris-buffered saline (TBS) containing Tween 20 was

used to wash the membrane three times for 5 min each. The membrane was then incubated with secondary antibodies labeled with an IR dye (Li-COR) at room temperature for an hour. The membrane was again washed three times with TBS containing Tween 20. An ODYSSEY CLx imager (Li-COR) was used to detect and measure strength of IR signals from the secondary antibodies. Only the signal from IpaB was used for quantitative purposes.

Contact-mediated hemolysis assay

Contact-mediated hemolysis tests for *Shigella*'s ability to form functional translocon pores in host cell membranes. Isolated *Shigella* colonies were inoculated into TSB with the appropriate antibiotics and the bacteria grown at 37 °C with 200 rpm shaking until mid-log phase (A_{600} of about 0.5). Ten mL of the bacterial cultures were then centrifuged at 3756 ×g for 15 min at 30 °C to pellet the bacteria. The pellets were resuspended with PBS with the volume normalized based on the bacterial densities at A_{600} with approximately $1/50^{th}$ of the culture volume. In parallel, 3 mL of the sheep red blood cells (RBC) (Colorado Serum, Co.) were washed twice with 40 mL PBS. The RBC pellets were then resuspended with 3 mL of PBS to be 4.0×10^9 cells/mL (19). Then, 50 µL each of the bacterial samples and RBC were placed in a round bottom 96 well plate (Fisher Scientific) and the plate was centrifuged with 2,876 ×g for 15 min at 30 °C. After that, the plate was incubated at 37 °C for 15 min. Then, 100 µL of ice cold PBS was used to resuspend the mixture of bacteria and RBC in the wells, and then the plate was centrifuges with 2876 ×g for 15 min at 10 °C. The supernatants were transferred into a new round bottom 96 well plate to measure the released hemoglobin as the absorbance at 545 nm (A_{545}) using a SpectraMax i3 spectrophotometer (Molecular Devices, Inc.) (19). These absorbance was used to calculate the

relative levels of hemolysis. Osmotic shock using water was used as a positive control and PBS was used as a negative control.

Testing for expression of MxiK-T4L fusion protein in *S. flexneri*

To make sure the cells transformed with plasmids for expressing T4L fusion proteins were actually producing this recombinant protein, we again performed immunoblot analysis. The *Shigella* strains (*mxiK* null, wild-type *mxiK* complement and T4L insertion mutants) were grown in TSB with appropriate antibiotics at 37 °C for overnight. One mL of overnight culture was centrifuged with 5,000 ×g for 10 min to collect bacterial pellets, which were washed with PBS. Washed bacterial pellets were prepared for SDS-PAGE and immunoblot assay using 15 % SDS-PAGE gels. The amount of sample loaded on the gels was based on the absorbance at 600 nm (A_{600}) of the culture.

Immunoblot assay for T4L

All procedures are same as the immunoblot assay of Ipa proteins except for the incubation of the primary antibodies. To detect T4L on blotted membranes, guinea pig anti T4L was used as the primary antibody. A blotted nitrocellulose membrane with the primary antibody was incubated at 4 °C for overnight. Donkey anti guinea pig with IR label (Li-COR) was used for secondary antibody, and the ODYSSEY CLx imager (Li-COR) was used to detect signals from the secondary antibody.

Preparing *E. coli BTH101* competent cells for BACTH analysis

E. coli BTH101 was inoculated and grown in LB with streptomycin (100 µg/mL) until mid-log phase. The bacterial pellet was obtained by centrifugation at 3756 ×g for 15 min at 4 °C. The bacteria were then resuspended in 50 mM of $CaCl_2$. The resuspended bacteria were incubated on ice for 20 min and then collected by centrifugation. The bacterial pellet was resuspended with 50 mM $CaCl_2$ with 15 % (v/v) glycerol and incubated on ice for 20 min. The competent cells were stored at -80 °C (76).

Bacterial Adenylate Cyclase Two-Hybrid (BACTH) analysis

Ten ng/µL of plasmids harboring the genes of interest fused with genes for the T25 and T18 domains of *Bordetella pertussis cyaA* and used to transform 50 µL of *E. coli BTH101* using the heat shock method – 42 °C for one minute. The transformed cells were spread on LB plates with kanamycin (50 µg/mL) and ampicillin (100 µg/mL), and incubated at 30 °C for overnight. The next day, at least three isolated colonies from the plates were separately inoculated into LB medium with 0.5 mM of IPTG, kanamycin (50 µg/mL), and ampicillin (100 µg/mL) for overnight growth at 30 °C with 200 rpm shaking. The overnight culture was washed with M63 medium three times and the bacteria were harvested and their pellets were resuspended with M63 medium. Two µL of resuspended bacteria were spotted onto MacConkey agar plates containing maltose and M63 agar plates containing X-gal. These plates were incubated at 30 °C to monitor for color changes that would indicate the presence of active adenylate cyclase, which can only occur if the two proteins fused to T25 and T18 are interacting.

MxiK-T4L fusion protein induction

E. coli Tuner (DE3) (Millipore Sigma) possessing the plasmid pT7HMT containing the desired MxiK-T4L insertion mutant gene was inoculated into LB medium with kanamycin (50 µg/mL) and grown at 37 °C with 200 rpm shaking overnight. The overnight culture was inoculated into one L of LB medium with kanamycin (50 µg/mL), and the bacteria grown at 37 °C with 200 rpm shaking until the A_{600} reached about 0.3. When the bacterial culture reached the desired density, the temperature and shaking speed were reduced to 16 °C and 100 rpm, respectively, to cool down the bacterial culture. After an hour (A_{600} of about 0.6), expression of the MxiK-T4L fusion proteins was induced with 0.25 mM IPTG. This bacterial culture was incubated at 16 °C for overnight production of protein.

Extraction of MxiK-T4L fusion protein using Detergent

The overnight bacterial culture was harvested by centrifugation at 3,470 ×g for 15 min at 4 °C. The bacterial pellet was resuspended with the IMAC binding buffer containing the protease inhibitor AEBSF (Sigma Chemical Co.) The cells were then lysed by ultra-sonication. To obtain the inclusion bodies, the bacterial lysate was centrifuged with 22,217 ×g for 30 min at 4 °C. The pellets were washed with the binding buffer twice and then resuspended with the binding buffer containing 0.1 % (v/v) N,N-Dimethyldodecylamine N-oxide (LDAO) with AEBSF. The bacterial suspension was incubated at 4 °C overnight. The next day, the suspension was centrifuged 22,217 ×g for 30 min to obtain the supernatant to be used for the protein purification.

Purification of the MxiK-T4L fusion protein

After the extraction of MxiK proteins into soluble fraction, nickel IMAC was used to purify the MxiK fusion proteins via an N-terminal His-tag. To remove nonspecific proteins from the Ni^{++}

resin, 20 column volumes of the IMAC binding buffer and another 20 column volumes of the binding buffer containing 5 % (v/v) elution buffer were used to wash the column. To elute the fusion protein from the resin, 10 column volumes of the elution buffer was used. Immediately after this step, this elution fraction was applied to HiLoad 16/600 Superdex 75 pg (GE Healthcare Life Sciences) for size exclusion chromatography (SEC).

Expression of recombinant Spa33

E. coli Tuner (DE3) strains harboring *spa33* in pT7HMT were inoculated into LB medium containing kanamycin (50 µg/mL) and grown at 37 °C with 200 rpm shaking overnight. The overnight culture was inoculated into one L of LB medium with kanamycin (50 µg/mL) and grown to an A_{600} of about 0.3. Then, the culture was grown at 16 °C for an hour. Spa33 was induced with 0.5 mM IPTG, and the bacterial culture was incubated at 16 °C with 200 rpm shaking overnight. The next day, the bacterial culture was harvested by centrifugation 3470 ×g for 15 min at 4 °C.

Spa33 purification

The bacterial pellets were resuspended with IMAC binding buffer and a microfluidizer was used to lyse the cells (18,000 psi with three cycles). The soluble fraction was obtained by centrifugation 22,217 ×g for 30 min at 4 °C and this was used for purification of Spa33. A His-trap Ni^{++} IMAC column (GE Healthcare Life Sciences) was used for the first purification step with the recombinant protein eluted with IMAC elution buffer after washing the column. To cleave off the His-tag, TEV protease, 1.0 mM EDTA, and 1.0 mM DTT were added into the solution. The sample was then dialyzed into IMAC binding buffer. Then, as a second purification step, His-trap Ni^{++} IMAC column (GE Healthcare Life Sciences) was used to prepare the recombinant protein

without the His-tag. The recombinant protein without the tag was collected in the flow through. After buffer exchange by dialysis, the protein was put into Q binding buffer for subsequent ion exchange chromatography.

A Q column (GE Healthcare Life Sciences) was as a third purification step. Spa33 was eluted from the column using a gradient of Q elution buffer containing high salt. This was performed on an AKTA (GE Healthcare Life Sciences) liquid chromatography system. The recombinant protein was collected for the final purification step. A Hi Load 26/600 Superdex 200 pg (GE Healthcare Life Sciences) SEC column was used for the final purification step. For this step, Spa33 was concentrated to a two mL final volume for injection onto the SEC column. The recombinant protein was eluted with the SEC buffer.

Purification of MxiN

MxiN production was induced by same procedures as Spa33. *E. coli* Tuner (DE3) cells (Sigma Millipore) with *mxiN* in pT7HMT were harvested and resuspended in IMAC binding buffer. The cells were lysed using a microfluidizer (18,000 psi with three cycles). The soluble fraction was collected by centrifugation (22,217 ×g for 30 min at 4 °C). MxiN in the soluble fraction was purified by His trap Ni^{++} IMAC column (GE Healthcare Life Sciences), and then TEV protease was added to cleave off the His-tag for the reverse Ni^{++} IMAC purification. If His-tag was needed for a given experiment (for example, Biolayer interferometry or BLI), the elution fractions from the first Ni^{++} IMAC were saved. With or without the His-tag, the final purification step was SEC using Hi Load 26/600 Superdex 200 pg (GE Healthcare Life Sciences).

Testing the MxiN-Spa33 interaction using SEC

Purified MxiN and Spa33 were dialyzed into the buffer used for SEC. Then, MxiN and Spa33 were combined and concentrated to two mL final volume for injection onto a Hi Load 26/600 Superdex 200 pg column (GE Healthcare Life Sciences). The protein absorbance at 280 nm was monitored to detect protein elution on an AKTA system (GE Healthcare Life Sciences). The eluted fractions were collected for SDS-PAGE analysis.

Testing the MxiN-Spa33 interaction using Biolayer interferometry (BLI)

Purified His-tagged MxiN was dialyzed into BLI buffer for binding to the pins of an Octet^{RED} 96 BLI system (FortéBIO, Inc.). Spa33 without a His-tag was prepared and the protein concentration was adjusted 400, 200, 100, 50, 25, and 12.5 µg/mL. The Octet^{RED} 96 (FortéBIO, Inc.) was then used to measure the dissociation constant for the MxiN and Spa33 interaction. For these measurements, 10 µg/mL of MxiN was loaded onto a Ni-NTA biosensor tip (FortéBIO, Inc.), which was then washed with BLI buffer. The binding of Spa33 at each concentration given above to the immobilized MxiN was measured to obtain the association rate. The biosensor tips were then placed into BLI buffer lacking Spa33 to measure the dissociation rate. These parameters were used to calculate dissociation constant (Kd) using the program associated with the BLI instrument.

Circular Dichroism (CD) spectroscopy of the MxiK-T4L fusion proteins and MxiN

The MxiK fusion proteins in SEC buffer were dialyzed into PBS containing 0.1 % (v/v) LDAO. Protein concentrations were adjusted to around 350 µg/mL and the sample filtered through a 0.22 µm membrane for CD spectroscopy. Then, 250 µL of the protein samples were put into quartz cuvettes with a 0.1 cm path length. The spectra were measured in triplicate. Buffer alone was used as the blank. The CD spectrum was measured between 190 and 260 nm light using on a

J-15000 model spectropolarimeter (JASCO). The CD spectral signals were converted to molar ellipticity. The thermal stability of the proteins were measured at 222 nm over a temperature range from 10 to 90 °C. Data were collected every 2.5 °C and the temperature was increased 15 °C/hr. In parallel, 380 µg/mL of T4L in PBS with 0.1 % (v/v) LDAO was used to measure the T4L CD spectrum in the absence of any MxiK component. To obtain the CD spectrum of MxiN samples, its concentration was adjusted around 200 µg/mL in the SEC buffer. Molar ellipticity was obtained as above in the 190 to 260 nm range and the MxiN thermal stability was measured at 222 nm over a temperature range 15 to 90 °C. Data were collected every 2.5 °C, and the temperature was increased 15 °C/hr.

^{1}H-^{15}N HSQC NMR spectroscopy for MxiN

E. coli Tuner (DE3) possessing the *mxiN* gene in pT7HMT was inoculated into LB with kanamycin (50 µg/mL) and grown at 37 °C overnight. The overnight culture was inoculated into one L of LB with kanamycin (50 µg/mL) and grown until the A_{600} reached 0.6. Three L of the bacterial culture was centrifuged and the bacterial pellets washed with M9 minimal medium. These washed cells were inoculated into one L of M9 minimal medium containing ^{15}N labeled ammonium chloride and grown at 37 °C for an hour. MxiN was induced with 0.4 mM IPTG and the bacterial cultures incubated at 16 °C overnight. Next day, the bacterial culture was harvested and the standard purification procedure for MxiN was used to purify the recombinant protein. After purifying ^{15}N-labeled MxiN, it was dialyzed into NMR buffer. The finial concentration of MxiN was almost 180 µM. For ^{1}H-^{15}N HSQC NMR measurements, D_2O was added to the MxiN sample. The sample was placed in an NMR tube and the HSQC spectrum was collected at 25 °C using 600 MHz NMR (Bruker, Co.).

Chapter 3 MxiK and MxiG Generate the Symmetrical Transition in the *Shigella* T3SS

3.1 Introduction

Shigella flexneri is Gram-negative member of the *Enterobacteriaceae* and causes bacillary dysentery (shigellosis) characterized by bloody diarrhea containing mucus, severe stomach cramps and fever. Children, especially younger than five years old, are at high risk from this disease (9). *Shigella*'s primary virulence factor is a type III secretion system (T3SS) which is used to directly translocate virulence effector proteins into eukaryotic host cells. The type III secretion apparatus (T3SA) is a protein nanomachine that is composed of four main parts as described in Chapter 1. Recent studies using cryo-electron tomography (cryo-ET) on mini-cells have provided the first visualization of the *in situ* T3SA with its intact cytoplasmic sorting platform (SP). The SP can be described as having two parts: a central hub and six surrounding pod-like structures (45). Hu et al. was able to fit published high-resolution protein structures of some SP components (or their homologues from the flagella T3SS) into their cryo-ET density maps to localize some of the proteins within the SP (45). The central hub is comprised of a Spa47 hexamer. Spa47 is an ATPase that provides energy for T3SS functions. Spa47 is connected with the surrounding pod structures the via the radial spoke protein MxiN near the bottom of the SP (45). Currently, Spa33 is believed to be the major component of the pod structures, based mostly on its homology with FliN and FliM from the flagella T3SA, which are proteins that make up the flagella C-ring (45). Since Spa33 and its homologous protein structures have not been determined, yet, the precise makeup of the pods remains to be determined (see Fig. 1.3 in Chapter 1). Based on a proposed unifying nomenclature

(Table 3.1) (79-83), Spa47 falls into the T3SS ATPase family SctN and Spa33 falls into the SP family SctQ.

In previous studies, MxiK of *Shigella* (SctK using the unifying nomenclature) co-immunoprecipitates with other SP components (84). Moreover, *Salmonella* OrgA (SctK family) has been localized to its pod structures (59). These data suggest that MxiK is a candidate for being located within an as yet unknown region of the *Shigella* SP pods. In fact, the T3SA from a *mxiK* null *S. flexneri* strain fails to assemble any part of the SP and lacks the external needle due to an inability to secrete any proteins (Fig. 3.1) (57). This is the same phenotype as seen for the *Shigella* T3SA for a *spa33* null *S. flexneri* mutant (45). Despite the fact that MxiK is an essential SP component, its position within the SP was unknown prior to the work being reported here. In this Chapter, I will determine the MxiK position within the SP using a combination of mutagenesis and supporting cryo-ET techniques carried out in the laboratory of Jun Liu (Yale University). The position of MxiK suggests that it contributes to the symmetry transition between the inner membrane ring (24-fold symmetry) and the pods (six-fold symmetry).

Currently, protein structures of SctK family proteins have not been determined, and this fact makes it more difficult to localize the MxiK position using cryo-electron tomographic techniques. To overcome this problem, a tag was fused with MxiK so that the additional electron density from the tag within the SP could be observed using cryo-ET. This additional electron density helped us to localize MxiK position in the SP. Bacteriophage T4 lysozyme (T4L) was chosen as the tag to be inserted into MxiK after expression from the plasmid, pWPsf4, which is able to express the recombinant *mxiK* in *S. flexneri* (75). Based on a high resolution structure of T4L (PDB ID: 2LZM), the distance between N- and C- termini is almost 9.1 Å which allows us to presume that the MxiK structure is least likely to be disrupted by the T4L insertion if that insertion

Location	Sct name	*S. flexneri*	*S. typhimurium* T3SS-1	*P. aeruginosa*	Flagella apparatus
Needle	SctF	MxiH	PrgI	PscF	-
IM ring	SctD	MxiG	PrgH	PscD	-
IM ring	SctJ	MxiJ	PrgK	PscJ	-
IM	SctV	MxiA	InvA	PcrD	FlhA
SP	SctK	MxiK	OrgA	PscK	-
SP	SctQ	Spa33	SpaO	PscQ	FliM + FliN
SP	SctL	MxiN	OrgB	PscL	FliH
SP	SctO	Spa13	InvI	PscO	FliJ

Table 3.1. Name of secretion and cellular translocation (Sct) for T3SS and flagella apparatus. Sct name which is the unified nomenclature for homologous proteins among T3SS including flagella apparatus are listed in this table with protein positions (79-83).

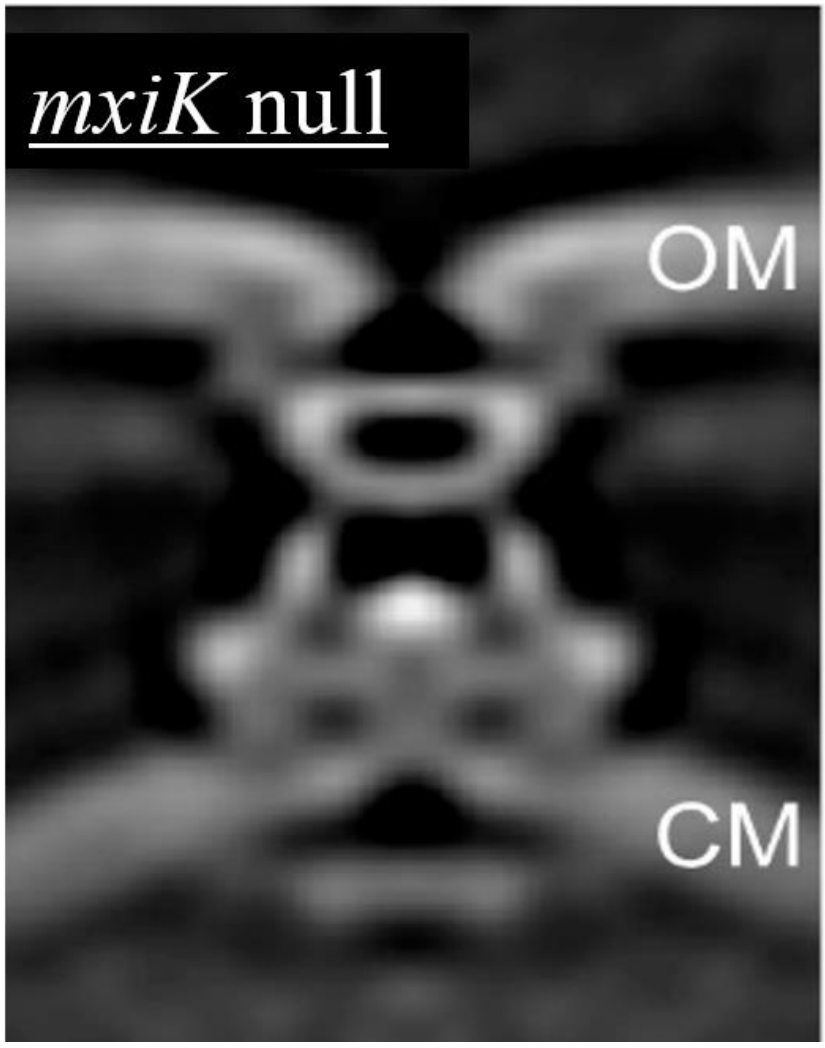

Figure 3.1. Cryo-ET image of T3SA from *mxiK* null *S. flexneri*.

T3SA from the *mxiK* null strain was observed using cryo-ET. The basal body spans within the outer membrane (OM) and cytoplasmic membrane (CM). Although the basal body is assembled appropriately, the entire SP and needle were not observed from this T3SA. This T3SA is almost identical with T3SA from *spa33* null *S. flexneri* strain. Also, as with the *spa33* null strains, the central channel of the basal body is closed at multiple points.

is within an exposed loop (Fig. 3.2). In fact, in previous experiments with IpaB T4L insertion mutants expressed in *S. flexneri*, most of the insertion mutants maintained IpaB functions (85). For insertion sites in MxiK, its secondary structure was predicted using PSIPRED program. Based on that analysis, MxiK was predicted that it has least five large loops in its structure. Therefore, T4L gene was inserted at the N- and C-termini, as well as in these loop regions of *mxiK* in pWPsf4 (Fig. 3.3). To develop a MxiK-T4L insertion *S. flexneri* mutant library, the *mxiK* null *S. flexneri* strain was complemented with these plasmids using electroporation. For cryo-ET, MxiK-T4L insertion mutants that possess a functional T3SS is required to observe changes in the pod structure in the SP because the T3SA from *mxiK* null *S. flexneri* mutant lacks the entire SP. We presume that T4L mutants that are inactive would also lack the SP.

To test T3SS activities for MxiK-T4L insertion *Shigella* mutants, overnight steady secretion and contact-mediated hemolysis assays were performed. To test secretion function, bacterial cultures were incubated at 37 °C for overnight, and proteins secreted into the culture supernatant were identified. Since Ipa proteins (IpaB, IpaC, and IpaD) are secreted via the functional T3SS into bacterial cultures, these proteins were used to analyze the secretion function of the T3SS. Trichloroacetic acid (TCA) was used to precipitate Ipa proteins in the culture supernatant followed by centrifugation. Then these proteins were detected by immunoblot analysis as described in Chapter 2. In addition to testing secretion, a contact-mediated hemolysis assay was performed to test for translocon pore formation (75). Since IpaB and IpaC form translocon pores in eukaryotic cell membranes, hemoglobin released from red blood cells after forced contact with *S. flexneri* is measured based in the absorbance of the hemoglobin (19,75). Since the MxiK-T4L insertion mutants with a functional T3SS are expected to have an intact SP with the additional T4L density, a mutant which is positive for both the secretion of Ipa proteins and hemolytic activity

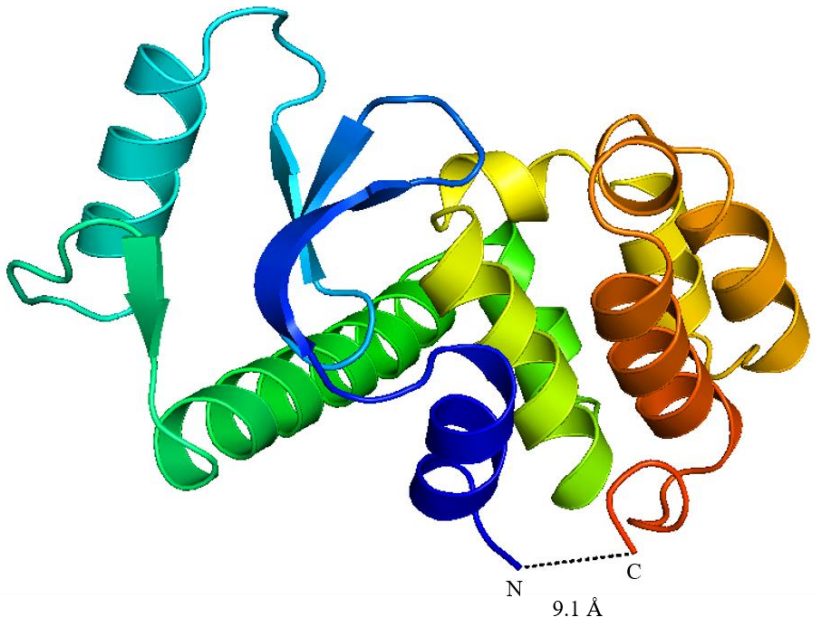

Figure 3.2. The high resolution structure of the bacteriophage T4 lysozyme (T4L).

The crystal structure of T4L from PDB is shown here (PDB ID: 2LZM). T4L is an α-helix rich protein. Residues 1 to 162 T4L was inserted into MxiK, and the distance between N-terminal (N) and C-terminal ends (C) is 9.1 Å.

Figure 3.3. Predicted secondary structure of MxiK using PSIPRED.

PSIPRED was used to predict the MxiK secondary structure. All secondary structures in MxiK are α-helices which is shown as cyan colored regions. The T4L insertion sites for this investigation are indicated by the black arrows. Eight MxiK-T4L insertion mutants were constructed.

was selected for cryo-ET. Once we visualize the additional electron density from the T4L within the SP, we will know the MxiK position.

Our laboratory has collaborated with Dr. Jun Liu's group at Yale University for cryo-ET and image analysis of the resulting images. Therefore, we sent all mutants of interest to his laboratory after transforming them with plasmids to give rise to mini-cell for obtaining cryo-ET data and images on the *in situ Shigella* T3SA. To determine the position of MxiK in the SP, cryo-ET images of the pod structure from both wild-type *S. flexneri* and a MxiK-T4L insertion mutant with a fully functional T3SS, we compared their density maps so that any additional electron densities from the T4L could be observed and localized. This T4L position helped us to determine MxiK position in the SP. Because of using a mutant with a functional T3SS, we presumed that the T4L in the pod structure does not have a negative effect for T3SA assembly and function.

In parallel, a bacterial adenylate cyclase two-hybrid (BACTH) series of experiments were performed to support MxiK's position within the SP and to confirm its binding partners. Since the as yet unidentified region within the pod structure facing the inner membrane ring creates a link with the bottom (major) density of the pod, interaction among three proteins, MxiK, Spa33, and the cytoplasmic domain of MxiG ($MxiG^{Cyt}$) were examined as part of this investigation. To prepare for this experiment, the genes for the two proteins of interest gene are cloned into plasmids as fusions with genes that encode subdomains of the catalytic portion of adenylate cyclase toxin (*cyaA*) from *Bordetella pertussis* (the T18 and T25 subdomains) (76). If T18 and T25 are brought together in the proper orientation by the association of their fusion partners, CyaA activity is restored (76). These plasmids were transformed into the *BTH101* strain of *E. coli*, which lacks endogenous adenylate cyclase activity (cya^-). Therefore, when two proteins show an interaction in this *E. coli* expression strain, both associated subdomains allow for the production of cAMP from

ATP (Fig. 3.4) (76) . Since cAMP enhances the expression of *lac* and *mal* operons, positive interactions from two test proteins are detected by color changes in the bacterial colonies on X-gal-containing agar plates and MacConkey agar plates with lactose or maltose as the carbon source. As mentioned in Chapter 1, Spa33 is believed to form a hetero-oligomer within the main pod structure. Accordingly, another member of our laboratory successfully introduced a mutation in wild-type *spa33* to express only the Spa33 C-terminal complex ($Spa33^{Cterm}$) or full-length Spa33 without the C-terminal domain being expressed ($Spa33^{FL}$). In addition to testing the interaction between MxiK and wild-type Spa33 ($Spa33^{WT}$), we cloned both of these Spa33 variants into plasmids for this experiment to determine how MxiK interacts with all components of the Spa33 complex.

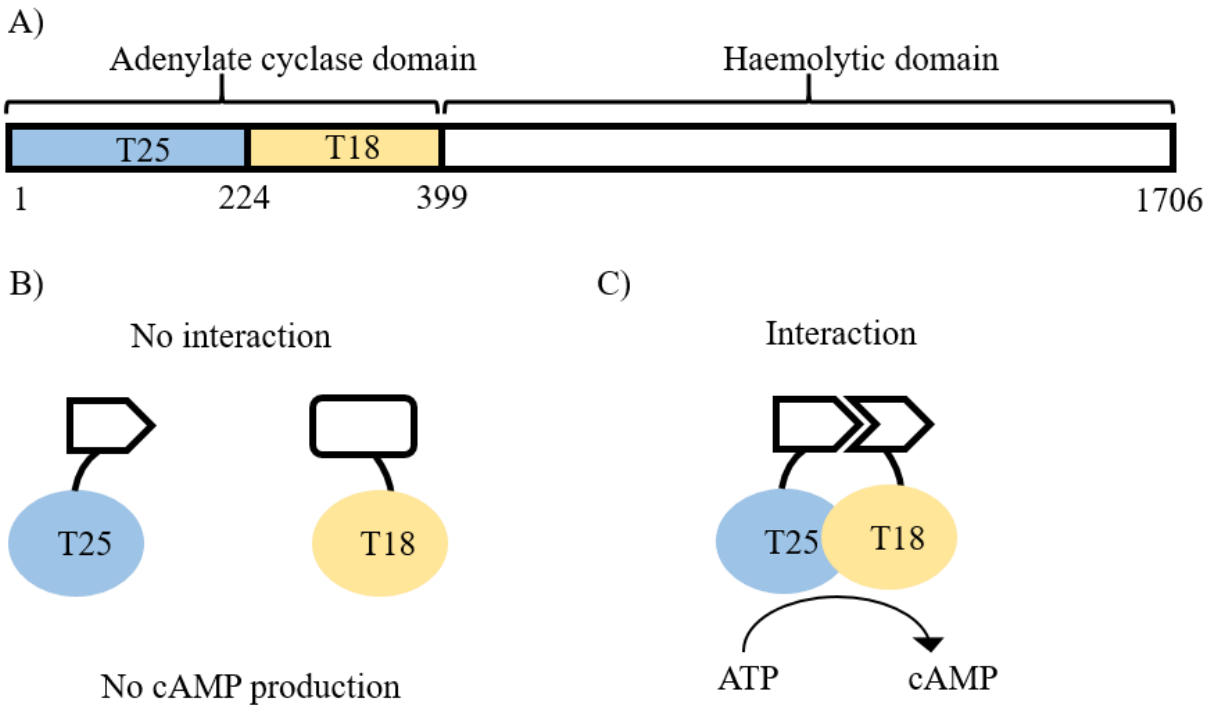

Figure 3.4. Diagram for the mechanism of the BACTH system.

The rationale of the BACTH system is shown in these diagrams. A) The adenylate cyclase from *Bordetella pertussis* CyaA is composed of two domains, the adenylate cyclase domain and hemolytic domain. The adenylate cyclase domain has two subdomain, T25 and T18, which are 25 kDa and 18 kDa proteins, respectively (76). B) When two fused proteins do not show an interaction, the T25 and T18 subdomains remain separated, which results in the no cAMP production in *E. coli BTH101* (76). C) When two fused proteins show an interaction, T25 and T18 subdomains are close together. This association of the two subdomains (if properly oriented) results in restoration of the enzymatic activity and then cAMP is produced from ATP in the *E. coli*$^{Cya-}$ strain (76).

3.2 Results

Overnight steady state secretion for MxiK-T4L insertion mutant.

MxiK-T4L insertion mutant genes were cloned into pWPsf4 plasmids and successfully transformed into the *mxiK* null *S. flexneri* strain using electroporation. To test secretion activity, the overnight steady secretion of Ipa proteins was examined. Although T4L insertion at 25, 55, and 136 mutants showed greatly reduced or disrupted secretion abilities, the other insertion mutants had restored secretion activities. Surprisingly, T4L at 101, 145, N-, and C-termini showed almost the same secretion levels as wild-type *S. flexneri* (Fig. 3.5).

Contact-mediated hemolysis assay for the MxiK-T4L insertion mutants.

To test the successful generation of translocon pores (a result of a fully functional T3SS), a contact-mediated hemolysis assay was performed for all the MxiK-T4L insertion mutants. This was done in parallel with the secretion assay above and, as with that assay, almost all of the mutants restored hemolytic activities. Importantly, the T4L insertion at 101, 145, N-, and C-termini showed almost the same activity levels as the wild-type *S. flexneri*. Meanwhile, insertion at 25 and 136 greatly reduced or disrupted hemolytic activities (Fig. 3.6). Moreover, the relative hemolytic activities correlate well with IpaB secretion for these mutants (Fig. 3.5).

Determination of the T4L and MxiK positions within the SP.

Based on the results of the overnight steady secretion assay (Fig. 3.5) and contact-mediated hemolysis assay (Fig. 3.6), T4L insertion at C-terminal end of MxiK (MxiK-T4L-C) restored both secretion and hemolytic activity to almost the same levels as *Shigella* expressing wild-type *mxiK*.

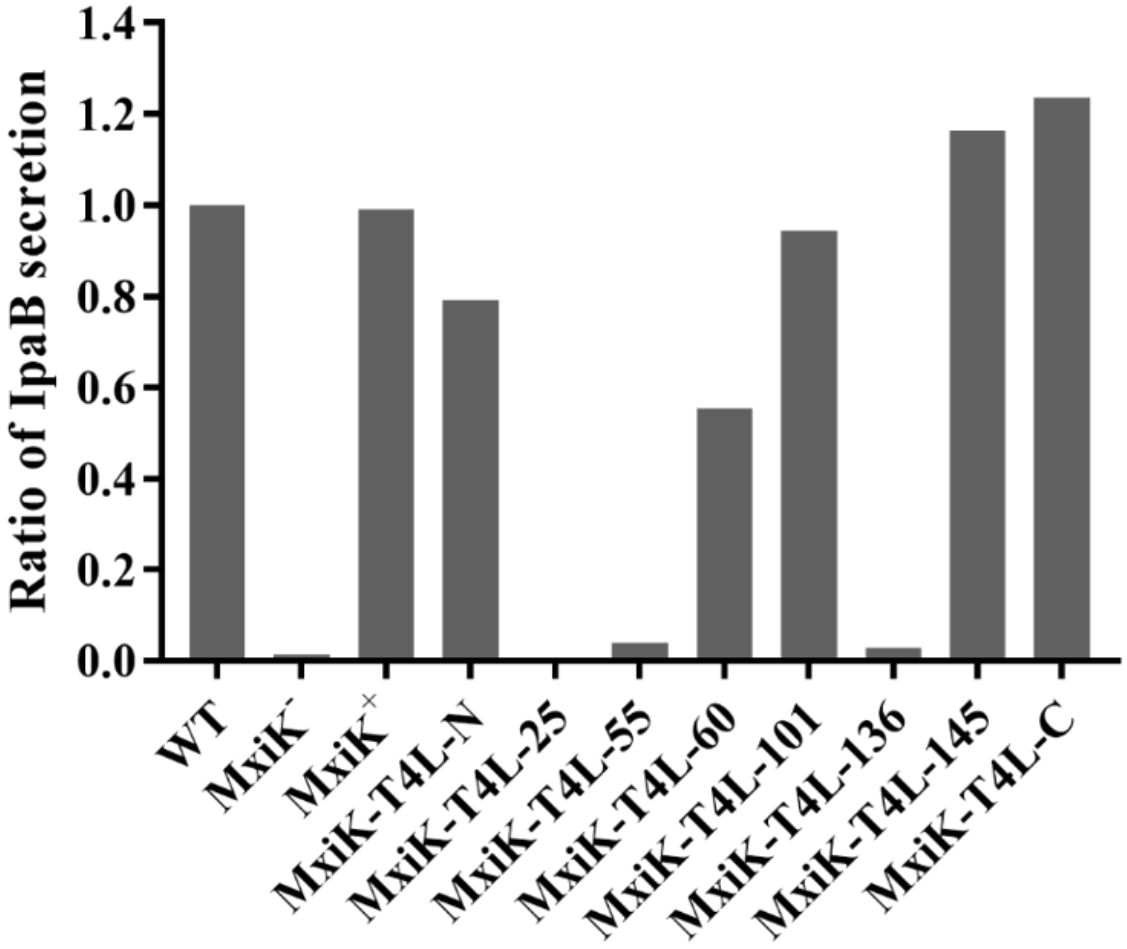

Figure 3.5. Overnight steady secretion assay for MxiK-T4L insertion *Shigella* mutants.

Overnight steady state secretion for each mutant was examined by monitoring the secretion of IpaB in *Shigella* overnight cultures. Proteins in the soluble supernatant of overnight bacterial cultures were precipitated and separated by SDS-PAGE for immunoblot analysis. Rabbit anti-IpaB serum was used for the primary antibody, and donkey anti-rabbit serum with an infrared fluorescent dye was used for the secondary antibody. After detecting the signal of IpaB from all samples, a signal from wild-type *S. flexneri* (WT) was used to quantify the relative signals for IpaB from all mutants.

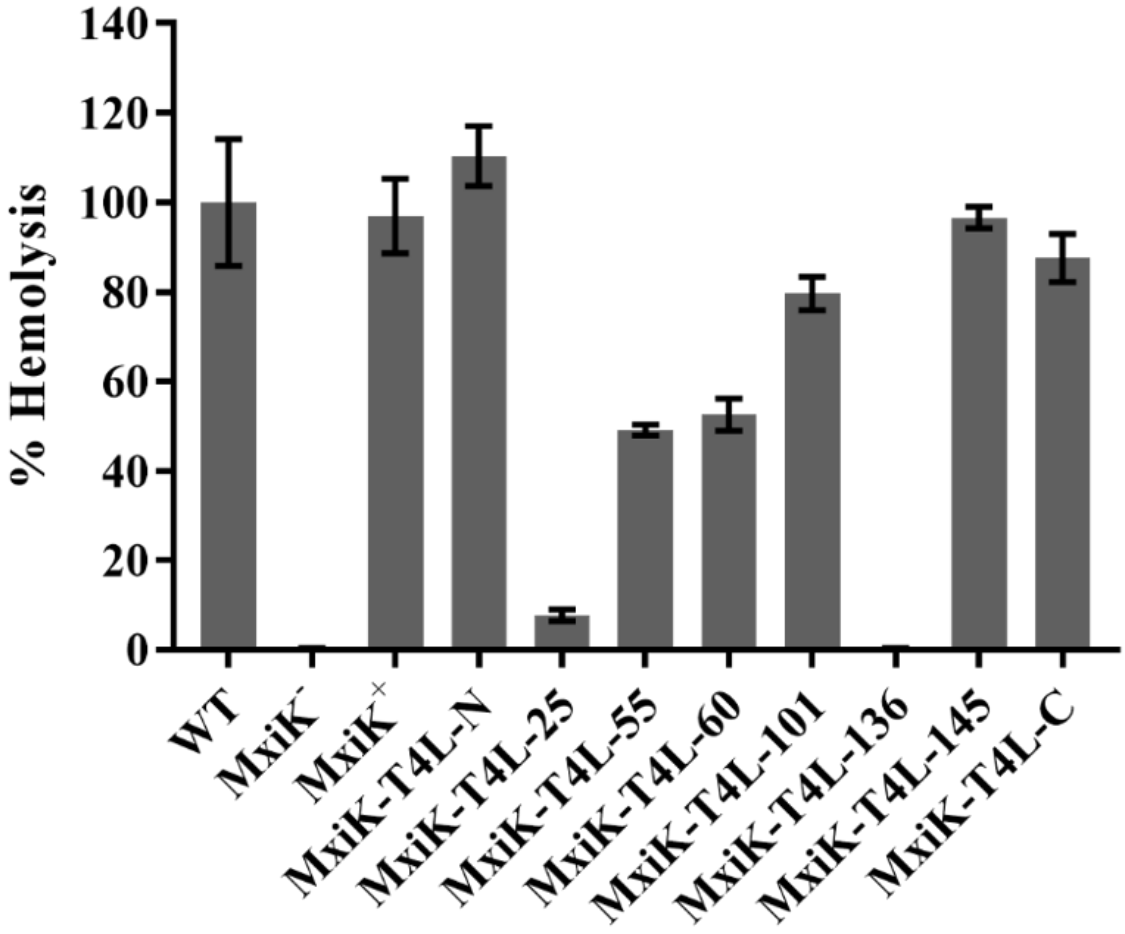

Figure 3.6. Contact-mediated hemolysis assay for the MxiK-T4L insertion *Shigella* mutants. Contact-mediated hemolysis was performed using sheep red blood cells to measure the release of hemoglobin caused by contacted with the bacteria. This is the result of translocon pore formation, which gives rise to osmotic lysis of the cells once the bacteria are dislodged. The release of hemoglobin from the red blood cells was measured by absorbance at 545 nm of the supernatant following centrifugation to remove the whole cells. We compared the result of each mutant with that of wild-type *S. flexneri* (WT) to calculate percentages of hemolytic activities.

Moreover, only this fusion protein could be obtained in the soluble fraction when it was expressed as a recombinant protein in an *E. coli* expression strain, which allowed us to purify the recombinant protein for biophysical analysis (discussed in Chapter 4). Therefore, the MxiK-T4L-C *Shigella* mutant was used for cryo-ET to localize MxiK's position in the SP (done in the laboratory of Jun Liu). To prepare the *Shigella* sample for cryo-ET, this MxiK-T4L fusion protein gene in pWPsf4 was successfully transformed into *mxiK* null *S. flexneri* strain, which was also transformed with the pBS58 plasmid, using the electroporation. Because pBS58 leads the overexpression of FtsQ, FtsA, and FtsZ, the mutant strain with pBS58 undergoes asymmetrical cell division to produce mini-cells. To perform cryo-ET, a single mini-cell was harvested from both wild-type *S. flexneri* and the MxiK-T4L-C mutant for cryo-electron microscopy with subsequent tomographic imaging to observe their relative SP densities. Cryo-ET images and the resulting rendered surface images of the T3SA and with a focus on the SP is shown for wild-type *S. flexneri* (Fig. 3.7A) (57). Next, T3SA from MxiK-T4L-C mutant was observed and found to possess an intact SP. The electron densities around the pod regions from the mutant were then compared with the electron densities from wild-type *S. flexneri* SP. In the difference map, the additional electron densities from T4L were clearly observed, and its position is on the cytoplasmic membrane side of the pod structure confirmed (Fig. 3.7B). To visualize all the components clearly, surface rendering images of the cryo-ET structure were used to better show the positions of T4L (green) and MxiK (orange) positions (Fig. 3.7C). In addition to locating both of these proteins, the Spa33 "complex" position is indicated by the yellow structure (Fig. 3.7C). The T4L position (green) is located inside of the SP "cage" near the cytoplasmic membrane. Thus, MxiK is clearly located immediately beneath the small cytoplasmic domain of the inner membrane ring. In the cryo-ET images of the pod structure from wild-type *S. flexneri*, the MxiK density has a lobed or kidney shape and it clearly

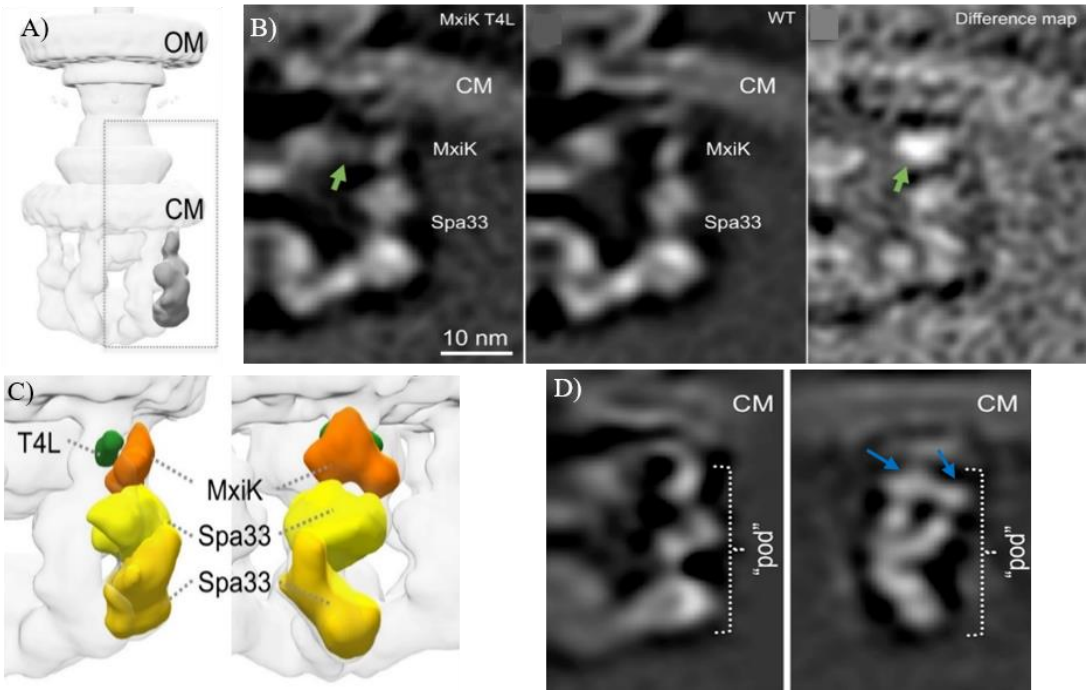

Figure 3.7. Cryo-ET images and its surface renderings for the pod-like structure.

The T3SA from both wild-type and MxiK-T4L-C mutant *S. flexneri* were visualized using cryo-ET techniques to compare their pod structures. A) The surface rendering image of the basal body and SP of the T3SA from wild-type *S. flexneri*. The boxed region from both strains were magnified and overlay to compare their electron densities from cryo-ET. B) The left panel is an enlarged cryo-ET image of the SP from the MxiK-T4L-C mutant. The middle panel is a magnified image of the same area from wild-type *S. flexneri*. The right panel is the difference map between them. The white density is the largest electron density difference between the two strains. The T4L location is indicated by the green arrows in the images. C) A surface rendering of a single pod structure in the SP from MxiK-T4L-C after the localization of the MxiK position. The green density is the T4L position, and the orange region is MxiK position. Spa33 is shown by the yellow density. The right panel is rotated 90 degrees. D) The cryo-ET image of a single pod structure from wild-type *S. flexneri*. The right panel is 90 degree's rotated image. In this image, two high electron density regions were observed for MxiK which are pointed with blue arrows.

makes contact with the Spa33 hetero-oligomer. In addition to the information of MxiK shape, we observed that electron densities of this MxiK position from wild-type *S. flexneri* has two high electron dense regions (Fig. 3.7D).

Bacterial Adenylate Cyclase Two-hybrid (BACTH) experiment to confirm MxiK binding to other proteins.

Based on our hypothesis, the previously unknown region in the pod structure between $MxiG^{Cyt}$ and Spa33 complex is comprised of MxiK, which interacts with each of these proteins. Therefore, interactions between MxiK and $MxiG^{Cyt}$, as well as between MxiK with the Spa33 complex, were tested using BACTH analyses. All genes were successfully cloned into the appropriate plasmids and transformed into *E. coli BTH101*, which is described above. For the MxiK interaction with $MxiG^{Cyt}$, *BTH101* strains, which possess both MxiK in pKT25 and $MxiG^{Cyt}$ in pUT18C, showed red colonies on MacConkey agar plates with maltose and blue colonies on M63 plates with X-gal. For the interaction of MxiK with $Spa33^{WT}$, *BTH101* strains which possess both MxiK in pUT18C and $Spa33^{WT}$ in pKT25 also showed red colonies and blue colonies on MacConkey plates with maltose and M63 plates with X-gal, respectively (Fig. 3.8).

In addition to testing the interaction of MxiK with $Spa33^{WT}$, interaction of MxiK with $Spa33^{Cterm}$ and MxiK with $Spa33^{FL}$ were tested. For the interaction between MxiK and $Spa33^{Cterm}$, all *BTH101* colonies from all combinations of MxiK and $Spa33^{Cterm}$ in plasmids for BACTH experiment gave white colonies (no interaction detected). In contrast to this interaction, some of combinations that possessed MxiK and $Spa33^{FL}$ genes in the plasmids gave colored colonies on both types of indicator plates, indicating a positive interaction (Fig. 3.8).

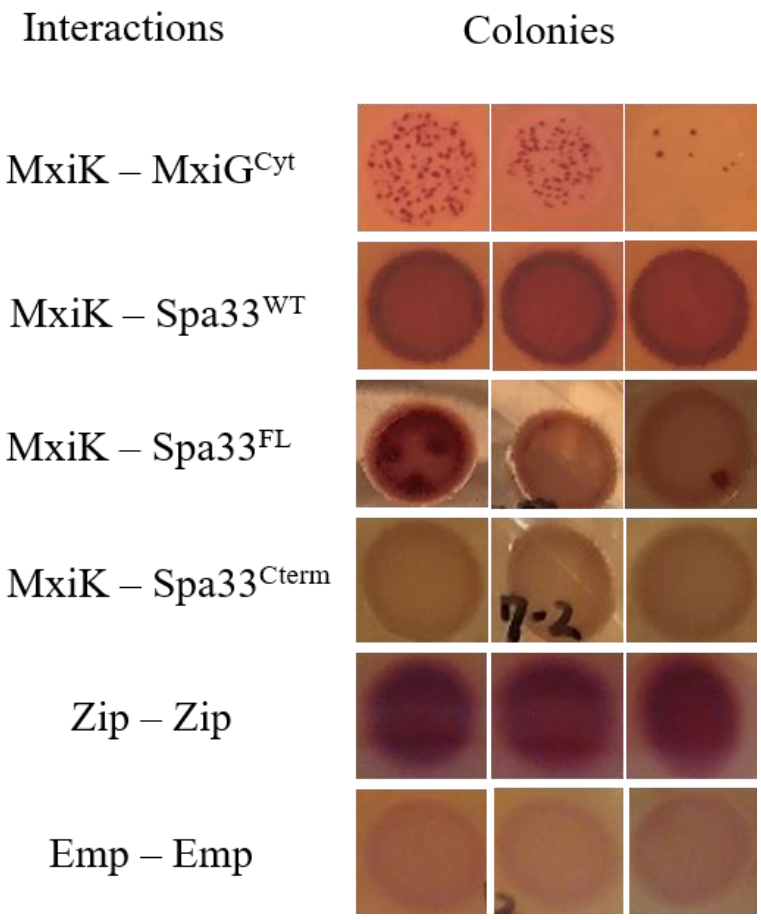

Figure 3.8. BACTH analysis of interactions among MxiK, MxiG^{Cyt}, and Spa33.

Each of the proposed interactions based on cryo-ET analyses were examined in a BACTH experiment. Bacterial culture for MxiK-MxiG^{Cyt} interaction was often condensed to spots on the plates, which was interpreted as a weak color change, possibly due to weak binding. For testing the MxiK-MxiG^{Cyt} interaction, *mxiK* was in pKT25 and *mxiG^{Cyt}* was in pUT18C which were transformed into *BTH101*. The strain which possessed *mxiK* in pUT18C and *spa33^{WT}* in pKT25 gave red colonies on the MacConkey agar plates. *mxiK* in pUT18C and *spa33^{FL}* in pKT25 also gave colored colonies, however, a few colonies were white. The same combination, but use *spa33^{Cterm}* in pKT25 instead of *spa33^{FL}*, in *BTH101* gave white colonies in all cases.

3.3 Conclusions

Based on the results of secretion and hemolytic activities, most of the MxiK-T4L insertion mutants restored the T3SS function. This fact suggests that the T4L insertion in most of loop regions maintained a functional MxiK structure within the SP (Fig. 3.5 and 3.6). This is in agreement with what was previously found for T4L insertion into the translocator protein IpaB (85). Based on results of both assays, T4L at N- and C-termini perfectly restored T3SS activities, therefore, both termini are probably not directly involved MxiK functions. Moreover, T4L insertion at residue 145 also restored T3SS activities, so this loop is also not an important region for MxiK function. Interestingly, the insertion at N-terminal half at residues 25, 55 and 60 shown relatively reduced T3SS functions, while the insertion at C-terminal half residues 101 and 145 restored relatively high level of activity functions. Perhaps, N-terminal side of MxiK (1 to 60) has more critical roles in MxiK's functions.

S. flexneri mutant with MxiK-T4L-C was used for cryo-ET to localize MxiK position in the SP. In the difference map for pod structures between MxiK-T4L-C mutant and wild-type *S. flexneri*, it is clear that pod structure from the mutant possesses the additional electron densities from T4L, which is indicated by green arrows in Figure 3.7B. Since T4L is fused at C-terminal side of MxiK, this cryo-ET images suggests that MxiK C-terminus is oriented to the inside of pod structure (Fig. 3.7B and C). Therefore, cryo-ET in parallel with mutagenesis has revealed that the MxiK position is just beneath the cytoplasmic side of inner membrane ring, which is $MxiG^{Cyt}$, and its C-terminal side faces the inside of SP (Fig. 3.7C). In addition to the MxiK position, the cryo-ET images showed that the MxiK region in the cryo-ET image has two highly electron dense regions (Fig. 3.7D). This suggests that MxiK has two subdomains in its structure. It is probable

that each subdomain is globular in structure. Since these two high electron dense regions face the Spa33 complex, these subdomains might be used for the Spa33 interaction in the main pod structure (Fig. 3.7D). One of the subdomains also faces the cytoplasmic side of inner membrane ring, so that is possibly the part of MxiK that interacts with the MxiG^{Cyt}.

BACTH analysis was used to confirm the identity of MxiK's binding partners. Based on *in situ* images, MxiK binds to both MxiG^{Cyt} and Spa33. In the BACTH experiments, *mxiK* in pKT25 with *mxiG^{Cyt}* in pUT18C and *mxiK* in pUT18C with *spa33^{WT}* in pKT25 in *E. coli BTH101*, gave rise to colored colonies (a positive result) (Fig. 3.8). Therefore, MxiK interacts with both MxiG^{Cyt} and Spa33^{WT}. These results support the proposed MxiK position based on the cryo-ET images (Fig. 3.7). Since the interaction between MxiK and MxiG^{Cyt} was found to take longer to be observed in the BACTH experiments, this interaction is probably weaker than the interaction between MxiK and Spa33^{WT}. Based on this weak (possibly transient) interaction, perhaps the six-fold symmetrical pod structure in the SP rotate along the inner membrane ring as observed for the rotary F0-F1 ATPase (86,87). In such a model, the interaction between the pod structure and inner membrane ring (MxiK and MxiG^{Cyt}) would need to be weak enough to allow for molecular dynamics. In contrast to this interaction, the interaction between MxiK and Spa33^{WT} must be strong enough to build the pod structure to connect with Spa47 at the bottom of the SP.

In addition to testing the interactions among MxiK, MxiG^{Cyt}, and Spa33^{WT}, BACTH experiments were used to test for the interaction of MxiK and key Spa33 variants (Fig. 3.8). These results indicate how MxiK may interact with the Spa33 hetero-multimeric complex. Because all *BTH101* colonies for testing the interaction between MxiK and Spa33^{Cterm} showed white colonies, the Spa33 C-terminal complex is probably not involved in the MxiK interaction. In contrast, some *BTH101* colonies combinations showed positive results on both X-gal and MacConkey agar plates

for the interaction between MxiK and Spa33^{FL}. Therefore, Spa33 without its C-terminal domains is still able to interact with MxiK. Importantly, not all colonies showed positive results on these plates, so Spa33 without its C-terminal domains may only weakly interact with MxiK. As mentioned in Chapter 1, the Spa33 C-terminal complex is probably required to stabilize or control the conformation of the Spa33^{FL} structure within its complex. These BACTH results might suggest that the Spa33 C-terminal complex is required for Spa33^{FL} to strongly interact with MxiK.

In this chapter, MxiK's position in the SP has been determined using a combination of mutagenesis and cryo-ET techniques. The cryo-ET images have also provided information about the overall structure of MxiK in the absence of high resolution crystallographic information. The BACTH experiments agreed with the MxiK position seen in the cryo-ET images and its binding partners, MxiG^{Cyt} and Spa33, which MxiK interact with Spa33^{FL} part. Since cryo-ET images of the T3SA from both *mxiK* null (Fig. 3.1) and *spa33* null *S. flexneri* strains are almost identical in architecture (no SP or needle formation) (45), the interaction between MxiK and Spa33 forms an essential single unit in the SP, which is required for the SP and needle assembly. Based on the MxiK position and its binding partners, MxiK probably acts as adaptor protein between the cytoplasmic side of 24-fold symmetrical inner membrane ring and six-fold symmetrical pod structure in the SP, which is also essential for needle assembly and subsequent secretion activities.

Chapter 4 Molecular Basis for the Interaction of MxiK with MxiG and Spa33

4.1 Introduction

Using a combination of mutagenesis, biochemistry and cryo-ET imaging techniques, we have shown that MxiK is located on the cytoplasmic side of the inner membrane as part of the pod structure that makes up the cytoplasmic sorting platform (SP) of the *Shigella* T3SA. After localizing MxiK's position, all of the SP components' positions are now known (Fig. 4.1) (57). MxiK and multiple copies of Spa33 form a complex (referred to as a "pod") that is required for assembly of the entire SP. As part of the pod structure, MxiK interacts with the cytoplasmic domain of MxiG ($MxiG^{Cyt}$), which is a component of the inner membrane ring in the basal body. The bottom part of the Spa33 complex then connects the pods with the central hub protein (the Spa47 ATPase) via radial spokes comprised of MxiN. Importantly, MxiG and its cytoplasmic domain form a 24-fold continuous symmetrical ring while the pod structures form six-fold discontinuous symmetrical pseudo-ring (homologous to the flagella C-ring) (Fig. 4.1B). The interaction between $MxiG^{Cyt}$ and MxiK, therefore, provides a symmetry transition between the inner membrane ring of the basal body and the pod structures of the SP. Since the cryo-ET image of T3SA from a *mxiK* null *S. flexneri* strain lacks the entire SP and the extracellular needle (Fig. 3.1 in Chapter 3), it is clear that the interaction between these two proteins has an important role for the SP functions. In addition to the importance of the $MxiG^{Cyt}$ and MxiK interaction, the interaction between MxiK and Spa33 is also required to develop a functional SP because the architecture of the T3SA from a *Shigella spa33* null strain also fails to assemble the SP and needle (45), which is identical to what is seen for the *Shigella mxiK* null strain. Based on cryo-ET images of the T3SA from *mxiK* null and *spa33* null strains, both the interaction of $MxiG^{Cyt}$ with MxiK and the Spa33 interaction with

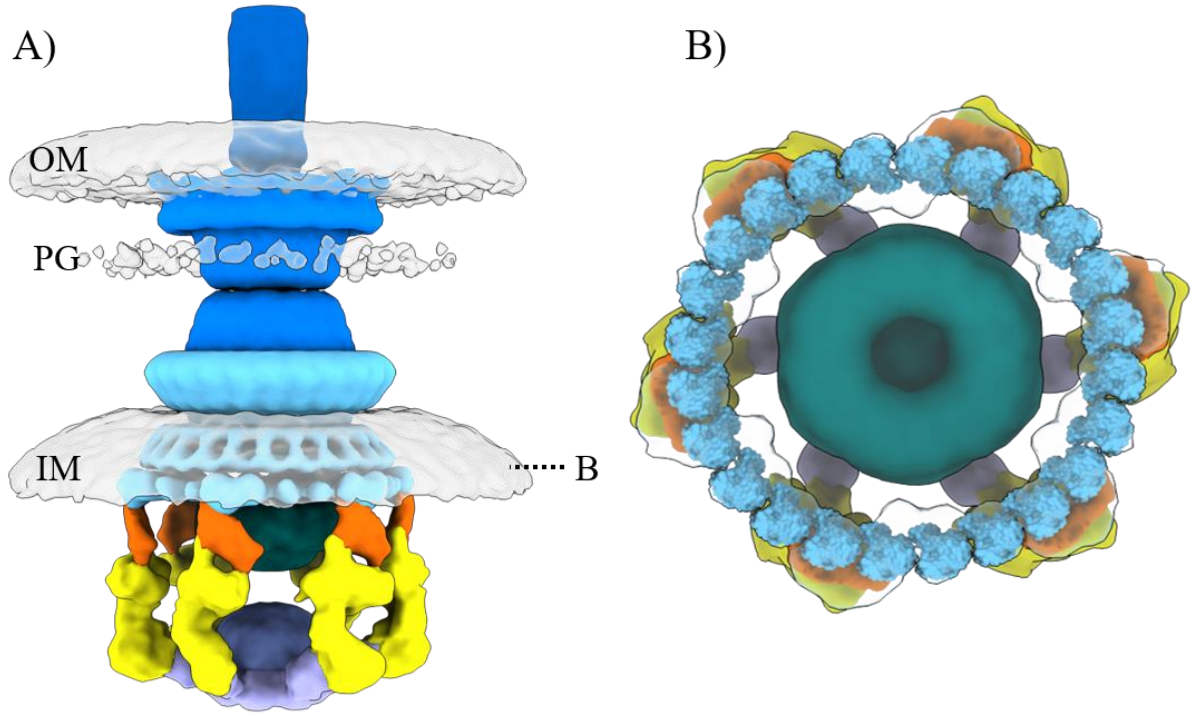

Figure 4.1. Surface rendering for the overall architecture of the *Shigella* T3SA.

A) The overall architecture of *Shigella* T3SA is shown in these surface rendering based on cryo-ET imaging. Each component position in the SP is indicated with different colors. The MxiG^{Cyt} (cyan) is located on the cytoplasmic side of the inner membrane. MxiK (orange) is just beneath MxiG^{Cyt}, and Spa33 (yellow) makes up the bulk of the pod structures. MxiN (purple) is at the bottom of the SP to connect the central hub with the pods. B) A top view of the SP is shown. MxiG^{Cyt} forms 24-fold continuous symmetrical ring, and the pod structure (MxiK and the Spa33 complex) form a six-fold symmetrical discontinuous ring. The pod array is directly overlaid by the MxiG^{Cyt} ring. MxiN is also forms a six-fold radial symmetry at the bottom.

MxiK are required to assemble a functional SP and this is needed to secrete the needle proteins from the bacterial cytoplasm to extracellular environment. These interactions are essential for generation of the complete T3SA, however, how each component interacts with the others is still unknown. In this chapter, I will describe a combination of the mutagenesis (the insertional and substitutional mutations), cryo-ET techniques, and BACTH experiments to reveal new details for the molecular basis of these interactions.

High resolution structures for MxiG^{Cyt} have already been determined using NMR and X-ray crystallographic techniques (56,62). MxiG^{Cyt} is a globular structure with a β-strand sandwich fold that is in the family of proteins known as Forkhead-associated (FHA) domains (Fig. 4.2A) (60,61). FHA domains functions were originally known to be involvement in recognizing phosphorylated threonine residues to initiate protein-protein interactions in eukaryotic cells (60,61), however, while MxiG^{Cyt} contains some of the consensus residues of the canonical FHA domain family, the relationship between these residues and its functions in the T3SS are poorly understood. One previous report proposed that Arg39 and Ser61, which are the consensus residues found in MxiG^{Cyt}, are functionally important for interacting with phosphorylated Spa33 peptides (62). In that report, introducing substitution mutations at these residues reduced secretion activities for the *Shigella* T3SS (62). However, the interaction between MxiG^{Cyt} and phosphorylated Spa33 peptides could not be reproduced independently using Biolayer Interferometry (BLI) in our laboratory. The latter is in agreement with the fact position of Spa33 in cryo-ET images indicates that Spa33's binding partners are MxiK and MxiN – not MxiG. In contrast, another previous report argued that introducing mutations into Arg39, Ser61, and Ser63 in MxiG^{Cyt} does not affect the secretion of Ipa proteins (56). For these reasons, the relationship between functions of MxiG^{Cyt} and T3SS activities is still unclear even though MxiG^{Cyt} and its homologous structures and

A)

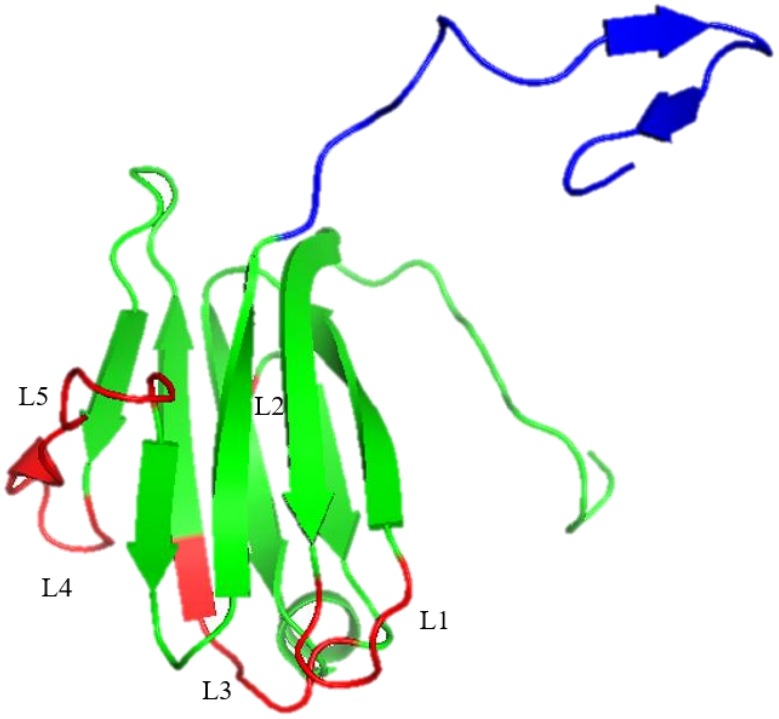

B)

MSEAKNSNLAPFRLLVKLTNGVGDEFPLYY 30

GNNLIVLGRTIETLEFGNDNFPENIIPVTD 60

SKSDGIIYLTISKDNICQFSDEKGEQIDIN 90

SQFNSFEYDGISFHLKNMREDKSRGHILNG 120

MYKNHS 126

Figure 4.2. Crystal structure of MxiG^{Cyt}.

A) The crystal structure of MxiG^{Cyt} from PDB is shown here (PDB ID: 4A4Y). MxiG has FHA domain. Red color loops in this figure are regions which were targeted for the substitutional mutations. L1 is 18 to 22 residues in MxiG, L2 is 47 to 52, L3 is 61 to 66, L4 is 81 to 85, and L5 is 86 to 94. Blue region in this structure is the linker region which connects with MxiG periplasmic domain via the transmembrane region. B) Amino acid sequence for MxiG^{Cyt} is shown. The underline is the linker region which was target for the mutagenesis.

positions are well known. Furthermore, while it is largely agreed that FHA domains are generally involved in mediating protein-protein interactions, not all of these interactions involve recognition of phosphopeptides (60,61,88,89).

In the overall MxiG structure, $MxiG^{Cyt}$ is connected to a single pass transmembrane helix via a relatively long (19 amino acids) loop with two short β-sheets (referred to as a "linker") (Fig. 4.2). This linker appears to be quite flexible and this is probably why $MxiG^{Cyt}$ was not visualized clearly in cryo-ET images prior to our most recent studies. We hypothesize that this linker is a flexible region allows $MxiG^{Cyt}$ to adopt multiple positions and this may provide the movement needed for the dynamic aspects of SP function. The periplasmic domain of MxiG ($MxiG^{Peri}$) contributes to the formation of a tightly packed continuous 24-fold symmetry inner membrane ring, however, the smaller $MxiG^{Cyt}$ does, in fact, have the potential to adopt different degrees of packing (57). In fact, as mentioned in Chapter 1, the 24 PrgH proteins that form the *Salmonella* inner membrane ring pack tightly in the periplasmic compartment, but their cytoplasmic domains can rearrange to form six-fold symmetrical clusters that associate with the MxiK homologue OrgA (59). One difference between the systems, however, is that although overall the cytoplasmic domain of PrgH ($PrgH^{Cyt}$) is an FHA domain that is homologous to $MxiG^{Cyt}$ (90), the linker region in $PrgH^{Cyt}$ is longer than the linker in $MxiG^{Cyt}$. Therefore, it is possible that this variation in linker length results in the different degrees of clustering for the FHA domain in the *Shigella* inner membrane ring.

To begin our investigation of the molecular basis for the observed protein-protein interactions within the SP, we constructed a series of alanine substitutions into the loops regions of $MxiG^{Cyt}$ on what is defined as the apical face of the FHA domain (the face opposite where the domain connects to the linker peptide) (Fig. 4.2A). These experiments were designed to determine

the important sequences or regions involved in its interaction with MxiK. Because the residues Ser61 and Ser63 were proposed by others to be key residues for MxiG^{Cyt} functions, alanine residues were used to replace all the residues from 61 to 66 in MxiG^{Cyt} (MxiG$^{61\text{-}66\ Ala}$). As a second target, we introduced the same substitution for neighboring loop region, which is residues 81 to 85 (MxiG$^{81\text{-}85\ Ala}$). These separate loop substitutions were cloned into the expression vector pWPsf4, which was then used to transform a *mxiG* null *Shigella* strain. Although Ser61 substitution was reported to negatively affect type III secretion (62), we found that that introducing each of our Ala loop substitutions (MxiG$^{61\text{-}66\ Ala}$ and MxiG$^{81\text{-}85\ Ala}$) did not adversely affect T3SS function (presented below in the Results section). In addition to introducing these mutations, other loops predicted to interface with MxiK in the SP were replaced to continuous alanine residues, however, all of these mutants also failed to negatively impact MxiG functions. Based on these results, we hypothesized that multiple loops in MxiG^{Cyt} may be involved in the MxiK interaction, so we replaced both loop regions, residues 61-66 and 81-85 residues, with Ala residues (giving MxiG$^{61\text{-}66/81\text{-}85\ Ala}$). Interestingly, this mutation completely eliminated *Shigella* T3SS activities, even though the individual mutations did not affect activity. Because this mutant was negative for directing type III secretion, it was used for cryo-ET analysis to explore its impact on the T3SA structure. It was also used in BACTH analyses to determine whether the MxiG$^{61\text{-}66/81\text{-}85\ Ala}$ mutation was able to interact with MxiK.

In other experiments, we explored the relationship between flexibility/length and MxiG function for the linker region that connects MxiG^{Cyt} with the MxiG tansmembrane helix (Fig. 4.2B). To provide additional flexibility into the linker region, five and ten glycine residues were inserted into the linker region, which increased the length of the linker while also adding more flexibility. In contrast to these insertion mutations, we also truncated the number of residues

present within the linker region to restrict the flexibility or range of movement for MxiG^{Cyt}. In this Chapter, we identified the linker mutants that most negatively impacted T3SS activities for further cryo-ET analysis to visualize how the linker region may contribute to SP assembly relative to SP function.

After investigating the loop and linker regions of MxiG^{Cyt}, we turned our attention to MxiK interactions within the SP. Based on MxiK's position in the SP, this protein is proposed to act as an adaptor in the transition from the 24-fold symmetry of the inner membrane ring to the six-fold symmetry of the SP pod structures. Based on both secretion and hemolysis results in Chapter 3, only the *S. flexneri* mutant with T4L insertion at residue 136 in MxiK (MxiK-T4L-136) completely disrupted T3SS function (Fig. 3.5 and 3.6 in Chapter 3). To understand why this MxiK mutant could not restore SP function, cryo-ET was performed to visualize the entire architecture of the T3SA. Interestingly, the SP and needle are completely absent from the T3SA for this mutant, which is the same phenotype seen for the T3SA in the *mxiK* null strain (shown below in Results). To determine why T4L insertion at residue 136 of MxiK eliminated T3SA function, we explored three possibilities: 1) the fusion protein is not expressed in the *S. flexneri* strain; 2) there is disruption of the MxiK structure by the T4L insertion; or 3) there is a disruption of MxiK's interactions with one of its binding partners, MxiG^{Cyt} or Spa33.

To quantify expression of MxiK-T4L fusion proteins in *S. flexneri*, whole bacteria from overnight cultures were lysed, their proteins separated by SDS-PAGE, and immunoblot analysis performed. Guinea pig anti-T4L antibodies were used as the primary antibody to detect the fusion protein. Since the MxiK-T4L-C mutant restores T3SS activities to a *mxiK* null mutant, the strain used to visualize the T3SA by cryo-ET in Chapter 3, this mutant was used as the positive control. In parallel, we determined whether MxiK structure is disrupted by the T4L insertion at residue 136

position. To test the structural features of the fusion proteins, circular dichroism (CD) spectroscopy was used to analyze the secondary structure content and the thermal stability as a measure of protein integrity with functional MxiK-T4L-C once again used as a positive control (91). Although CD spectroscopy is a low resolution technique, it was deemed suitable as it provides a measure of secondary content and can be used to measure thermal stability with only a small amount of the MxiK-T4L fusion protein needing to be purified for such a biophysical analysis (91). In fact, we tested various conditions for MxiK induction in *E. coli* expression strains and tested protein refolding methods following denaturation to try to obtain soluble MxiK, however, all such conditions initially failed. This made it difficult to analyze the MxiK structure. Eventually, the T4L fusion at the MxiK C-terminus allowed us to express soluble MxiK fusion protein using a mild detergent. The amount of protein purified was enough to allow for CD spectroscopy of the fusion protein.

As mentioned, because MxiK-T4L-C in *Shigella* restored its T3SS activities, its CD spectrum and melting temperature (Tm) was used as a positive control for comparisons with the same properties for MxiK-T4L-136, which is unable to promote T3SS activities in *Shigella*. It should be mentioned, however, that T4L is an α-helical protein like MxiK is predicted to be (Fig. 3.2 in Chapter 3). Therefore, the CD spectrum for T4L alone in the same buffer condition as used for the MxiK-T4L fusion proteins was performed to determine the contribution that T4L makes to the spectra of these MxiK fusion proteins. Lastly, BACTH analyses were carried out to determine how the T4L insertion at residue 136 affects the interaction of MxiK with its binding partners, $MxiG^{Cyt}$ and Spa33. This BACTH experiment could also provide information on MxiK's orientation within the SP. The C-terminus of MxiK faces inside of the SP (Fig. 3.7C in Chapter

3). The results of this BACTH experiment might be able to tell us whether residue 136 faces toward $MxiG^{Cyt}$ or Spa33 in the event that it blocks MxiK's association with either protein.

In the end, the MxiK-T4L insertion mutants revealed the importance of a predicted loop containing residue 136 that is important for *Shigella* T3SS functions. To minimize the effect that insertion of T4L might have on MxiK activity and SP assembly, substitution mutations were introduced by replacing MxiK residues 134 to 138 with Ala. We also introduced single point mutations at each residue in the predicted loop region to give a MxiK Ala mutant library. In addition to targeting the region around MxiK residue 136, residues from 51 to 55 were also replaced with Ala based on preliminary data generated using Biolayer Interferometry (BLI) and fluorescence polarization (FP) data generated by Dr. Meenakumari Muthuramalingam, which suggested that peptides from this region could bind to immobilized $MxiG^{Cyt}$ (data not shown) (57). These findings indicated that a peptide spanning MxiK residues 50 to 60 could be involved in its interaction with $MxiG^{Cyt}$ and thus might be important for the MxiK-MxiG interaction. To identify important residues in this region, MxiK point mutants were generated and these results are also provided below. Secretion assays and contact-mediated hemolysis assays were used to test the effects of these mutations on MxiK T3SS activities. To analyze structural effects of these alanine substitution mutations, they were introduced into the MxiK-T4L-C fusion protein for CD spectroscopic analysis to compare their secondary structures and thermal stabilities with the spectrum of MxiK-T4L-C having a wild-type MxiK sequence. BACTH analyses were also conducted with all of these mutants to determine how binding to $MxiG^{Cyt}$ and Spa33 was affected.

4.2 Results

Determination of the effects of MxiG loop mutants on T3SS function and interactions with MxiK.

Residues spanning 18 to 22, 47 to 52, 61 to 66, 81 to 85, and 86 to 94 in MxiG^{Cyt} are loop regions that are on the apical face of this FHA domain and which are proposed to face MxiK within the SP. These loops were mutagenized to contain all Ala residues and the resulting *mxiG* genes were cloned into pWPsf4 for expression in a *mxiG* null *Shigella* strain to monitor their ability to restore T3SS functions to this strain. As alluded to above, two loops (61-66 and 81-85) were also simultaneously replaced with Ala residues (MxiG$^{61\text{-}66/81\text{-}85\ Ala}$). To test T3SS activities for these mutants in *S. flexneri*, *mxiG* null *S. flexneri* strain was complemented with these mutant genes followed by conducting contact-mediated hemolysis and overnight steady state secretion assays (Fig. 4.3A and B). Interestingly, MxiG mutants which possess continuous substitutional mutation at individual loops almost completely restored hemolytic activity and IpaB secretion. Only the mutant which introduced Ala substitutions in two of the loops (MxiG$^{61\text{-}66/81\text{-}85\ Ala}$) disrupted both hemolysis and IpaB secretion activities.

Cryo-ET image for MxiG$^{61\text{-}66/81\text{-}85\ Ala}$ and MxiK-T4L-136 mutants.

MxiG$^{61\text{-}66/81\text{-}85\ Ala}$ mutant in pWPsf4 and the T4L insertion at 136 residues of MxiK (MxiK-T4L-136) in pWPSf4 were successfully transformed into *mxiG* null and *mxiK* null *S. flexneri* strain with pBS58, respectively, for cryo-ET. After harvesting mini-cells for both mutants, the T3SA in the mini-cells was visualized using cryo-ET techniques (Fig. 4.4) (57). T3SA from MxiG$^{61\text{-}66/81\text{-}85\ Ala}$ (Fig. 4.4A and C) and MxiK-T4L-136 (Fig. 4.4B and D) mutants still possess the T3SA basal

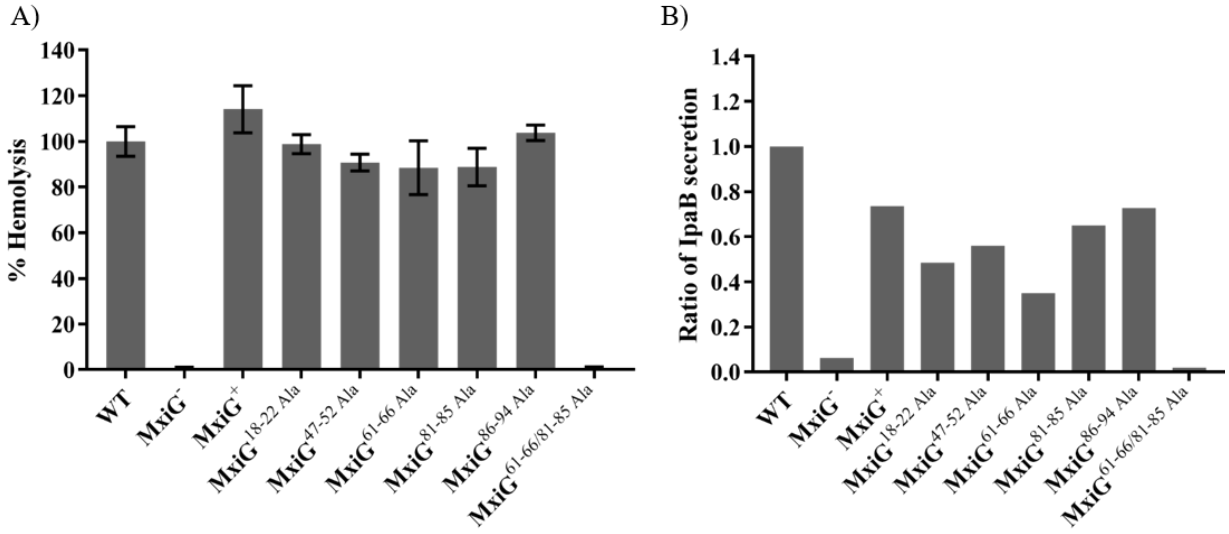

Figure 4.3. Hemolytic activities and IpaB secretion for the MxiG loop mutants.

A) Translocon formation by the T3SS from *S. flexneri* with each MxiG loop Ala mutant was examined using a contact-mediated hemolysis assay. We calculated the relative hemolysis based on the wild-type *S. flexneri* (WT). The *mxiG* null *S. flexneri* strain (MxiG$^-$) and this strain complemented with wild-type *mxiG* (MxiG$^+$) were also used for controls. All targeted loops, which are replaced with Ala residues, are predicted to face MxiK within the SP. B) The secretion of Ipa proteins was examined using an overnight steady state secretion assay. Protein in the culture supernatant of the overnight culture was precipitated with TCA, solubilized in SDS sample buffer and the proteins separated by SDS-PAGE. IpaB was then detected by immunoblot analysis using rabbit anti-IpaB serum and a secondary antibody with an infrared probe. The signals from IpaB in the immunoblot were used to calculate the ratio of IpaB secretion relative to that secreted by the wild-type *Shigella* (WT).

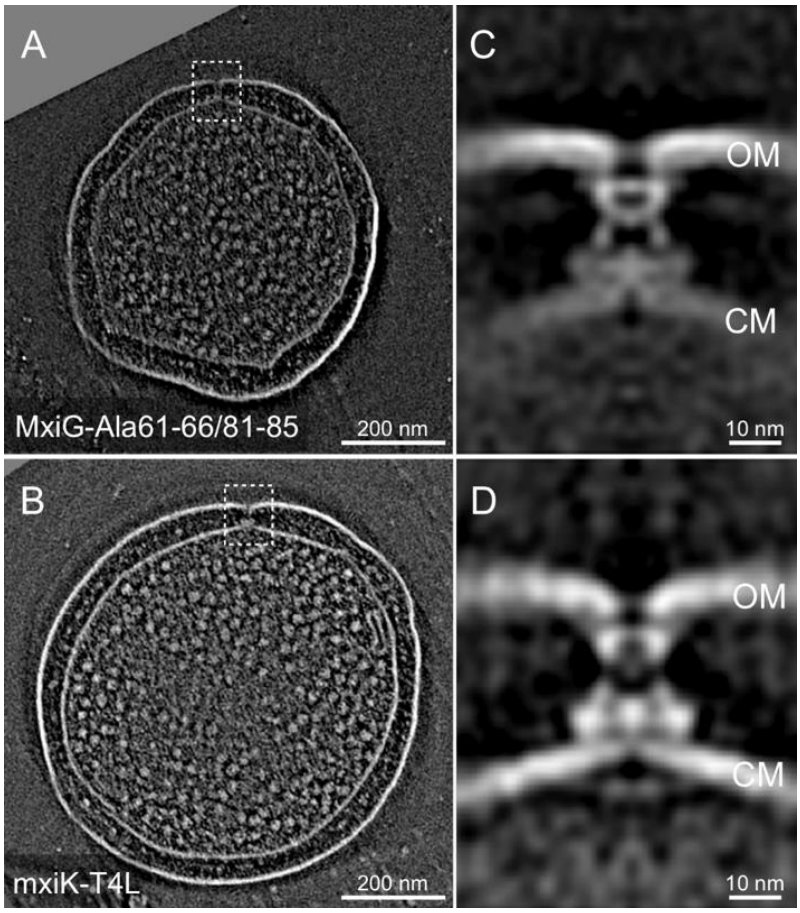

Figure 4.4. Cryo-ET images for the T3SA from MxiG$^{61\text{-}66/81\text{-}85\ Ala}$ and MxiK-T4L-136 *Shigella* mutants.

A) A mini-cell from the *Shigella* MxiG$^{61\text{-}66/81\text{-}85\ Ala}$ mutant strain. The square region contains a T3SA, which was used to visualize the overall T3SA architecture using by cryo-ET to generate high resolution images. B) A mini-cell from *Shigella* MxiK-T4L-136 mutant strain. The square region was again used to visualize the overall T3SA architecture. C) A cryo-ET image of T3SA from the MxiG$^{61\text{-}66/81\text{-}85\ Ala}$ mutant. Both the SP and needle are completely absent from the T3SA although the basal body region is clearly observed between the outer membrane (OM) and cytoplasmic membrane (CM). D) A cryo-ET image from the MxiK-T4L-136 mutant. As with the MxiG$^{61\text{-}66/81\text{-}85\ Ala}$ mutant, the T3SA here lacks the entire SP and needle. Once again, the basal body is observed to span the bacterial envelope.

body in the two bacterial membranes, however, electron densities from the SP and needle were not observed in either mutant.

BACTH analysis for MxiG$^{61\text{-}66/81\text{-}85\ Ala}$ mutant.

Previously, *BTH101 E.coli* strain with wild-type *mxiG* in pUT18C and *mxiK* in pKT25 showed red colonies which suggested the positive interaction between two proteins (Fig. 3.8 in Chapter 3), therefore, *mxiG*$^{61\text{-}66/81\text{-}85\ Ala}$ was cloned into pUT18C for this experiment to test its interaction with wild-type *mxiK* in pKT25. The resulting strain gave negative results on both MacConkey agar plates with maltose and M63 plates with X-gal as indicated by the white colonies (Fig. 4.5).

Development of *Shigella* MxiG linker mutants and testing their T3SA.

A library of MxiG linker region mutants was generated to determine how important mobility of the MxiG^{Cyt} FHA domain was for type III secretion. This library included the insertion of strings of glycine residues within the existing linker, truncation of the linker, changing the linker to be identical to the longer PrgH^{Cyt} (homologue from *Salmonella*) and even insertion of T4L into the linker. These linker region mutants were cloned into pWPsf4 and used to transform a *mxiG* null *Shigella* strain. Surprisingly, very few changes in the linker region had any major negative impact on type III secretion. The contact-mediated hemolysis assay was performed to test for T3SA function from these MxiG^{Cyt} linker mutants.

The insertion of five and ten glycine residues completely restored the hemolytic activities of the *mxiG* null strain (data not shown). For the truncated mutations, MxiG$^{d115\ and\ 120}$, MxiG$^{d115\text{-}120}$, MxiG$^{d110\text{-}120}$, MxiG$^{d111\text{-}124}$, and MxiG$^{d108\text{-}120}$, restored the hemolytic activities while MxiG$^{d108\text{-}}$

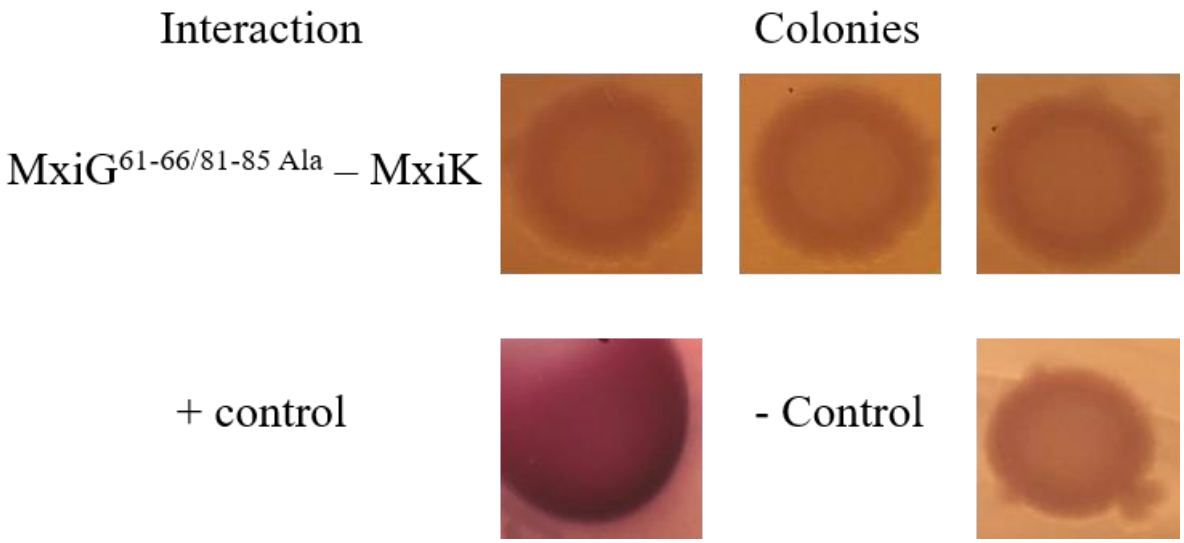

Figure 4.5. BACTH analysis of the interaction between of MxiG$^{61\text{-}66/81\text{-}85\ Ala}$ and MxiK.

For testing the ability of MxiG$^{61\text{-}66/81\text{-}85\ Ala}$ to interact with MxiK, BACTH analysis was used. *mxiG*^{Cyt} with loops 61-66 and 81-85 mutated to Alanine in pUT18C, and *mxiK* in pKT25 were transformed into the *BTH101* strain. Three single colonies from the transformant were grown in LB medium with appropriate antibiotics with 0.5 mM IPTG and spotted onto both MacConkey agar plates with 1.0 % (w/v) maltose and M63 agar plates with X-gal. Color changes in the colonies was then monitored. The strain with leucine zipper genes in both pUT18C and pKT25 are used for the positive control (+ Control) while pUT18C and pKT25 without any genes were used for the negative control (- Control). In this figure, only the results from the MacConkey agar plates with maltose are shown, but the MxiG mutants also failed to show an interaction on the M63 plates with X-gal (data not shown).

^{124} (with almost the entire linker removed) eliminated T3SA function (Fig. 4.6). Interestingly, even the insertion of T4L into the linker failed to eliminate type III secretion (data not shown).

Testing for expression of MxiK-T4L fusion proteins in *S. flexneri*.

T4L antibodies were used to detect the MxiK-T4L fusion protein in whole *S. flexneri* cells. The positive control, MxiK-T4L-C, which restored T3SS activities and used for cryo-ET to observe and localize the T4L and MxiK positions within the SP, showed a positive signal around 38 kDa (Fig. 4.7). The negative controls, *mxiK* null strain and complemented with wild-type *mxiK* in pWPsf4 strain, did not show any T4L signals in their samples. In this assay, MxiK-T4L-25 was also examined because this mutant showed diminished T3SS activities (Fig. 3.5 and 3.6 in Chapter 3). Samples from both MxiK-T4L-25 and MxiK-T4L-136 mutants showed signals around 38 kDa in the immunoblot assay (Fig. 4.7). Although MxiK-T4L-C showed two signals between 25 and 15 kDa region, these signals were weak. These data indicate that the loss of activity for any of these MxiK-T4L mutants was not caused by an expression defect.

Comparison of CD spectra for the MxiK-T4L fusion proteins.

To characterize MxiK-T4L fusion proteins, they were cloned into a plasmid for expression in *E. coli* Tuner (DE3) cells. They were then purified as described in Chapter 2. For structural analysis, we attempted to purify different MxiK-T4L fusion as well as other fusion tag, however, many degradation products were observed during the purification process which made them unsuitable for further study. Eventually, the T4L insertion at C-terminal side of MxiK (MxiK-T4L-C) could be purified as described in Chapter 2 without seeing significant degradation. Using the same purification scheme, we were also able to purify MxiK-T4L-136.

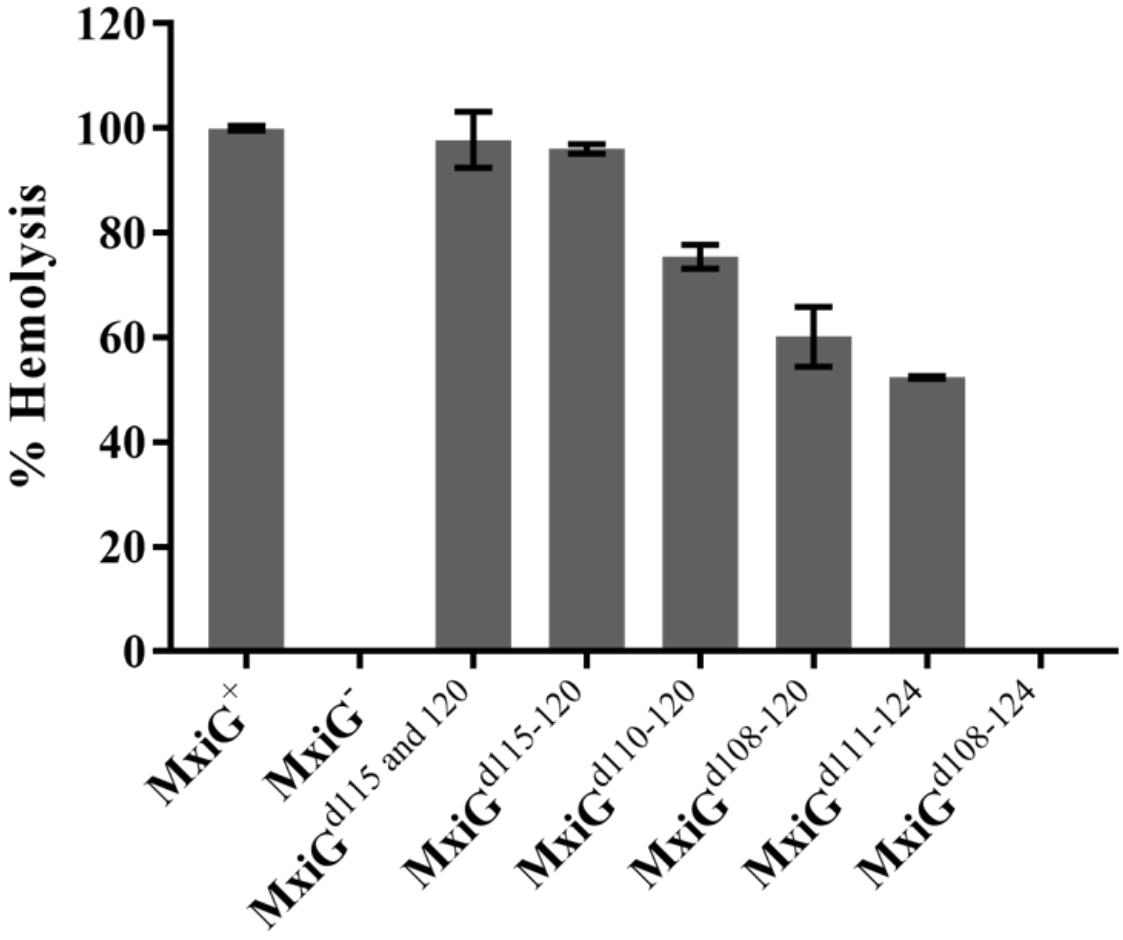

Figure 4.6. Relative hemolytic activities for MxiG truncated linker mutants.

Translocon insertion by the T3SA from *S. flexneri* with each MxiG linker truncation was examined using the contact-mediated hemolysis assay. The relative hemolytic activity was calculated based on a comparison with the wild-type *mxiG* complemented strain (MxiG^{+}) and a *mxiG*$^{-}$ strain was the negative control in this assay.

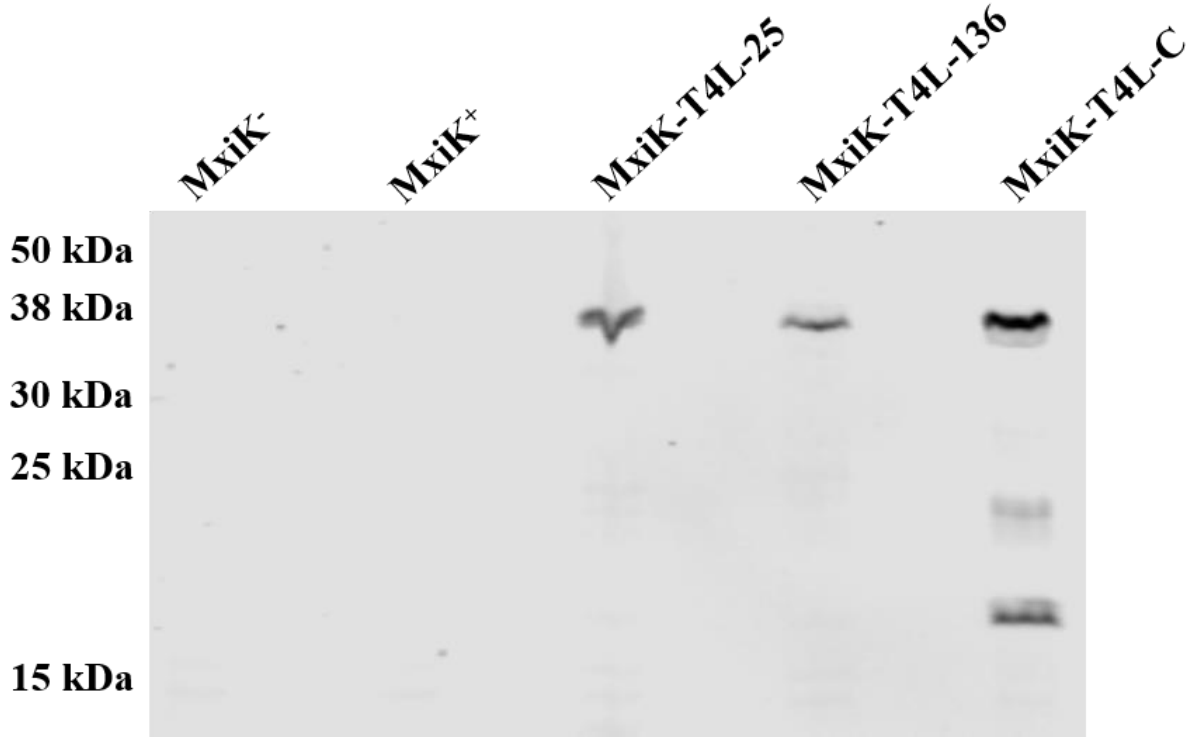

Figure 4.7. Immunoblot detection of T4L in *Shigella* following expression of the MxiK-T4L mutants.

Guinea pig anti-T4L antibody and Donkey anti-guinea pig IgG with an infrared dye were used as the primary and secondary antibodies, respectively, for this immunoblot assay. The negative controls are *mxiK* null strain ($MxiK^-$) and its complement with wild-type *mxiK* ($MxiK^+$), which does not have a T4L component. The signal from the secondary antibody was detected for MxiK-T4L-25, -136, and -C. The size of MxiK-T4L fusion protein is approximately 38.6 kDa, which agrees with the signals in each mutant sample. Signals between 25 and 15 kDa were observed for the MxiK-T4L-C strain, but all expressed the full length fusion.

For CD spectroscopy, purified MxiK-T4L-C, MxiK-T4L-136, and T4L alone were analyzed and their thermal unfolding profiles obtained (see Fig. 4.8) (57). Two negative minima were observed at 208 and 222 nm for all three samples with a positive peak around 197 nm. This is all very characteristic of there being a large α-helical component (91), which is what is predicted for MxiK and is known for T4L (Fig. 3.2 and 3.3 in Chapter 3). When ellipticities at 222 nm were monitored with increasing temperature, an unfolding transition was observed from both MxiK-T4L fusion protein samples, but not for T4L alone. Because of this behavior from T4L, we propose that the fusion protein curves are a result of the MxiK component. Using the Boltzmann sigmoidal equation in GraphPad prism software, we determined the Tm for each sample. The Tm of MxiK-T4L-C was 38.63 °C and the Tm of MxiK-T4L-136 was 42.68 °C. In contrast, the T4L alone did not show a clear transition although its CD spectrum is similar to those of the MxiK-T4L fusion proteins. Based on the similar CD spectra for MxiK-T4L-C and MxiK-T4L-136, and the fact that the thermal stability of MxiK-T4L-136 is greater than that of the active MxiK-T4L-C, it appears that the inactive mutant is still folded properly.

BACTH analysis of MxiK-T4L-136 interactions with MxiG^{Cyt} and Spa33.

To determine whether the T4L insertion at residue 136 affects interactions with its binding partners, BACTH experiments were performed. Because MxiK^{WT} in pKT25 and MxiG^{Cyt} in pUT18C in *E. coli BTH101* strain gave positive results (Fig. 3.8 in Chapter 3), MxiK-T4L-136 in pKT25 and MxiG^{Cyt} in pUT18C were transformed into the strain. When MxiK-T4L-136 was tested with MxiG^{Cyt}, the colonies did eventually turn color, but it took several days to see the result and the positive bacteria appeared as spots within the larger white colony (Fig. 4.9).

MxiK^{WT} in pUT18C and Spa33^{WT} in pKT25 in *E. coli BTH101* strain gave positive results on MacConkey agar plates with maltose and M63 agar plates with X-gal (overall positive control

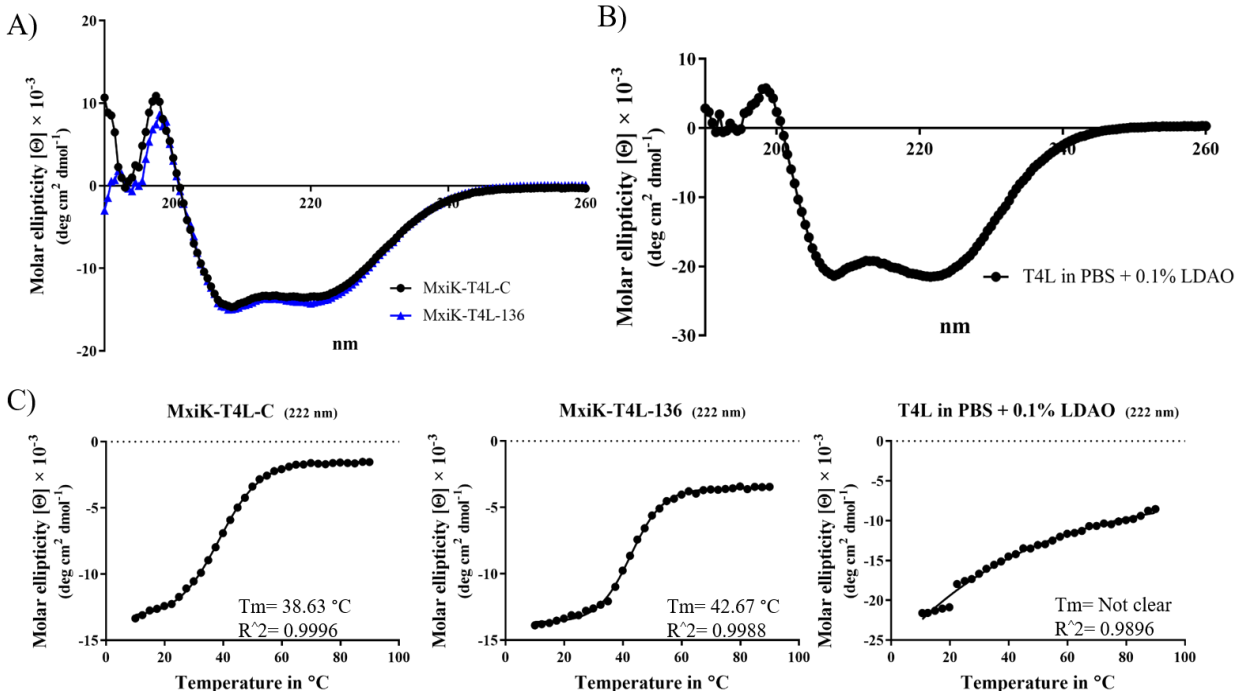

Figure 4.8. The CD spectra for the MxiK-T4L fusion proteins and T4L.

A) The CD spectra for MxiK-T4L-C and MxiK-T4L-136 in PBS with 0.1 % LDAO are overlaid. The two spectra are almost identical with negatives peak around 208 and 222 nm and a positive peak around 197 nm observed. B) The CD spectrum for T4L in PBS containing 0.1 % LDAO is shown. The spectrum for T4L also shows two negative peaks around 208 and 222 nm. C) Molar ellipticity at 222 nm for each protein sample was monitored while increasing the temperature. Both MxiK-T4L-C and MxiK-T4L-136 show clear sigmoidal curves. The Tm is 38.63 °C for MxiK-T4L-C and 42.67 °C for MxiK-T4L-136. T4L alone with 0.1 % LDAO did not show a clear transition, and its Tm could not be determined.

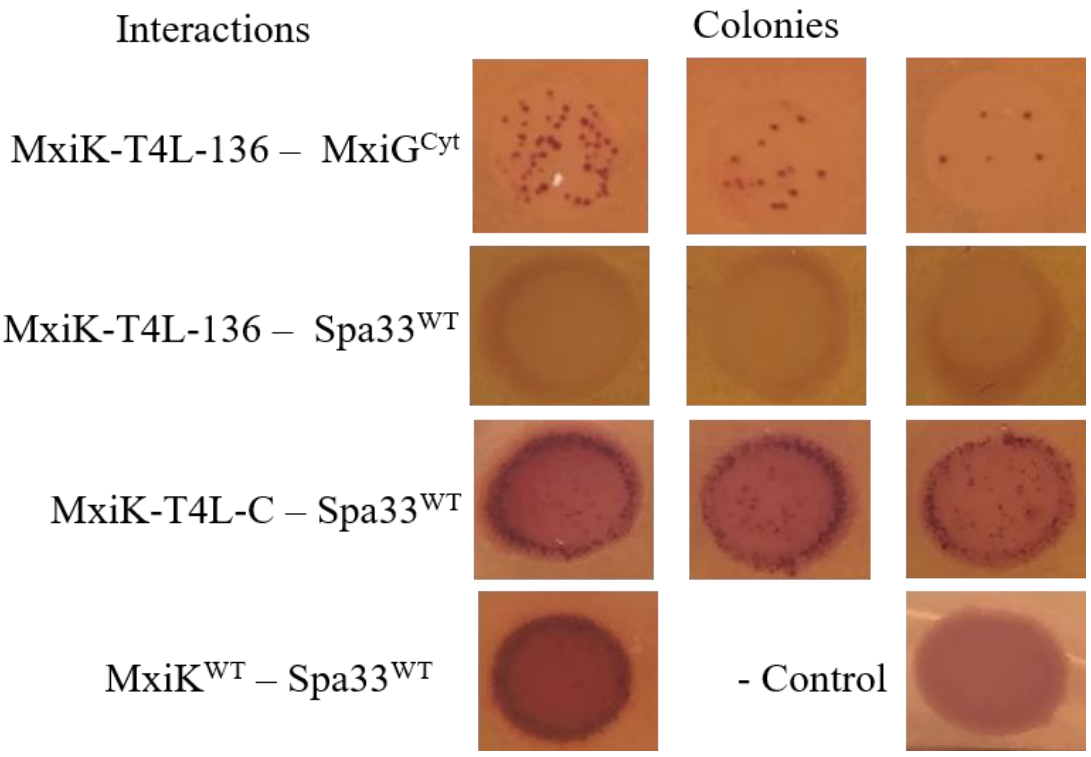

Figure 4.9. BACTH analysis of the interaction of MxiK-T4L-136 with MxiG^{Cyt} and Spa33 on MacConkey agar plates.

To test the interaction of MxiK mutants with MxiG^{Cyt} and Spa33, MxiK-T4L-136 was cloned into pKT25 and MxiG^{Cyt} into pUT18C for BACTH analysis. The plasmids were used to transform *E. coli BTH101*. For testing the interaction with Spa33^{WT}, the MxiK mutant was in pUT18C and Spa33^{WT} in pKT25. These combinations all gave positive results for the wild-type proteins. The MxiK-T4L-136 with MxiG^{Cyt} gave a positive result (top row). The mutant with Spa33^{WT} was negative for the interaction (second row) while MxiK-T4L-C did interact with Spa33^{WT} (third row). The overall positive control in this figure was wild-type MxiK with wild-type Spa33 and empty vectors were used for the negative control (- Control). All BACTH experiments were completed using both MacConkey agar plates with maltose and M63 plates with X-gal (the latter is not shown).

in Fig. 4.9). Likewise, MxiK-T4L-C gave a positive result with Spa33, however, this strain required almost one additional day of incubation to give the positive result and the overall colony was spotty. In contrast, MxiK-T4L-136 gave white colonies on both plates and thus failed to demonstrate an interaction (Fig. 4.9).

Shigella T3SS activity assays for the MxiK Ala substitutions in the loop containing residue 136.

To better explore the importance of the predicted MxiK loop that contains residue 136, single and group Ala substitution mutations were introduced and each *mxiK* mutant was cloned into pWPsf4, which was used to transform a *S. flexneri mxiK* null strain so that their T3SS activities could be monitored. The first activity examined was insertion of the translocon into red blood cells (contact-mediated hemolysis assay). *Shigella* T3SA with five continuous Ala residues from 134 to 138 of MxiK ($MxiK^{134\text{-}138\ Ala}$) had no readily detectable activity and was almost the same as seen for the *mxiK* null strain. The individual point mutations with Ala at positions 134, 136, 137, and 138 restored hemolytic activities, however, the point mutation at residue 135 ($MxiK^{Leu135Ala}$) had dramatically reduced activity (Fig. 4.10).

The IpaB secretion activity for each mutant was tested by comparing IpaB protein secreted into the culture supernatant for overnight cultures. IpaB was detected by immunoblot analysis using rabbit anti-IpaB antiserum with the secondary antibody-dye conjugate detected using an IR imaging system. The $MxiK^{134\text{-}138\ Ala}$ showed dramatically reduced IpaB secretion as did $MxiK^{Leu135Ala}$ (Fig. 4.10). In contrast, IpaB secretion for the single Ala substitutions at residues 134, 136, 137, and 138 were almost at the same level as the wild-type *mxiK* complemented strain ($MxiK^{+}$).

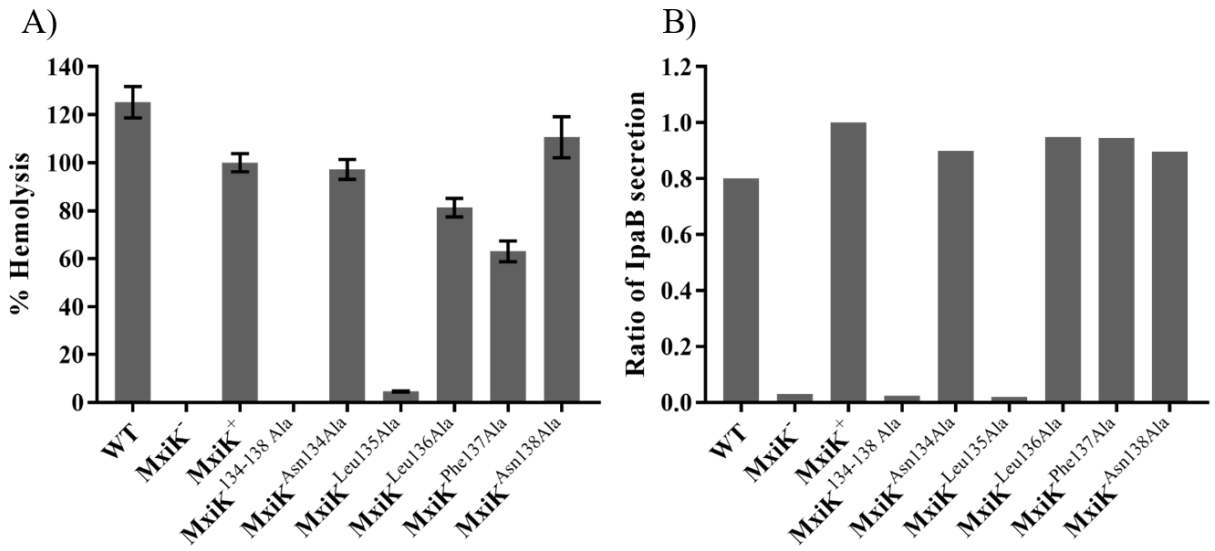

Figure 4.10. Contact-mediated hemolysis and IpaB secretion assays for the *Shigella* MxiK Ala mutants.

A) The hemolysis assay was performed for all the mutants to test for translocon formation. The hemolysis for the wild-type *mxiK* complemented into a *mxiK* null strain ($MxiK^+$) was used to calculate the relative hemolysis for all samples in this experiment. B) For the IpaB secretion assay, secreted IpaB in overnight culture supernatants was quantified by immunoblot analysis. Rabbit anti-IpaB antiserum was used to recognize the IpaB protein and donkey anti-rabbit antibody with an IR dye was used to detect its signals. IpaB signal from $MxiK^+$ was used to calculate ratios for all samples. Relative signals were determined by densitometry.

BACTH experiment for the interaction between MxiK^{Leu135Ala} and Spa33^{WT}.

To determine how the Ala substitution mutations affect the interaction between MxiK and Spa33^{WT}, BACTH analyses were performed. For these experiments, MxiK^{WT} and Spa33^{WT} served as the positive control and the empty vector was the negative control. To start, *mxiK$^{134\text{-}138\ Ala}$* and *mxiK^{Leu135Ala}* were cloned into pUT18C to test interaction for their interaction with Spa33^{WT} being expressed from pKT25 when both plasmids are used to transform *E. coli BTH101* and the bacterial spotted onto both MacConkey agar plates with maltose and M63 agar plates with X-gal to look for color changes. After a few days of growth, only the strain with MxiK^{WT} and Spa33^{WT} showed any color change in the colonies. Both mutant combinations, MxiK$^{134\text{-}138\ Ala}$ with Spa33^{WT} and MxiK^{Leu135Ala} with Spa33^{WT}, only gave rise to white colonies (Fig. 4.11).

***Shigella* T3SS activity assays for the MxiK Ala substitutions in the loop containing residue 51.**

Another region of MxiK targeted for mutagenesis is the predicted loop region near residue 51 of the protein. This is based on the observation that peptides in a library that contain the sequence from 50 to 60 of MxiK are able to bind to immobilized MxiG^{Cyt} based on Biolayer interferometry (BLI) analysis (57). Furthermore, a T4L insertion at residue 55 of MxiK diminished T3SA function (see Fig. 3.5 and 3.6 in Chapter 3). Ala substitution mutations within the region were generated and then cloned into pWPsf4 for expression in a *S. flexneri mxiK* null strain. The function of the resulting T3SA was then tested using our contact-mediated hemolysis assay and by monitoring the secretion of IpaB. The substitution mutations generated included placing five continuous Ala residues in the 51 to 55 position of MxiK (MxiK$^{51\text{-}55\ Ala}$) and then substituting each individual residue in this region with Ala. The MxiK$^{51\text{-}55\ Ala}$ mutant was completely disrupted with regard to hemolysis activity (Fig. 4.12A). Moreover, the single point mutation at residue 53

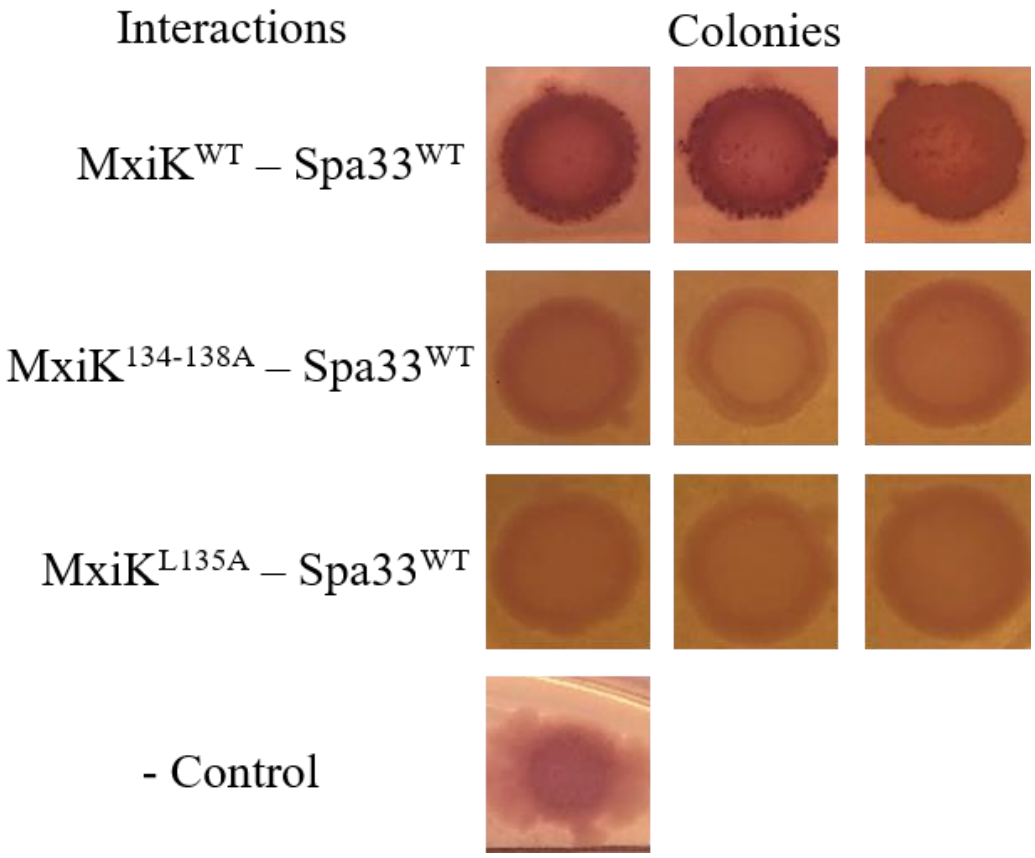

Figure 4.11. BACTH analysis of the interactions between the inactive MxiK Ala substitution mutants and Spa33^{WT}.

MxiK mutant genes were cloned into pUT18C and Spa33^{WT} was cloned into pKT25 and used to transform *E. coli BTH101*. The strain with MxiK$^{134\text{-}138\ Ala}$ and Spa33^{WT} gave only white colonies on MacConkey agar plates with maltose (middle row) and on M63 plates with X-gal (not shown). The strain with MxiK^{Leu135Ala} with Spa33^{WT} gave the same result as the MxiK$^{134\text{-}138\ Ala}$ mutant. The strain with plasmids which encode MxiK^{WT} and Spa33^{WT} was used for the positive control. The negative control was the combination of pUT18C and pKT25 plasmids without gene inserts.

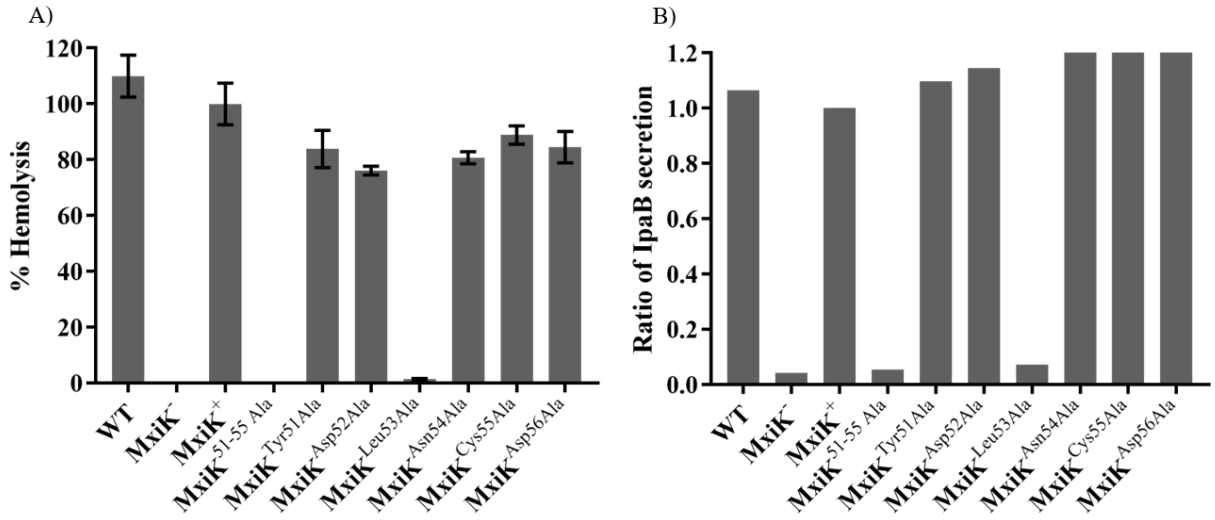

Figure 4.12. Contact-mediated hemolysis assay and secretion assay for MxiK alanine mutants at 51 loop region in *S. flexneri*.

A) The hemolysis assay was performed for all substitutional mutants to test functions of their translocon on the tip complex. The leaked hemoglobin was measured by 545 nm absorbance followed by contacting red blood cells and bacterial samples. The absorbance of wild-type *mxiK* complemented with *mxiK* null strain ($MxiK^+$) was used to calculate the relative hemolysis for all samples. B) The secretion ability of T3SS was analyzed by secreted IpaB protein in soluble part of the overnight cultures. The immunoblot was used to quantify IpaB protein signal in samples. The IpaB signal from $MxiK^+$ was used to calculate the ratio of IpaB signals for all samples.

(MxiK^{Leu53Ala}) was also dramatically reduced in its T3SS activities (Fig. 4.12A). None of the other point mutations (at residues 51, 52, 54, 55, and 56) displayed any negative impact on hemolytic activity (Fig. 4.12A).

The secretion activities of the same set of Ala mutants were then analyzed for IpaB secretion using the immunoblot assay already described (Fig. 4.12B). The IpaB signal from MxiK^{+} was used to calculate relative release of IpaB by the different MxiK mutants. As with the hemolysis assay, MxiK$^{51\text{-}55\ Ala}$ showed almost no IpaB secretion and MxiK^{Leu53Ala} had dramatically reduced IpaB secretion activity. This is in contrast the other Ala point mutants, all of which restored the IpaB secretion phenotype at near wild-type levels.

CD-spectrum for MxiK^{Leu135Ala}-T4L-C and MxiK$^{51\text{-}55\ Ala}$-T4L-C.

To confirm structural effects of the substitutional mutations, CD-spectrum of MxiK^{Leu135Ala}-T4L-C and MxiK$^{51\text{-}55\ Ala}$-T4L-C were compared with MxiK-T4L-C (Fig. 4.8 and 4.13). The point mutation at 135 residues and five continuous Ala at 51 to 55 residues in MxiK were introduced into MxiK-T4L-C in pT7HMT, and then each recombinant protein was purified by same methods as purification of MxiK-T4L-C. Two negative peaks around 208 and 222 nm, which is α-helical property were observed on both spectrum (Fig. 4.13A) (91). Although CD-spectrum from MxiK^{Leu135Ala}-T4L-C shows a small positive peak around 197 nm, spectrum from MxiK^{Leu135Ala}-T4L-C and MxiK$^{51\text{-}55\ Ala}$-T4L-C are almost identical to MxiK-T4L-C, which mutant restores T3SS activities to a *mxiK* null *S. flexneri* strain. (Fig. 3.5, 3.6 in Chapter 3, and Fig. 4.13A). To determine Tm, ellipticity at 222 nm was monitored under increasing temperature. Both recombinant proteins showed clear sigmoid curves, and the Tm are 40.72 °C for MxiK^{Leu135Ala}-T4L-C and 42.36 °C for MxiK$^{51\text{-}55\ Ala}$-T4L-C, which are similar to Tm of MxiK-T4L-C (Fig. 4.8C and 4.13B and C).

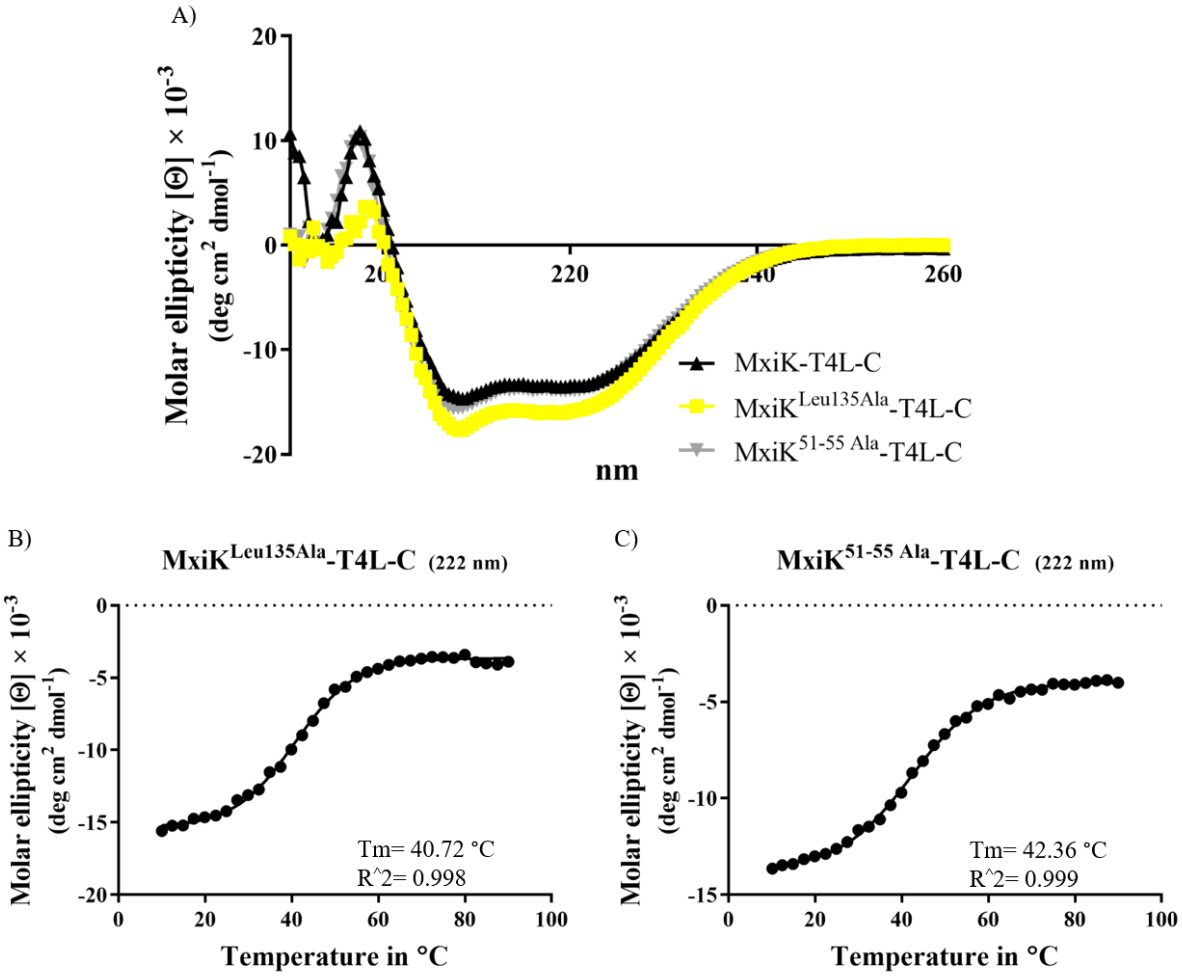

Figure 4.13. CD-spectrum for MxiK-T4L fusion with substitutional mutants.

A) CD-spectrums for MxiK-T4L-C, MxiK^{Leu135Ala}-T4L-C, and MxiK$^{51\text{-}55\ Ala}$-T4L-C in PBS with 0.1 % LDAO are overlay. Two negative peaks around 208 and 222 nm are observed for these three spectrum. B) Ellipticity at 222 nm for MxiK$^{Leu135\ Ala}$-T4L-C was monitored under increasing temperature, and its Tm is 40.72 °C. C) Ellipticity at 222 nm for MxiK$^{51\text{-}55\ Ala}$-T4L-C was monitored under increasing temperature. Its Tm was 42.36 °C.

BACTH analysis for interactions between MxiK^{Leu53Ala} and MxiG^{Cyt} and Spa33.

Both single Ala point mutations at 53 and 56 of *mxiK* were cloned into pUT18C using inverse PCR (described in Chapter 2). *E. coli BTH101* was transformed with each *mxiK* mutant in pUT18C with *spa33*^{WT} in pKT25 and the bacteria were spotted onto MacConkey agar plates containing maltose and M63 agar plates with X-gal. To test for the interaction between the MxiK mutants and MxiG^{Cyt}, *BTH101* was transformed with each *mxiK* mutant in pKT25 and *mxiG*^{Cyt} in pUT18C and the bacteria were spotted onto the MacConkey agar plates with maltose. A leucine zipper fused with T18 and T25 in these plasmids served as a positive control and the empty vectors served as the negative control. The strains expressing MxiK^{Leu53Ala} with Spa33^{WT} showed no color change on either medium while another MxiK point mutant, MxiK^{Asp56Ala}, with Spa33^{WT} did give rise to a color change (Fig. 4.14). Interestingly MxiK^{Leu53Ala} also appeared to be negative for binding to MxiG^{Cyt}, but MxiK^{Asp56Ala} also appeared negative for binding to MxiG^{Cyt}. This is despite the fact that the latter was active for type III secretion in *Shigella*. These experiments are being repeated and parallel methods are being considered to monitor these protein-protein interactions.

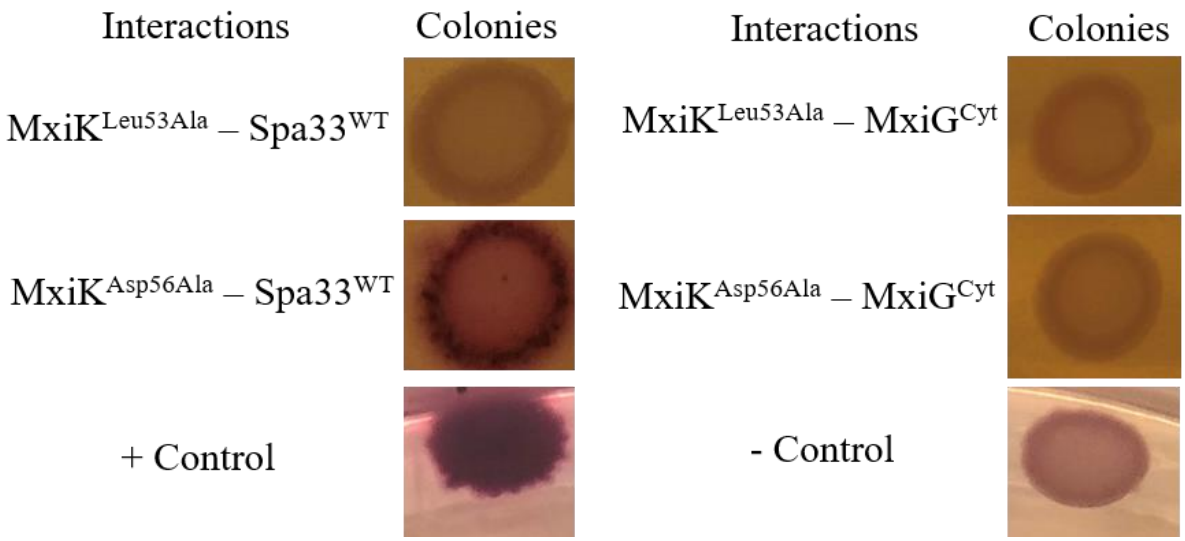

Figure 4.14. BACTH experiments to test for MxiG^{Cyt} and Spa33 binding to the MxiK Ala substitution mutant at residues 53 and 56.

To monitor the binding of MxiK mutants with Spa33^{WT}, each *mxiK* mutant was cloned into pUT18C and *spa33^{WT}* was cloned into pKT25 with both used to transform *E. coli BTH101*. Each was then spotted onto MacConkey agar plates with maltose. For testing the interaction of these MxiK mutants with MxiG^{Cyt}, each *mxiK* mutant was cloned into pKT25 and *mxiG^{Cyt}* was cloned into pUT18C for transforming *BTH101* which was then spotted onto MacConkey agar plates with maltose. The positive control (+ Control) is *BTH101* expressing T18 and T25 fused with leucine zipper genes. The negative control (- Control) is the strain with empty vectors.

4.3 Conclusion

In this investigation, we have elected to study the molecular basis for the interactions that are important for the assembly and function of the *S. flexneri* T3SA sorting platform. It is expected, based on what is known about FHA domains, that the loops on the apical face of $MxiG^{Cyt}$ (a component of the inner membrane ring) face toward the pod structures of the SP. Thus, these were targets for mutagenesis to identify the important regions involved in its interaction with MxiK. Although recent reports said that $MxiG^{Cyt}$ interacts with phosphorylated Spa33 (62), our current cryo-ET images indicate that it is closest to MxiK within the SP (Fig. 3.7 in Chapter 3). In fact, BACTH analyses could not demonstrate an interaction between $MxiG^{Cyt}$ and $Spa33^{WT}$ (data not shown). Moreover, our preliminary data using Biolayer interferometry (BLI) showed that $MxiG^{Cyt}$ does not interact with Spa33 peptides (or even phosphorylated Spa33 peptides). Instead, other members of our group demonstrated that peptides containing the sequence between residues 50 and 60 of MxiK are able to bind to $MxiG^{Cyt}$ (data not shown) (57). Therefore, the focus of this chapter is on the relationship between the loops of $MxiG^{Cyt}$ and their role in directing MxiK interactions.

Most of the loops anticipated to face MxiK were targeted for mutagenesis using Ala substitutions in exchange for each entire loop. Interestingly, when we introduced these mutations into each single loop regions, both hemolytic activity and IpaB secretion were still observed (Fig. 4.3A and B). Only when introducing mutations into both the 61-66 and 81-85 loops ($MxiG^{61\text{-}66/81\text{-}85\ Ala}$) did we disrupt T3SS activities (Fig. 4.3A and B). This mutation also resulted in the complete loss of SP assembly and T3SA needle formation (Fig. 4.4A and C). Importantly, the architecture of the inner membrane ring of the basal body for this MxiG mutant assembles correctly, indicating

that MxiG$^{61\text{-}66/81\text{-}85\ Ala}$ in *Shigella* is expressed and leads to proper assembly of the basal body. We then moved on the test how this mutation in MxiG^{Cyt} affects its interaction with MxiK. In BACTH experiments, the mutant failed to interact with MxiK (Fig. 4.5). This result suggests that the replacement of residues in these two loop regions with Ala disrupts the MxiK interaction and that the 61-66 and 81-85 loops of MxiG^{Cyt} contribute to the symmetry transition seen between the cytoplasmic side of the inner membrane ring and the SP pod structures. This interaction and the resulting symmetry change are essential for SP assembly and T3SA function.

A notable feature of the MxiG^{Cyt} structure is that it has a linker region at its C-terminal end that connects it to the MxiG transmembrane region (Fig. 4.2A). The linker of MxiG is thought to be flexible and this may contribute to molecular dynamics within the SP. When five and ten glycine residues are inserted into its linker region, T3SS activities are not affected (data not shown). In contrast to adding length and flexibility to the linker, when most of the linker is deleted (MxiG$^{d108\text{-}124}$), T3SA functions are disrupted. However, other truncations (MxiG$^{d115\ and\ 120}$, MxiG$^{d115\text{-}120}$, MxiG$^{d110\text{-}120}$, MxiG$^{d108\text{-}120}$, and MxiG$^{d111\text{-}124}$) restored the activities (Fig. 4.6). This results suggests that the linker is required for MxiG activity, but that it can accommodate extensive modification. In fact, we could even insert T4L into the linker and still retain a significant amount of T3SA activity (almost 50 %).

The MxiG binding partner, MxiK, is also an essential component of the *Shigella* T3SS SP. A *mxiK* null strain of *Shigella* completely lacks the SP and fails to assemble the T3SA external needle (Fig. 3.1 in Chapter 3). In this investigation, *Shigella* MxiK-T4L insertion mutants were used to identify important loops within MxiK that are needed to generate a functional SP. Since the T4L insertion at residue 136 completely disrupts both hemolytic activity and IpaB secretion (Fig. 3.5 and Fig. 3.6 in Chapter 3), this region is probably important for SP functions. In fact, the

T3SA from MxiK-T4L-136 *Shigella* mutant strain does not assemble the SP or needle, which is identical in architecture to the T3SA from *mxiK* null strain (Fig. 3.1 in Chapter 3 and Fig. 4.4B and D). Based on the CD spectrum of MxiK-T4L-136, we confirmed that this fusion protein still retains its α-helical secondary structure. More importantly, the CD spectrum of MxiK-T4L-136 is almost identical to that of MxiK-T4L-C, which is still active in restoring *S. flexneri* T3SS activities (Fig. 4.8A). Moreover, the thermal stability of MxiK-T4L-136 is similar to that of MxiK-T4L-C (Fig. 4.8C). Therefore, the insertion at 136 residue in MxiK does not appear to cause structural compromise, but it results in a defect in SP assembly and function. Next, the results of BACTH experiments revealed that MxiK-T4L-136 is no longer able to interact with Spa33 (Fig. 4.9). In contrast, this fusion protein gave a positive result for interacting with $MxiG^{Cyt}$ (Fig. 4.9). Based on data presented in this chapter, we propose that the loop containing residue 136 MxiK is involved in the $Spa33^{WT}$ interaction and this is required to generate a functional SP within the T3SA.

Even though it appears that the T4L insertion at residue 136 residue in MxiK is folded properly, we cannot differentiate between a steric effect and disruption of a key residue involved in the MxiK-Spa33 interaction. Therefore, we generated smaller substitution mutations within this region of MxiK, starting with replacement of residues 134-138 with Ala residues ($MxiK^{134\text{-}138\ Ala}$). This mutant had no hemolytic or IpaB secretion activities, which is same as MxiK-T4L-136 (Fig. 3.5, and Fig. 3.6 in Chapter 3, and Fig. 4.10). To determine which of these residues are important for MxiK activity, we introduced single Ala substitutions and found that one residue, Leu135, was critical for MxiK activity within the SP (Fig. 4.10). These results are probably not a result of structural disruption because *S. flexneri* with single Ala mutations at neighboring residues (even Ala in place of Leu136) restoring both hemolytic and IpaB secretion activities. Moreover,

introducing the same mutation in MxiK-T4L-C (MxiK^{Leu135Ala} -T4L-C) resulted in a CD spectrum and Tm value similar to MxiK-T4L-C (Fig. 4.13).

To better understand how the MxiK$^{134\text{-}138\ Ala}$ and MxiK^{Leu135Ala} mutations negatively affect T3SA activities, BACTH experiments were performed. Both mutants did not show an interaction with Spa33^{WT} which is the same result as seen for MxiK-T4L-136 (Fig. 4.9 and 4.11). Hence, all the data suggest that MxiK residue 135 is involved in the Spa33^{WT} interaction and this is needed to form the SP pod structures. These pods are, in turn, essential for generating a functional T3SA. As mentioned in Chapter 3, cryo-ET images suggest that least two regions of MxiK may be involved in the Spa33 interaction. Thus, it is possible that residues in MxiK other than Leu135 are involved in binding to Spa33^{WT}.

In addition to investigating the importance of Leu135 residue in MxiK, we tested 51 to 55 residues region because of preliminary data of BLI and FP (data not shown). We first introduced five continuous Ala substitutional mutation within residues 51-55 (MxiK$^{51\text{-}55\ Ala}$) to know how this region contributes T3SS activities. This mutation showed no hemolytic and IpaB secretion activities (Fig. 4.12). To analyze secondary structures and Tm for this mutant, we purified MxiK$^{51\text{-}55\ Ala}$-T4L-C to obtain its CD-spectrum that is almost identical to MxiK-T4L-C (Fig. 4.13). These data suggests that the disruption of T3SS activities by this mutant is not resulted from a protein misfold. To determine important residues in this loop region, we introduce single Ala substitutional mutation between 51 and 56, and found that one residue, Leu53, is critical for MxiK function in the SP. Because other Ala substitutional mutation within neighbor residues showed almost same T3SS activities as wild-type MxiK complement strain (Fig. 4.12), T3SS activities of MxiK^{Leu53Ala} are probably not resulted from the structural disruption. In addition, CD-spectrum of MxiK$^{51\text{-}55\ Ala}$ which include Leu53Ala was almost identical to MxiK-T4L-C (Fig. 4.13).

BACTH experiments were performed to analyze interaction ability of $MxiK^{Leu53Ala}$ with $MxiG^{Cyt}$ and $Spa33^{WT}$. Surprisingly, $MxiK^{Leu53Ala}$ is no longer able to interact with both binding partners, $MxiG^{Cyt}$ and $Spa33^{WT}$ (Fig. 4.14). Moreover, a positive control in this experiment, $MxiK^{Asp56Ala}$ also did not show interaction with $MxiG^{Cyt}$ although this mutation in *S. flexneri* strain restored T3SS activities (Fig. 4.14). Since MxiK structure is not available, now, it is difficult to conclude whether Leu53 is involved in $MxiG^{Cyt}$ interaction. Perhaps, the substitutional mutation in this region leads a very small conformational change that is not able to monitor by CD-spectrometry. This small change reduces strength of MxiK interactions which are difficult to detect by BACTH experiment.

In developing new antibiotics and anti-infective therapeutics, it will be important to identify virulence factor targets that can be disrupted to prevent infection. Because disruption of the T3SA via its SP would render this pathogen avirulent, it provides and attractive target for developing such agents. Without the T3SS, *Shigella* species are not able to enter intestinal epithelial cells. Thus, our identification of Leu135 and Leu53 as key residues in the function of MxiK suggest the both regions of MxiK are probably good candidates for identifying small compounds that could serve as anti-infective agents. Moreover, conservation of the residues (Leu135 and Leu53 of MxiK) among homologous proteins, all in the SctK family, suggest that these could be targets for developing new therapeutics that could also target other Gram negative bacteria such as *Pseudomonas aeruginosa* and *Salmonella enterica*, which have related T3SS architecture.

Chapter 5 Cryo-Electron Tomographic Analysis of the *Shigella* T3SA Sorting Platform and Characterization of Component Proteins.

5.1 Introduction

We have worked closely with Dr. Jun Liu (Yale University) to study the architecture of the *Shigella* T3SA using cryo-electron tomography (cryo-ET). Cryo-ET technologies have revealed that the cytoplasmic sorting platform (SP) of the *Shigella* type III secretion system (T3SS) is composed of multiple components that differ from, but are still organizationally related to, parts of the Gram-negative flagellar apparatus (45,57). MxiN is an SP component in the *Shigella* T3SA that forms radial spoke-like structure at the bottom of the SP to connect the six major pod structures to the central hub protein, Spa47, which is a hexameric ATPase that is related to the β-subunit of the F_1 ATP synthase (Fig. 5.1A) (45,48,92). It is also related to the FliI ATPase of the *Salmonella* flagellar apparatus (48,93). As with MxiK and Spa33, MxiN is an essential component of a functional SP. However, while the T3SA SP from a *mxiN* null *S. flexneri* mutant does not possess the central hub and lacks the external needle, it is still able to form remnants of the pod structures that we now know are comprised of a Spa33 complex and MxiK (Fig. 5.1B to E) (45). This phenotype suggests that MxiN is not responsible for maintenance of the pods within the SP, but it is required to maintain Spa47 as the central hub and to connect it with the pods for a functional SP. Therefore, the primary function of MxiN may be the localization of Spa47 and to act as an adaptor for the energy source provided by the central hub as it influences the positioning of the pods within the SP (45).

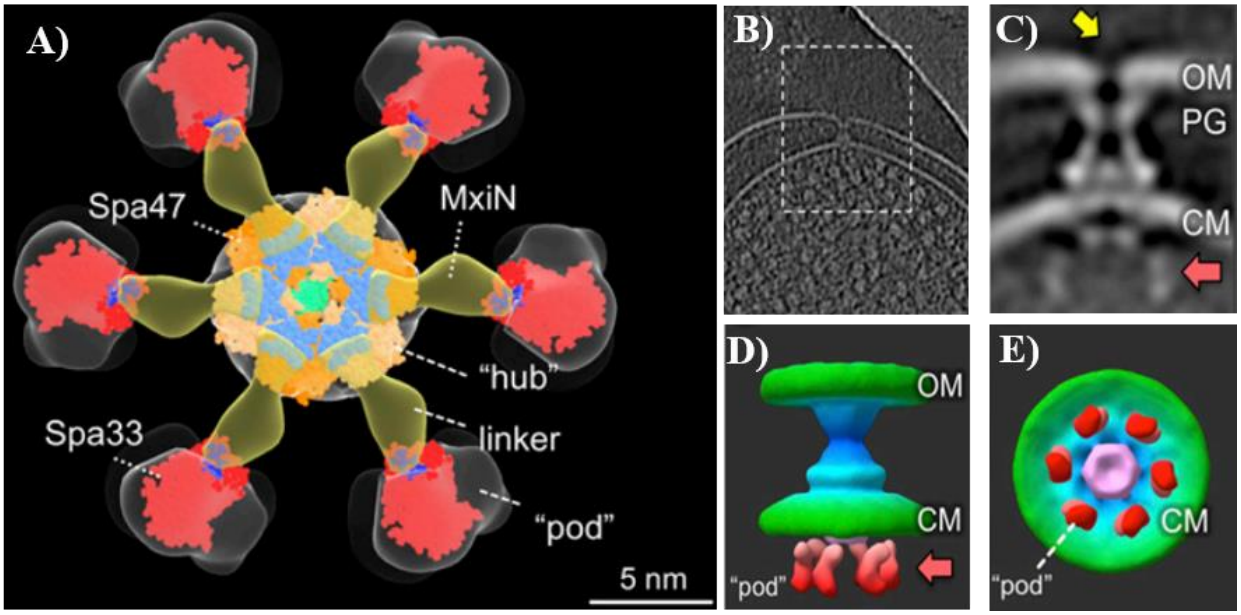

Figure 5.1. Bottom view of the cytoplasmic sorting platform (SP) for the wild-type *Shigella* T3SA and for a *mxiN* null mutant of *S. flexneri*.

A) The bottom view of the SP is shown as a surface rendering. Spa33 (red) represents the pod structure that connects with Spa47 (orange with light blue) via MxiN (yellow). The green structure at center of Spa47 is Spa13 which is a stalk that connects it to the export gate protein MxiA. B) A mini-cell from the *mxiN* null *S. flexneri* strain was harvested and observed by cryo-ET. The mini-cell possesses the T3SA (within the square). The T3SA was magnified to observe the architecture of the SP. C) The basal body spans the outer membrane (OM), peptidoglycan (PG) layer, and cytoplasmic membrane (CM). The pod structures are also observed (red arrow), but the central hub and needle (yellow arrow) are not observed. D) The surface rendering image of the image in C. The pod structures are indicated with red color. E) The bottom view of the image D).

(These images are from B. Hu et al., [2015] PNAS 112:1047-52)

The interaction between MxiN and Spa47 has already been described (53). A MxiN homodimer binds to Spa47 and this interaction alters the ATP hydrolysis activity of the Spa47 (53). This suggests that MxiN functions within the SP is a (probably negative) regulator of Spa47 ATPase activities (53,94,95). Based on current cryo-ET images, MxiN also associates with Spa33 to connect the pod complex with the central hub, however, only a few *in vitro* data have been reported for this interaction (96). Here, we provide clear evidence for the interaction between MxiN and $Spa33^{WT}$ and shown that we can purify this complex. I and other members of our group have also observed this interaction based on BACTH analyses (data not shown). To demonstrate this interaction, size exclusion chromatography (SEC) was performed to detect a complex of MxiN and $Spa33^{WT}$. This chromatographic method is able to separate proteins based on the molecular size. After monitoring the elution profile based on absorbance at 280 nm (A_{280}), the proteins in the collected fractions were analyzed using SDS-PAGE. In parallel, Biolayer interferometry (BLI) was performed to look for a physical interaction between the purified proteins. In this assay, protein-protein interactions are detected by changes in the white light interference patterns at the BLI sensor tip, much like the signals detected by surface plasmon resonance (SPR) spectroscopy (97). Since BLI is done using a 96 well microplate format, varied concentration of analytes can be tested in a single assay, which allows for the generation of a binding curve to determine the dissociation constant (Kd) of the interaction. Together, these two *in vitro* experiments were performed to confirm the interaction between MxiN and Spa33 and to determine the strength of this interaction.

For the *Shigella* T3SA SP, high resolution protein structures would be ideal for understanding their functions and interactions. Even though cryo-ET techniques are available to visualize the overall architecture, these methods do not give a high-resolution snapshot of the

structure. Currently, only the structure of the C-terminal portion of a MxiN homologue from the flagellar apparatus of *Salmonella enterica*, FliH, has been determined, while MxiN and its homologous virulence T3SA structures remain unknown (93). In this investigation, we used three biophysical experiments in an attempt to obtain structural and biophysical information on MxiN. First, CD spectroscopy was performed to characterize the MxiN secondary structure. Then, NMR spectroscopy and crystallization screens were performed in an attempt to determine its high resolution structure. Unfortunately, NMR was not a suitable technique for determining the MxiN structure because not enough peaks could be resolved within its NMR spectrum (see below). Meanwhile, MxiN, as well as MxiN-T4L fusion proteins have been put into crystal screens for subsequent X-ray crystallographic analysis. Nevertheless, while we have made efforts to determine the high resolution structure of MxiN structure, these have not yet yielded useful information. Therefore, at end of this chapter, I will report on the current status of those experiments and the problems that need to be overcome for determination of the MxiN structure.

5.2 Results

Size exclusion chromatography (SEC) of the MxiN-Spa33 complex.

Initially, we attempted to purify a MxiN-Spa33^{WT} complex after they were co-expressed in *E. coli*, however, the purified complex was contaminated by a number of other proteins (not shown). Thus, a mixture of purified MxiN and purified Spa33^{WT} was incubated at 4 °C for overnight. The mixture was loaded onto an SEC column and the eluting proteins were monitored by absorbance at 280 nm. In the chromatogram shown in Figure 5.2, two peaks of absorbance were observed during the separation of the protein sample. Proteins in each of the two peaks were analyzed using SDS-PAGE. In the fractions from the first peak, three dominant bands were observed in the SDS-PAGE gel. The largest band is observed near the 35 kDa band of a molecular weight standard, and the smallest band is between the 11 and 17 kDa bands of the ladder. Since Spa33^{FL} and Spa33^{Cterm} fit these protein sizes, Spa33^{WT} was clearly part of the first peak. In addition to these two protein bands in the gel, another band is observed around 25 kDa, which corresponds to the MxiN molecular weight of 26 kDa. Although fractions at the start of the second peak in the chromatogram had two protein bands at 25 kDa and 11 kDa, the main protein in the second peak is only the 25 kDa protein, which corresponds to MxiN based on molecular mass (Fig. 5.2). So this complex could be purified for further study.

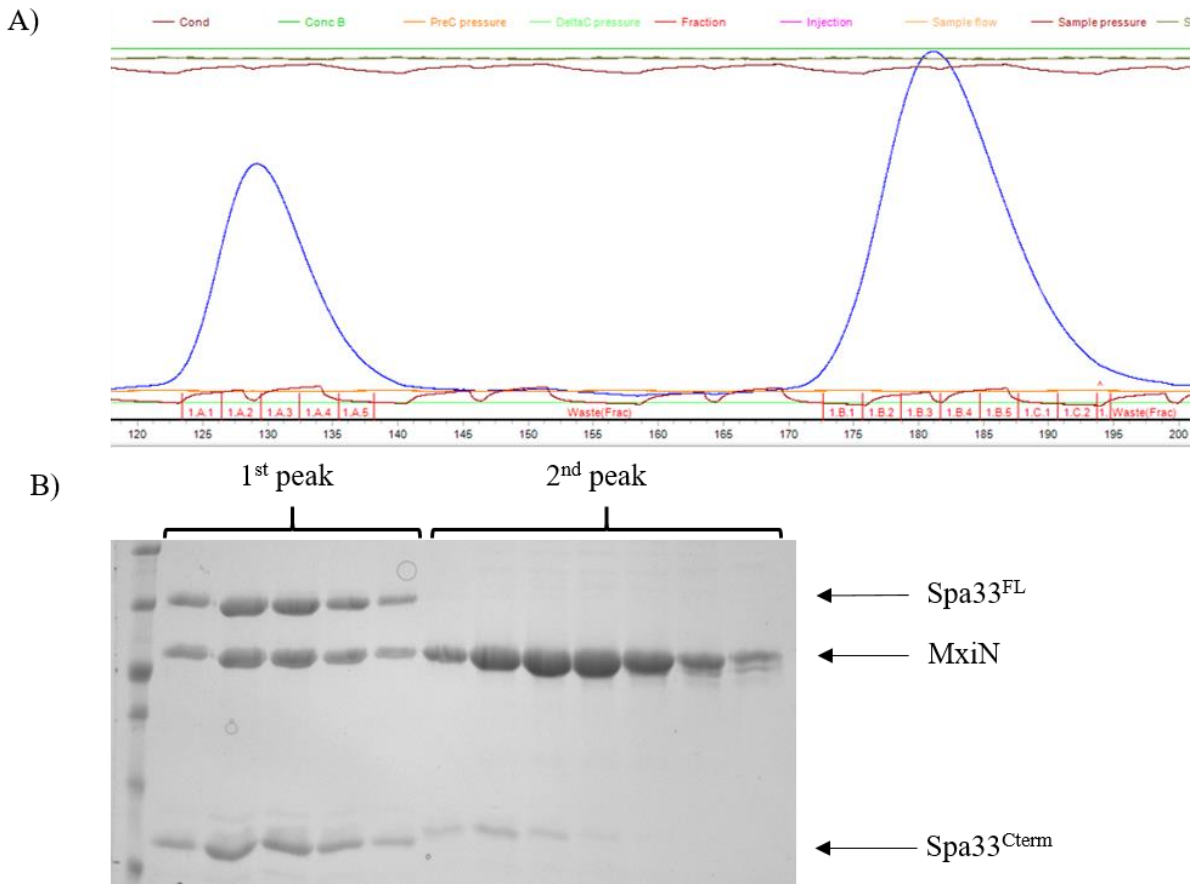

Figure 5.2. Chromatogram for size exclusion chromatography for MxiN and Spa33^{WT} mixture.

The protein mixture of purified MxiN and purified Spa33^{WT} was loaded into a SEC column. A) Two peaks of 280 nm absorbance (A_{280}) were detected in the chromatogram from AKTA system. B) Proteins in fractions from the first peak and second peak were analyzed using SDS-PAGE. Most of MxiN and Spa33 complex are in the first peak and MxiN is dominantly in the second peak.

Biolayer Interferometry (BLI) for MxiN and Spa33^{WT} interaction.

To determine the strength of the MxiN-Spa33 interaction, we used Biolayer interferometry (BLI) using an Octet system (ForteBio). MxiN with a HisTag was bound to the BLI tip, and different concentrations of Spa33^{WT} without the tag (400, 200, 100, 50, 25, and 12.5 µg/mL) were used to analyze their interaction (Fig. 5.3). Based on the association and dissociation rates for each reaction, BLI program is able to calculate a dissociation constant (Kd) value which turned out to be 0.55±0.091 µM. Nonspecific binding of Spa33^{WT} to the BLI tip was not observed during this experiment.

Circular dichroism (CD) spectroscopy of MxiN.

As a low-resolution structural analysis, we used far-UV circular dichroism (CD) spectropolarimetry. The CD spectrum for MxiN was measured between 190 to 260 nm. The CD spectrum was obtained and the signal converted to molar ellipticity. A positive peak was observed around 197 nm, and two negative peaks were observed around 208 and 222 nm (Fig. 5.4A). These were hallmarks that indicated MxiN is rich in α-helical secondary structure (91). The molar ellipticity at 222 nm was also monitored as a function of increasing sample temperature (from 10 to 90 °C). This allowed us to monitor the loss of α-helical structure and thereby provided a measure of thermal stability. The resulting unfolding profile showed clear sigmoidal curve and the midpoint of its unfolding transition (Tm) was 40.29 °C (Fig. 5.4B).

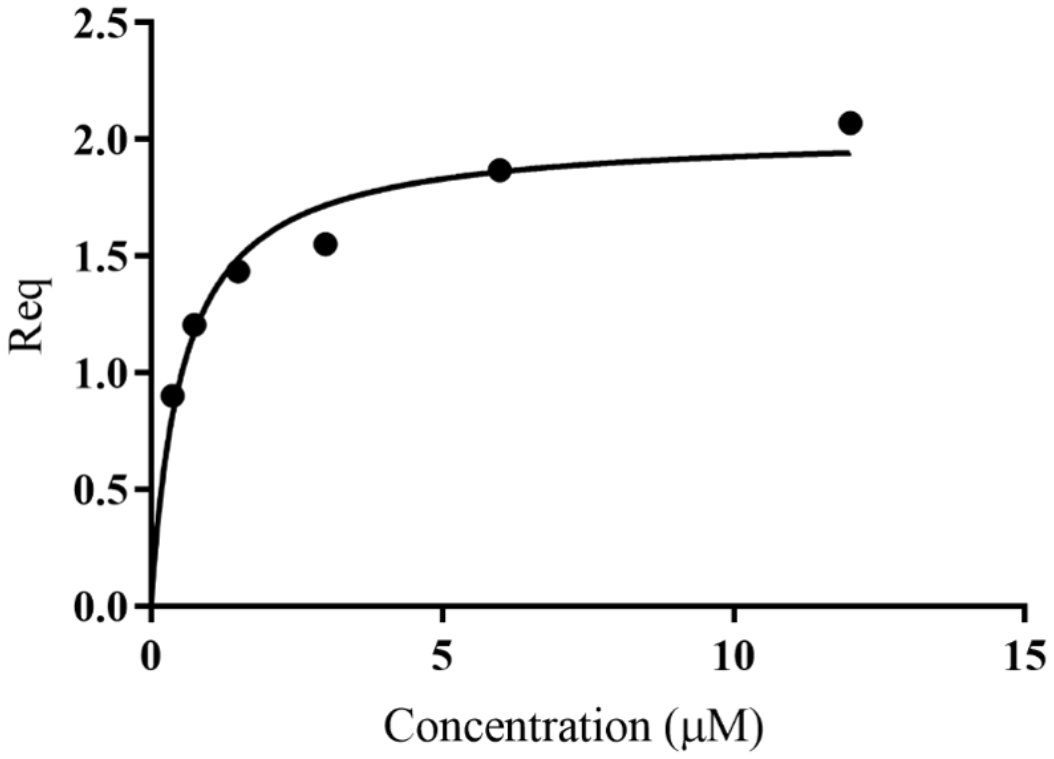

Figure 5.3. The MxiN-Spa33^{WT} interaction was also monitored using BLI.

MxiN with a HisTag was loaded on to a BLI tip. The tips were immersed in various concentrations of Spa33^{WT} without the tag to determine association and dissociation rates with MxiN on the BLI tips. Both rates were used to calculate Kd value which is 0.55±0.091 μM. This graph was created by GraphPad Prism.

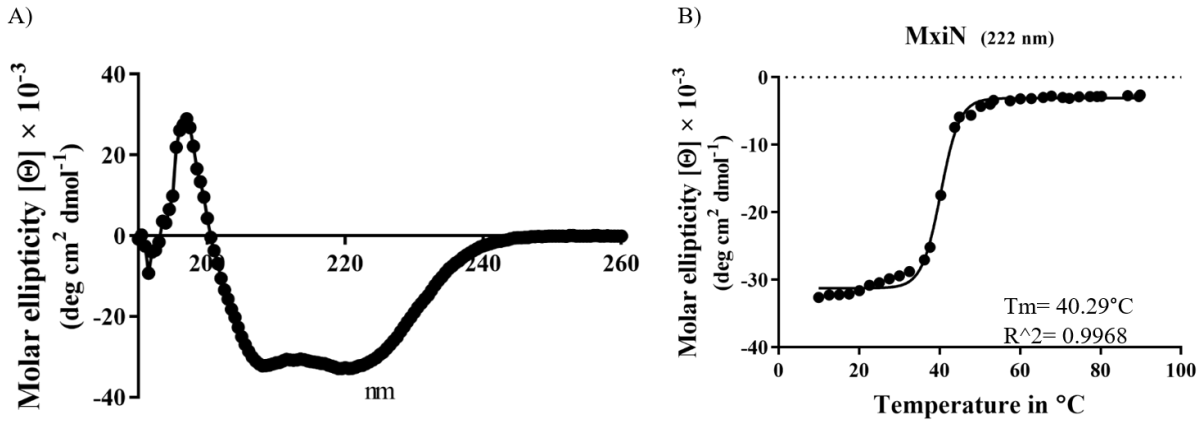

Figure 5.4. CD spectral analysis of MxiN.

A) The far UV spectrum (190 to 260 nm) was used to determine molar ellipticity spectrum of MxiN in 0.1 cm cuvettes. This spectrum was determined as an average of triplicate measurements. A positive peak around 197 nm and two negative peaks around 208 and 222 nm were observed, suggesting a large α-helical component. B) The molar ellipticity at 222 nm was monitored with increasing temperature (between 10 and 90 °C) and the unfolding temperature (Tm) was found to be 40.29 °C.

Nuclear Magnetic Resonance (NMR) spectroscopy.

MxiN was labeled uniformly with ^{15}N and the concentration adjusted to 180 µM for HSQC NMR spectroscopy. A spectrum was then obtained using a 600 MHz magnetic field (Fig. 5.5). MxiN has 231 residues in its structure, however, only 20 peaks were detected by NMR. This could be due to the large size of MxiN in solution since we know that it forms a tight dimer. Because of this, we elected to attempt methods other than NMR spectroscopy for more detailed structure analysis of MxiN.

Crystal screens of MxiN.

MxiN was screened for crystal formation using various crystallization solutions that are part of different screening kits. These were mixed and set up for crystal screening in 96 well plates which were then incubated at 20 °C. Unfortunately, MxiN in the crystallization solutions failed to form crystals and in some cases demonstrated precipitation. Nevertheless, these experiments are continuing because of the high solubility of MxiN. One of the samples showing precipitation is shown in Figure 5.6 under both visible and UV lights. Since MxiN has relatively high stability at high salt concentrations, this protein generally gave rise to clear solutions when used in the Salt-Rx crystallization kit (not shown). We are also attempting to purify the MxiN-Spa33 complex shown in Figure 5.2 using similar screening strategies. All of the crystallography work is being done in collaboration with Dr. Scott Lovell (Protein Structure Laboratory, University of Kansas).

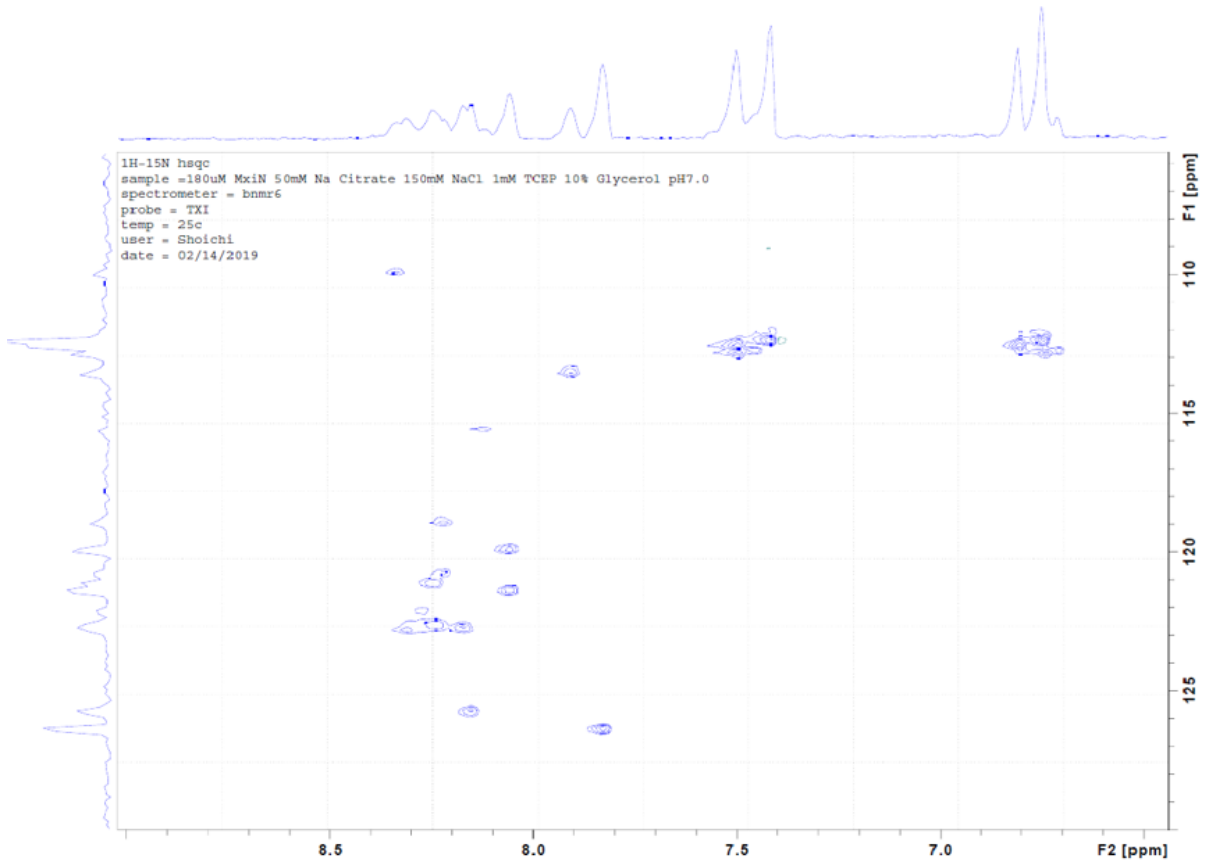

Figure 5.5. The HSQC spectrum for MxiN.

MxiN was expressed in M9 minimum with ^{15}N ammonium chloride. 180 μM of MxiN with ^{15}N labeled was used for NMR experiment to detect peaks under 25 °C. Although MxiN is a 231 residue protein, less than 20 peaks were detected making the results to analyze for MxiN structural information.

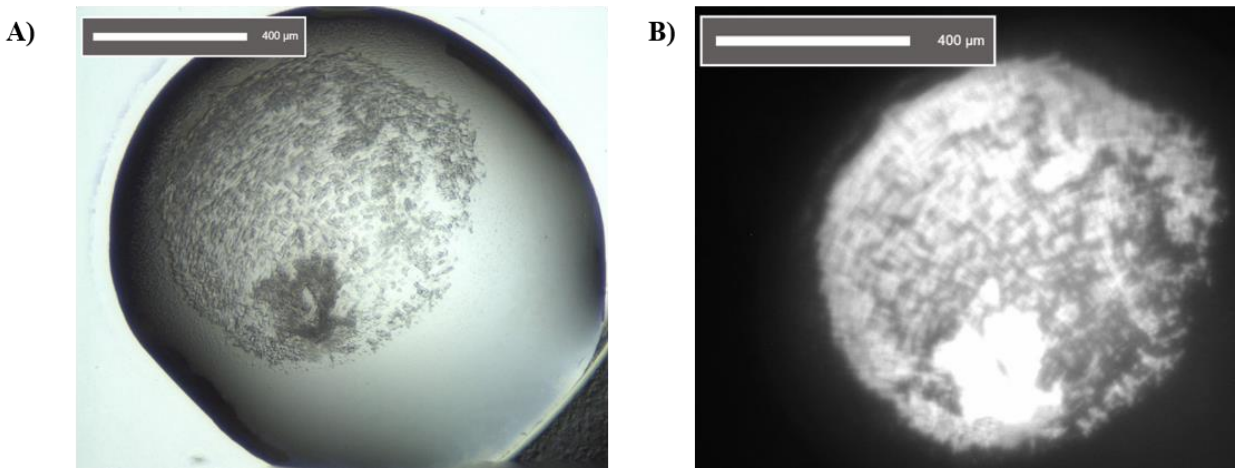

Figure 5.6. Example picture of crystal screening for MxiN.

MxiN and crystallization solution mixtures were set up in 96 wells plates using the sitting drop method. All conditions failed to form protein crystals. A) Example of picture of a well which shows MxiN precipitation under visible light (100 mM Sodium potassium phosphate buffer, pH 6.2 with 10 % PEG 3000). MxiN tends to be aggregate in most of solutions. B) Same well picture as (A), but image was photographed under UV light. Aggregated MxiN part are shown in white regions.

5.3 Conclusion

MxiN is one of the essential components of the SP of the *Shigella* T3SA. Recent cryo-ET analyses suggest that MxiN interacts with both Spa47 and Spa33 (45). In this chapter, the interaction between MxiN and $Spa33^{WT}$ was examined using complementary *in vitro* experiments, SEC and BLI. In the chromatogram from the SEC analysis, two A_{280} absorbance peaks were observed, so SDS-PAGE was used to determine the proteins present in these two peaks. Based on the SDS-PAGE gel, a MxiN-$Spa33^{WT}$ complex (MxiN with $Spa33^{FL}$ and $Spa33^{Cterm}$) was present in the first peak while MxiN and perhaps a small amount of $Spa33^{Cterm}$ and/or another minor contaminant were observed in the second peak. These data suggests that MxiN interacts with $Spa33^{WT}$ in the protein mixture with and this protein complex eluting in the first peak due to its large size relative to MxiN alone. The fact that no separate $Spa33^{WT}$ ($Spa33^{FL}$ and $Spa33^{Cterm}$) was observed suggests that the interaction is fairly strong and that the excess MxiN, which was not able to bind to $Spa33^{WT}$, eluted later as would be expected. The large size of the complex also suggests that the $Spa33^{WT}$ complex (comprised of one $Spa33^{FL}$ and two $Spa33^{Cterm}$) formed a complex larger than what could be formed by the Spa33 along or the MxiN homodimer which approximately 52 kDa in size. In addition to the SEC experiment, BLI was performed to determine the Kd value for this interaction. Since MxiN itself shows high affinity with metal ions as nickel and cobalt, MxiN with a HisTag was used to attach it to the BLI tip via a nickel-charged tris-nitrilotriacetic (NTA) biosensor. Different concentrations of $Spa33^{WT}$ without a HisTag interacted with MxiN on the BLI tips. The association and dissociation rates were determined for each concentration of the analyte ($Spa33^{WT}$) for this interaction. Based on the obtained data, the Kd value was determined which is 0.55 ± 0.091 μM, which is a reasonably strong interaction. An empty

BLI tip (without MxiN loading) was then used to show that Spa33^{WT} showed very little to no nonspecific association during the BLI experiment. Thus, this Kd value is the resulted of a specific MxiN-Spa33^{WT} interaction. Based on the results of these two *in vitro* experiments, we confirmed that MxiN interacts with Spa33^{WT} with a dissociation constant near 0.5 μM. It is thus possible that MxiN needs to interact tightly with Spa33 to serve as an adaptor protein between the pod structure and the central hub during the assembly of the intact SP. Together with data from the BACTH experiment for this interaction (data not shown), these findings demonstrate a clear interaction between MxiN and Spa33^{WT} as suggested in its *in situ* (cryo-ET) structure (Fig. 4.1 in Chapter 4).

Currently, one of the MxiN functions that has been reported is that it is a regulator of Spa47 ATPase activity which is needed to drive the protein translocation steps of the T3SS (53). Despite MxiN's importance for SP functions, structural details of this protein are still unknown. The CD-spectrum from MxiN suggests that it is α-helical with two minima around 208 and 222 nm and the maximum around 197 nm. This result is agreement with a secondary structure predictions for MxiN using the PSIPRED program. Even though the structure of FliI and the C-terminal fragment of FliH (FliH^{C}) from the *Salmonella* flagellar system have been determined (PDB ID: 5B0O) (93), no MxiN structure has been reported. This is why NMR and X-ray crystallography were used in an attempt to determine the MxiN high resolution structure. The results of NMR spectroscopy for MxiN gave only almost 20 peaks in its spectrum, which is far shy of what is needed to analyze the MxiN structure. In general, large molecules are not suitable for NMR experiment, therefore, the large size of the MxiN homodimer in the NMR buffer could be leading to aggregation which would result in the small number of peaks seen in the NMR spectrum. MxiN has also been set up crystal screening for possible X-ray diffraction studies. In addition to setting up wild-type MxiN, a truncated version of MxiN and MxiN fusion proteins (MxiN with MBP and T4L) have been set

up for screening, however, all samples have thus are either precipitated or remained in solution in the screening plates. Since MxiN is sensitive to low salt conditions, the precipitation in the screening solutions may be due to changing salt conditions as the mixtures are prepared. Possibly for the same the reason, MxiN at low salt could have led to aggregation that caused the NMR experiment to fail. In the future, MxiN may need to be co-crystallized as a C-terminal fragment with Spa47, which is what was done in previous structure reports for FliI and $FliH^{C}$ of the bacterial flagellar complex (93). Nevertheless, crystallization screens will continue for MxiN and these will be expanded by screening for crystals of the purified MxiN-Spa33 complex. Currently, cryo-electron microscopy techniques have been improved with regard to the resolution of images, and these techniques might also prove useful in obtaining high resolution structures for proteins such as MxiN or MxiN and the Spa33 complex.

Chapter 6 Discussion

Shigella flexneri is a Gram-negative bacterium that uses its type III secretion system (T3SS) to inject effector proteins into eukaryotic cells to alter normal host cell functions for its own purposes. The type III secretion apparatus (T3SA) has a syringe-like architecture that possesses a cytoplasmic sorting platform (SP) which acts as the plunger, a basal body that is the syringe body, and a needle with associated tip complex (45,98). Although *Shigella's* primary virulence factor is its T3SS which has been studied for decades, the location of important SP components and their precise functions are still not clearly understood. In fact, it has only been five years since the first observation of the structure of the *Shigella*, or any, T3SA SP. In 2015, Hu and coworkers first visualized the SP and were able to propose the positions of some SP components using high resolution protein images obtained using cryo-electron tomography (cryo-ET) (45). Even then, however, parts of the six pod-like structures that make up the bulk of the SP remained unidentified due, in part, to the lack of information (structural and biochemical) on the proteins that resided here (Fig. 1.3B in Chapter 1). Since MxiK could be co-immunoprecipitated with other SP components based on previous reports (84,96), the Picking laboratory hypothesized that part of the unknown density region within the pod-like structures is made up of MxiK.

To determine the MxiK position within the SP, a library of MxiK-T4L fusion/insertion mutants were generated and one selected to be expressed in a *mxiK* null *Shigella* strain so that the protein could be observed with the added electron density from the T4L seen within the SP using cryo-ET. Based on the observed T4L position, we pinpointed the positon of MxiK within the SP (Fig. 3.7B and C in Chapter 3) (57). Therefore, the positions of all the SP components, including MxiK, have now been revealed (Fig. 4.1 in Chapter 4). Interestingly, MxiK is located just beneath

the cytoplasmic portion of the inner membrane ring protein MxiG via interactions with the MxiG cytoplasmic domain ($MxiG^{Cyt}$). In the SP, MxiK appears to also associate with the Spa33 hetero-oligomeric complex to give rise to the complete pod-like structure (Fig. 3.7C in Chapter 3 and Fig. 4.1 in Chapter 4). These pods have six-fold discontinuous symmetry and make up the bulk of the SP. The central hub within the SP "cage" is formed by Spa47, which is connected with Spa33 of the pods via radial spokes comprised of a dimer of MxiN (45,53). Then, Spa47 connects with the export gate protein MxiA at the base of the basal body via the Spa13 stalk protein (45). In addition to these *in situ* data, BACTH analyses were performed to confirm MxiK's binding partners, which indeed are $MxiG^{Cyt}$ and $Spa33^{WT}$ (Fig. 3.8 in Chapter 3). More specifically, MxiK showed an interaction with $Spa33^{FL}$ within the Spa33 complex rather than one of the two copies of the Spa33 C-terminal domain ($Spa33^{Cterm}$). Therefore, I propose that MxiK interacts with both $MxiG^{Cyt}$ in the inner membrane ring and $Spa33^{FL}$ part of the hetero-oligomer to form the pod-like structure with MxiK serving as an adaptor between the pods and the basal body.

As mentioned above, the SP associates with $MxiG^{Cyt}$ of the inner membrane ring and MxiK acts as the adaptor between these two substructures. Interestingly, $MxiG^{Cyt}$ forms a continuous 24-fold symmetrical ring while MxiK (as part of the pod-like structures) has a discontinuous six-fold symmetry (57). To better understand the interaction giving rise to this symmetry transition, Ala substitutional mutations were introduced into several loop regions in $MxiG^{Cyt}$. Only the double loop mutant $MxiG^{61\text{-}66/81\text{-}85Ala}$ disrupted T3SS activities, which resulted in a loss of SP and needle assembly (Fig. 4.3 and 4.4C in Chapter 4). Moreover, this mutant was no longer able to interact with MxiK (Fig. 4.5 in Chapter 4). These data suggest that these two loop regions may contribute to the MxiK interaction.

In addition to the MxiG^{Cyt} loop regions involved in its association with MxiK, we have hypothesized that the MxiG linker that connects MxiG^{Cyt} with the MxiG transmembrane helix provides flexibility for the MxiG cytoplasmic domain and needed movement for the molecular dynamics required for SP activities. Different types of mutations (insertions, truncations and substitutions) in the linker region revealed that flexibility here may be essential for T3SS activities, however, the linker could accept a number of major changes without eliminating SP functions. In the end, MxiG^{Cyt} with the shortest linker showed almost no T3SS activity (Fig. 4.6 in Chapter 4). To observe a T3SA possessing MxiG^{Cyt} with the shortest linker region, we have been shipped *Shigella* expressing MxiG$^{d108-124}$ to Yale University for cryo-ET analysis. It is our hypothesis that this mutant will completely lack the SP, however, it is possible that the SP is there but the inability for MxiG^{Cyt} to move prevents the structure changes needed for active secretion (work in progress). If this shortest linker does allow for SP assembly, the absence of secretion would suggest that it is not able to allow for formation of the extracellular needle. If this is the case, perhaps the export gate and the inner and outer membrane rings of the basal body are in closed conformations as is seen for the individual SP null mutants. Because of our hypothesis that movement of MxiG^{Cyt} could contribute to the rotational of the pod-like structure (possibly driven by the Spa47 ATPase), we constructed a linker MxiG-T4L insertion mutant to provide potential steric hindrance of this domain's movement. Surprisingly, this T4L insertion mutant still showed almost 50 % of wild-type T3SS activity (data not shown). Now these will take advantage of this mutant identity the linker's location using cryo-ET imaging (work in progress).

To better characterize MxiK within the SP, the T3SA *in situ* structure for the MxiK-T4L-136 mutant was observed using cryo-ET. Because its T3SA SP is almost identical to that of the *mxiK* null mutant (Fig. 4.4B and C in Chapter 4), we purified this fusion as a recombinant protein

to monitor its secondary structure. We also explored its ability to interact with $MxiG^{Cyt}$ and $Spa33^{WT}$. Importantly, both MxiK-T4L-136 and $MxiK^{Leu135Ala}$ failed to interact with Spa33 (Fig. 4.9 and 4.11 in Chapter 4). Therefore, we postulate that Leu135 in MxiK is involved in the interaction with Spa33, and this interaction is essential for SP assembly. In addition, we determined that Leu53 in MxiK is an important residue for T3SS activities (Fig. 4.12 in Chapter 4). Since the $MxiK^{Leu53Ala}$ mutant failed to interact with either $MxiG^{Cyt}$ and Spa33, it is difficult to conclude just how this MxiK mutation is affected by this point mutation (Fig. 4.14 in Chapter 4). It does not seem likely that it is a misfolding of the protein, however, this will be tested. Importantlly, Dr. Meenakumari Muthuramalingam in our laboratory determined the high resolution crystal structure for PscK (SctK using the unifying nomenclature and the *P. aeruginosa* homologue of MxiK) (Fig. 6.1A). In this structure, the residues equivalent to Leu53 and Leu135 of MxiK are located on opposite sides of the protein (Fig. 6.1A and B). Therefore, I propose here that the Leu53 residue of MxiK is involved in the $MxiG^{Cyt}$ interaction while Leu135 is involved in the Spa33 interaction. Further characterization of this mutant form of MxiK will be required. Based on all available data on the generated MxiK insertional and substitutional mutations described in Chapter 4, along with the PscK structure, I propose that Leu53 and Leu135 are candidate target residues in MxiK to design or screen for small anti-infective compounds that could disturb SP assembly.

At the bottom of the SP, the central hub (the hexameric Spa47 ATPase) connects with Spa33 via radial spokes formed by the protein MxiN, which is required to localize the Spa47 (45,53). In this investigation, the MxiN interaction with Spa33 was confirmed by SEC and BLI (Fig. 5.2 and 5.3 in Chapter 5). In parallel, I attempted to determine MxiN's high resolution

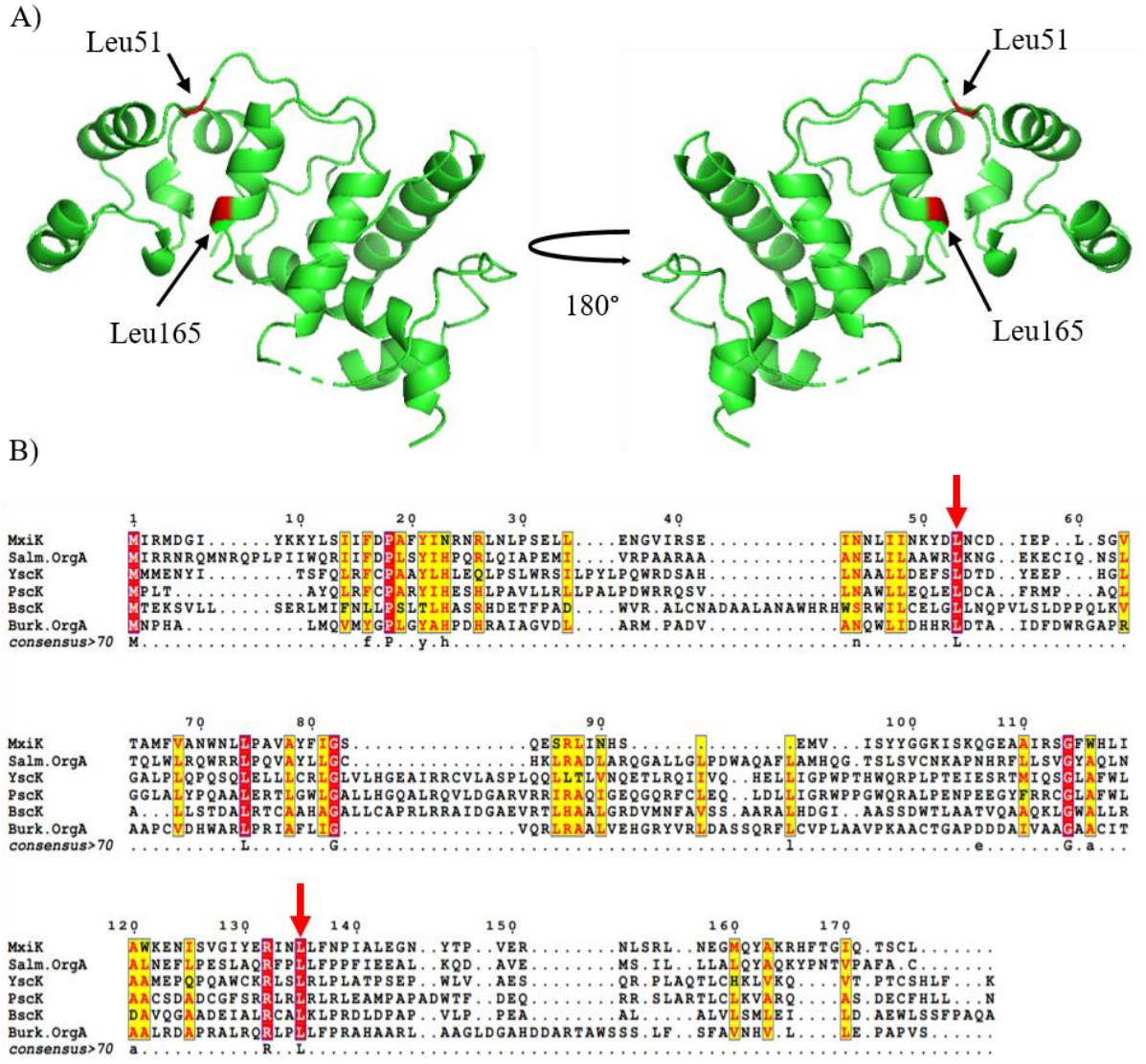

Figure 6.1. Crystal structure of PscK (SctK).

A) Dr. Meenakumari Muthuramalingam determined the crystal structure of PscK. Leu53 and Leu135 in MxiK are conserved with Leu51 and Leu165 in PscK which are shown in red. B) Sequence alignment of different SctK family proteins. MxiK is from *S. flexneri*, Salm.OrgA is from *Salmonella enterica* T3SS-1, YscK is from *Yersinia pestis*, PscK is from *P. aeruginosa*, BscK is from *Bordetella bronchiseptica*, and Burk.OrgA is from *Burkholderia thailandensis.* The Leu51 and Leu165 residues in PscK are conserved among this family, and indicated by the red arrows in this figure.

structure using both NMR and X-ray crystallography, however, neither of the methods have yet provided a successful result. Perhaps, the MxiN homodimer in high concentration causes aggregation, which is not suitable for NMR or protein crystallization. I am currently looking at the buffer components, pH, temperature and salt conditions in hopes of optimizing them for better protein stability and for crystallization screening.

Previously, cryo-ET had been used to visualize T3SAs from *spa33* and *mxiN* null mutants (45). In this investigation, we observed the T3SA from a *mxiK* null mutant and it was identical to that seen when *spa33* is deleted (Fig. 3.1 in Chapter 3). Here, I propose a model for the assembly of the SP based on these cryo-ET images. First, *Shigella* generates the basal body on the two bacterial membranes with components crossing the cytoplasmic membrane via general *sec*-dependent translocation system (Fig. 6.2A) (81,99-102). Once the basal body is essentially formed, I believe that MxiK interacts with Spa33 (via $Spa33^{FL}$ of the Spa33 complex) to form pod-like structures in the bacterial cytoplasm. This is an initial step for the SP assembly based on the fact that no SP is seen for *mxiK* and *spa33* null strains (45). After forming the pod-like structures, MxiK in the complex interacts with $MxiG^{Cyt}$ of the inner membrane ring (Fig. 6.2B), based on the fact that pods are visible for *mxiN* null mutants. MxiN then recognizes the bottom part of the Spa33-containing pod-like structures to allow for localization of the central hub, Spa47 and Spa13 stalk complex, at the middle of the SP, based on the fact that the *mxiN* null strain lacks these structures (Fig. 6.2C) (45). After SP assembly is completed, the needle protein monomers (MxiH) are translocated to the bacterial surface via the MxiA export gate to form the needle part (33,34). The system is now secretion competent. It is at this point that the needle tip components, IpaD, IpaB, and IpaC, are translocated to the tip of the needle where IpaD forms the tip complex, IpaB is

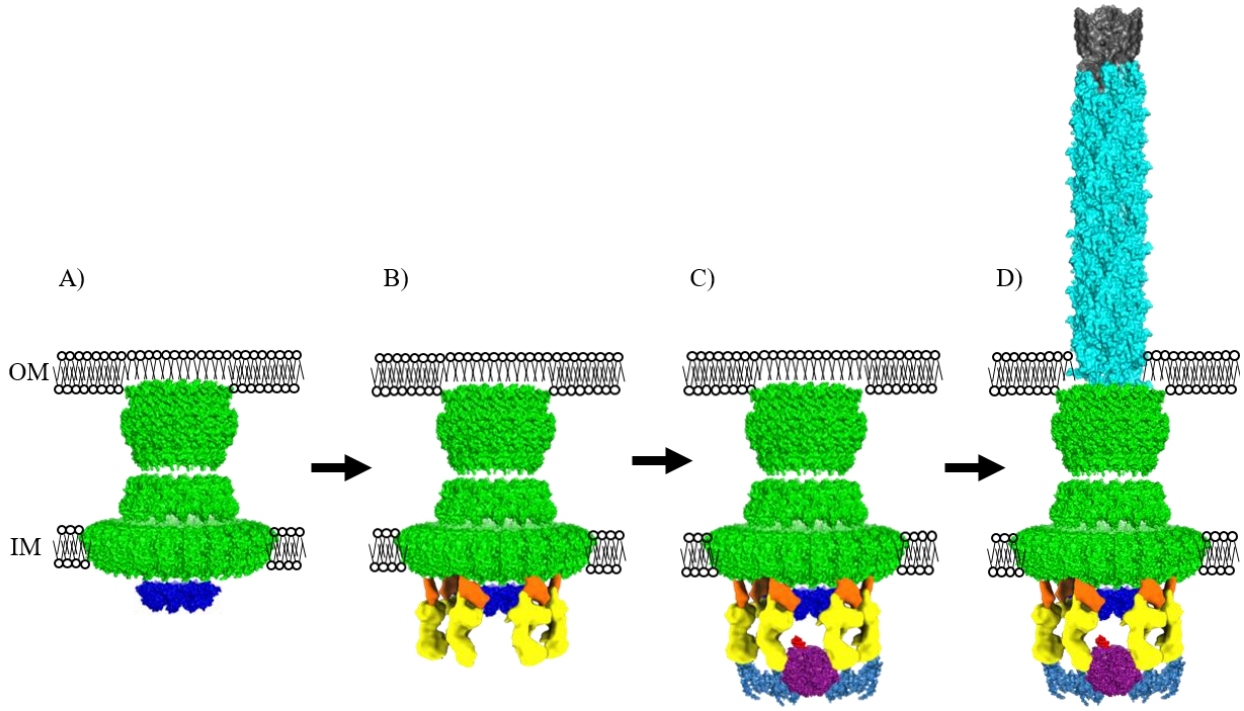

Figure 6.2. Model of T3SA assembly process.

A) *Shigella* develops the basal body part on bacterial inner (IM) and outer (OM) membranes via the general secretory pathway. The green structure is the basal body (here shown for *Salmonella* InvG, PrgH, and PrgK, PDB ID: 5TCR). The export channel is MxiA (PDB ID: 4A5P, blue). B) In the bacterial cytoplasm, MxiK (orange) and the Spa33 complex (yellow) form the pod-like structures, which then associate with the inner membrane ring, $MxiG^{Cyt}$. C) MxiN (homologue of flagella FliH, PDB ID: 5B0O, light blue) localizes with Spa47 (purple) and Spa13 stalk (red) to complete SP assembly (here are the homologues from enteropathogenic *E. coli* EscN and EscO, respectively, PDB ID: 6NJP). D) After the SP assembly is complete, the needle protein monomers MxiH are translocated to the bacterial surface to form the needle filament (*Salmonella* PrgI, PDB ID: 6DWB, cyan is shown here). Lastly, IpaD (PDB ID: 2J0O, gray) is translocated on the needle tip to form the tip complex pentarmer.

maintained as part of the “primed” tip complex prior to host cell contact (Fig. 6.2D) (36). IpaB and IpaD provide a second secretion control checkpoint at the needle tip. Once IpaB contacts the host cell membrane, its conformation is changed so that it and IpaC are inserted into the host cell membrane to form the translocon pore (40,41).

Based on my model, developing new anti-infective medicines that target the Leu53 and Leu135 regions in MxiK should be able to interfere the initiation step for SP assembly. Here, I also would like to mention that the bacterial flagellar T3SA is not composed of true SctK family proteins (Table 3.1 in Chapter 3). Therefore, new anti-infective medicines that target SctK are probably going to be specific for the virulence T3SS, even though its overall architecture is roughly shared with the bacterial flagellar T3SA. This fact is important for designing medicines that do not have off target side effects because other Enterobacteriacae are still able to keep their activities for our health.

Determination of the MxiK structure will be important for fully understanding its functions within the SP. In my preliminary data, MxiK is now available in a soluble form when it is co-expressed with Spa33 in an *E.coli* expression strain. Thus, I have attempted to generate protein crystals of this complex for X-ray crystallographic study. Unfortunately, this complex has resulted in the formation of protein precipitates in almost all of the crystal screen solutions tested so far. Therefore, I am now working on the conditions of the screens to optimize them for obtaining diffractable protein crystals. Another approach to solve the MxiK structure is computational modeling. Although amino acid sequence similarities between MxiK and PscK is only about 9 % (using Unipro UGENE software), it may still be possible to develop a MxiK structural model based on the PscK structure (Fig. 6.1A). In addition to these computational experiments, the purified MxiK-Spa33^{WT} complex might be able to be used for site-direct spin labeling electron

paramagnetic reasonance (SDSL-EPR) to measure distances between residues within the protein. This distance information might be useful to complement and confirm any MxiK structural model that is developed. Once we determine the MxiK structure, we will be able to fit the structure into our cryo-ET images to predict its orientation and localize Leu53 and Leu135 in MxiK, which would help in developing new anti-infective medicines.

Bibliography

1. Keusch, G. T. (1998) The rediscovery of Shiga toxin and its role in clinical disease. *Jpn J Med Sci Biol* **51 Suppl**, S5-22
2. Trofa, A. F., Ueno-Olsen, H., Oiwa, R., and Yoshikawa, M. (1999) Dr. Kiyoshi Shiga: discoverer of the dysentery bacillus. *Clin Infect Dis* **29**, 1303-1306
3. Marteyn, B., Gazi, A., and Sansonetti, P. (2012) Shigella: a model of virulence regulation in vivo. *Gut Microbes* **3**, 104-120
4. CDC. (n.d.) Shigellosis Chapter 4 Travel-Related Infectious Diseases https://wwwnc.cdc.gov/travel/yellowbook/2020/travel-related-infectious-diseases/shigellosis Accessed: 13 April 2020.
5. CDC. (2014) National Enteric Disease Surveillance: Shigella Annual Report, 2012 [PDF file] https://www.cdc.gov/ncezid/dfwed/pdfs/shigella-annual-report-2012-508c.pdf Accessed: 13 April 2020.
6. CDC. (n.d.) Shigella – Shigellosis https://www.cdc.gov/shigella/audience-medical-professionals.html Accessed: 13 April 2020.
7. NARMS. (n.d.) Antibiotic Resistance Threats in the United States, 2019 [PDF file] https://www.cdc.gov/drugresistance/pdf/threats-report/2019-ar-threats-report-508.pdf Accessed: 13 April 2020.
8. Schroeder, G. N., and Hilbi, H. (2008) Molecular pathogenesis of Shigella spp.: controlling host cell signaling, invasion, and death by type III secretion. *Clin Microbiol Rev* **21**, 134-156
9. Carayol, N., and Tran Van Nhieu, G. (2013) The inside story of Shigella invasion of intestinal epithelial cells. *Cold Spring Harb Perspect Med* **3**, a016717
10. Dupont, H. L., Levine, M. M., Hornick, R. B., and Formal, S. B. (1989) Inoculum size in shigellosis and implications for expected mode of transmission. *The Journal of infectious diseases* **159**, 1126
11. Gorden, J., and Small, P. L. (1993) Acid resistance in enteric bacteria. *Infection and Immunity* **61**, 364-367
12. Niyogi, S. K., Vargas, M., and Vila, J. (2004) Prevalence of the sat, set and sen genes among diverse serotypes of Shigella flexneri strains isolated from patients with acute diarrhoea. *Clin Microbiol Infect* **10**, 574-576
13. Marteyn, B., West, N. P., Browning, D. F., Cole, J. A., Shaw, J. G., Palm, F., Mounier, J., Prévost, M.-C., Sansonetti, P., and Tang, C. M. (2010) Modulation of Shigella virulence in response to available oxygen in vivo. *Nature* **465**, 355-358
14. Sansonetti, P. J., Arondel, J., Cantey, J. R., Prevost, M. C., and Huerre, M. (1996) Infection of rabbit Peyer's patches by Shigella flexneri: effect of adhesive or invasive bacterial phenotypes on follicle-associated epithelium. *Infect Immun* **64**, 2752-2764
15. Lafont, F., Tran Van Nhieu, G., Hanada, K., Sansonetti, P., and van der Goot, F. G. (2002) Initial steps of Shigella infection depend on the cholesterol/sphingolipid raft-mediated CD44-IpaB interaction. *EMBO J* **21**, 4449-4457
16. Tran Van Nhieu, G., Caron, E., Hall, A., and Sansonetti, P. J. (1999) IpaC induces actin polymerization and filopodia formation during Shigella entry into epithelial cells. *EMBO J* **18**, 3249-3262

17. Terry, C. M., Picking, W. L., Birket, S. E., Flentie, K., Hoffman, B. M., Barker, J. R., and Picking, W. D. (2008) The C-terminus of IpaC is required for effector activities related to Shigella invasion of host cells. *Microb Pathog* **45**, 282-289
18. Yoshida, S., Katayama, E., Kuwae, A., Mimuro, H., Suzuki, T., and Sasakawa, C. (2002) Shigella deliver an effector protein to trigger host microtubule destabilization, which promotes Rac1 activity and efficient bacterial internalization. *EMBO J* **21**, 2923-2935
19. Sansonetti, P. J., Ryter, A., Clerc, P., Maurelli, A. T., and Mounier, J. (1986) Multiplication of Shigella flexneri within HeLa cells: lysis of the phagocytic vacuole and plasmid-mediated contact hemolysis. *Infect Immun* **51**, 461-469
20. Glick, D., Barth, S., and Macleod, K. F. (2010) Autophagy: cellular and molecular mechanisms. *J Pathol* **221**, 3-12
21. Ogawa, M., Suzuki, T., Tatsuno, I., Abe, H., and Sasakawa, C. (2003) IcsB, secreted via the type III secretion system, is chaperoned by IpgA and required at the post-invasion stage of Shigella pathogenicity. *Mol Microbiol* **48**, 913-931
22. Ogawa, M., Yoshimori, T., Suzuki, T., Sagara, H., Mizushima, N., and Sasakawa, C. (2005) Escape of intracellular Shigella from autophagy. *Science* **307**, 727-731
23. Yoshida, S., Handa, Y., Suzuki, T., Ogawa, M., Suzuki, M., Tamai, A., Abe, A., Katayama, E., and Sasakawa, C. (2006) Microtubule-severing activity of Shigella is pivotal for intercellular spreading. *Science* **314**, 985-989
24. Hilbi, H., Moss, J. E., Hersh, D., Chen, Y., Arondel, J., Banerjee, S., Flavell, R. A., Yuan, J., Sansonetti, P. J., and Zychlinsky, A. (1998) Shigella-induced apoptosis is dependent on caspase-1 which binds to IpaB. *J Biol Chem* **273**, 32895-32900
25. Senerovic, L., Tsunoda, S. P., Goosmann, C., Brinkmann, V., Zychlinsky, A., Meissner, F., and Kolbe, M. (2012) Spontaneous formation of IpaB ion channels in host cell membranes reveals how Shigella induces pyroptosis in macrophages. *Cell Death Dis* **3**, e384
26. Arizmendi, O., Picking, W. D., and Picking, W. L. (2016) Macrophage Apoptosis Triggered by IpaD from Shigella flexneri. *Infection and Immunity* **84**, 1857-1865
27. Suzuki, T., Nakanishi, K., Tsutsui, H., Iwai, H., Akira, S., Inohara, N., Chamaillard, M., Nunez, G., and Sasakawa, C. (2005) A novel caspase-1/toll-like receptor 4-independent pathway of cell death induced by cytosolic Shigella in infected macrophages. *J Biol Chem* **280**, 14042-14050
28. Kohler, H., Rodrigues, S. P., and McCormick, B. A. (2002) Shigella flexneri Interactions with the Basolateral Membrane Domain of Polarized Model Intestinal Epithelium: Role of Lipopolysaccharide in Cell Invasion and in Activation of the Mitogen-Activated Protein Kinase ERK. *Infect Immun* **70**, 1150-1158
29. Perdomo, J. J., Gounon, P., and Sansonetti, P. J. (1994) Polymorphonuclear leukocyte transmigration promotes invasion of colonic epithelial monolayer by Shigella flexneri. *J Clin Invest* **93**, 633-643
30. Kubori, T., Matsushima, Y., Nakamura, D., Uralil, J., Lara-Tejero, M., Sukhan, A., Galan, J. E., and Aizawa, S. I. (1998) Supramolecular structure of the Salmonella typhimurium type III protein secretion system. *Science* **280**, 602-605
31. Blocker, A., Jouihri, N., Larquet, E., Gounon, P., Ebel, F., Parsot, C., Sansonetti, P., and Allaoui, A. (2001) Structure and composition of the Shigella flexneri "needle complex", a part of its type III secreton. *Mol Microbiol* **39**, 652-663

32. Hodgkinson, J. L., Horsley, A., Stabat, D., Simon, M., Johnson, S., da Fonseca, P. C., Morris, E. P., Wall, J. S., Lea, S. M., and Blocker, A. J. (2009) Three-dimensional reconstruction of the Shigella T3SS transmembrane regions reveals 12-fold symmetry and novel features throughout. *Nat Struct Mol Biol* **16**, 477-485
33. Deane, J. E., Roversi, P., Cordes, F. S., Johnson, S., Kenjale, R., Daniell, S., Booy, F., Picking, W. D., Picking, W. L., Blocker, A. J., and Lea, S. M. (2006) Molecular model of a type III secretion system needle: Implications for host-cell sensing. *Proc Natl Acad Sci U S A* **103**, 12529-12533
34. Cordes, F. S., Komoriya, K., Larquet, E., Yang, S., Egelman, E. H., Blocker, A., and Lea, S. M. (2003) Helical structure of the needle of the type III secretion system of Shigella flexneri. *J Biol Chem* **278**, 17103-17107
35. Fujii, T., Cheung, M., Blanco, A., Kato, T., Blocker, A. J., and Namba, K. (2012) Structure of a type III secretion needle at 7-Å resolution provides insights into its assembly and signaling mechanisms. *Proceedings of the National Academy of Sciences* **109**, 4461-4466
36. Epler, C. R., Dickenson, N. E., Bullitt, E., and Picking, W. L. (2012) Ultrastructural analysis of IpaD at the tip of the nascent MxiH type III secretion apparatus of Shigella flexneri. *J Mol Biol* **420**, 29-39
37. Espina, M., Olive, A. J., Kenjale, R., Moore, D. S., Ausar, S. F., Kaminski, R. W., Oaks, E. V., Middaugh, C. R., Picking, W. D., and Picking, W. L. (2006) IpaD localizes to the tip of the type III secretion system needle of Shigella flexneri. *Infect Immun* **74**, 4391-4400
38. Olive, A. J., Kenjale, R., Espina, M., Moore, D. S., Picking, W. L., and Picking, W. D. (2007) Bile salts stimulate recruitment of IpaB to the Shigella flexneri surface, where it colocalizes with IpaD at the tip of the type III secretion needle. *Infect Immun* **75**, 2626-2629
39. Barta, M. L., Guragain, M., Adam, P., Dickenson, N. E., Patil, M., Geisbrecht, B. V., Picking, W. L., and Picking, W. D. (2012) Identification of the bile salt binding site on ipad from Shigella flexneri and the influence of ligand binding on IpaD structure. *Proteins: Structure, Function, and Bioinformatics* **80**, 935-945
40. Dickenson, N. E., Choudhari, S. P., Adam, P. R., Kramer, R. M., Joshi, S. B., Middaugh, C. R., Picking, W. L., and Picking, W. D. (2013) Oligomeric states of the Shigella translocator protein IpaB provide structural insights into formation of the type III secretion translocon. *Protein Sci* **22**, 614-627
41. Picking, W. L., and Picking, W. D. (2016) The Many Faces of IpaB. *Front Cell Infect Microbiol* **6**, 12
42. Blocker, A., Gounon, P., Larquet, E., Niebuhr, K., Cabiaux, V., Parsot, C., and Sansonetti, P. (1999) The tripartite type III secreton of Shigella flexneri inserts IpaB and IpaC into host membranes. *J Cell Biol* **147**, 683-693
43. Ward, J. E., Jr., and Lutkenhaus, J. (1985) Overproduction of FtsZ induces minicell formation in E. coli. *Cell* **42**, 941-949
44. Bi, E., and Lutkenhaus, J. (1990) FtsZ regulates frequency of cell division in Escherichia coli. *J Bacteriol* **172**, 2765-2768
45. Hu, B., Morado, D. R., Margolin, W., Rohde, J. R., Arizmendi, O., Picking, W. L., Picking, W. D., and Liu, J. (2015) Visualization of the type III secretion sorting platform of Shigella flexneri. *Proc Natl Acad Sci U S A* **112**, 1047-1052

46. Chen, S., Beeby, M., Murphy, G. E., Leadbetter, J. R., Hendrixson, D. R., Briegel, A., Li, Z., Shi, J., Tocheva, E. I., Muller, A., Dobro, M. J., and Jensen, G. J. (2011) Structural diversity of bacterial flagellar motors. *EMBO J* **30**, 2972-2981
47. Demler, H. J., Case, H. B., Morales, Y., Bernard, A. R., Johnson, S. J., and Dickenson, N. E. (2019) Interfacial Amino Acids Support Spa47 Oligomerization and Shigella Type Three Secretion System Activation. *Proteins*
48. Burgess, J. L., Jones, H. B., Kumar, P., Toth, R. T. t., Middaugh, C. R., Antony, E., and Dickenson, N. E. (2016) Spa47 is an oligomerization-activated type three secretion system (T3SS) ATPase from Shigella flexneri. *Protein Sci* **25**, 1037-1048
49. Burgess, J. L., Burgess, R. A., Morales, Y., Bouvang, J. M., Johnson, S. J., and Dickenson, N. E. (2016) Structural and Biochemical Characterization of Spa47 Provides Mechanistic Insight into Type III Secretion System ATPase Activation and Shigella Virulence Regulation. *J Biol Chem* **291**, 25837-25852
50. Lara-Tejero, M., Kato, J., Wagner, S., Liu, X., and Galan, J. E. (2011) A sorting platform determines the order of protein secretion in bacterial type III systems. *Science* **331**, 1188-1191
51. Akeda, Y., and Galán, J. E. (2005) Chaperone release and unfolding of substrates in type III secretion. *Nature* **437**, 911-915
52. Hu, J., Worrall, L. J., Hong, C., Vuckovic, M., Atkinson, C. E., Caveney, N., Yu, Z., and Strynadka, N. C. J. (2018) Cryo-EM analysis of the T3S injectisome reveals the structure of the needle and open secretin. *Nature Communications* **9**, 3840
53. Case, H. B., and Dickenson, N. E. (2018) MxiN Differentially Regulates Monomeric and Oligomeric Species of the Shigella Type Three Secretion System ATPase Spa47. *Biochemistry* **57**, 2266-2277
54. Erhardt, M., Mertens, M. E., Fabiani, F. D., and Hughes, K. T. (2014) ATPase-independent type-III protein secretion in Salmonella enterica. *PLoS Genet* **10**, e1004800
55. Morimoto, Y. V., Kami-Ike, N., Miyata, T., Kawamoto, A., Kato, T., Namba, K., and Minamino, T. (2016) High-Resolution pH Imaging of Living Bacterial Cells To Detect Local pH Differences. *MBio* **7**
56. McDowell, M. A., Johnson, S., Deane, J. E., Cheung, M., Roehrich, A. D., Blocker, A. J., McDonnell, J. M., and Lea, S. M. (2011) Structural and functional studies on the N-terminal domain of the Shigella type III secretion protein MxiG. *J Biol Chem* **286**, 30606-30614
57. Tachiyama, S., Chang, Y., Muthuramalingam, M., Hu, B., Barta, M. L., Picking, W. L., Liu, J., and Picking, W. D. (2019) The cytoplasmic domain of MxiG interacts with MxiK and directs assembly of the sorting platform in the Shigella type III secretion system. *Journal of Biological Chemistry* **294**, 19184-19196
58. Marlovits, T. C., Kubori, T., Sukhan, A., Thomas, D. R., Galan, J. E., and Unger, V. M. (2004) Structural insights into the assembly of the type III secretion needle complex. *Science* **306**, 1040-1042
59. Hu, B., Lara-Tejero, M., Kong, Q., Galan, J. E., and Liu, J. (2017) In Situ Molecular Architecture of the Salmonella Type III Secretion Machine. *Cell* **168**, 1065-1074 e1010
60. Durocher, D., and Jackson, S. P. (2002) The FHA domain. *FEBS Letters* **513**, 58-66
61. Mahajan, A., Yuan, C., Lee, H., Chen, E. S.-W., Wu, P.-Y., and Tsai, M.-D. (2008) Structure and Function of the Phosphothreonine-Specific FHA Domain. *Science Signaling* **1**, re12-re12

62. Barison, N., Lambers, J., Hurwitz, R., and Kolbe, M. (2012) Interaction of MxiG with the cytosolic complex of the type III secretion system controls Shigella virulence. *FASEB J* **26**, 1717-1726
63. McDowell, M. A., Marcoux, J., McVicker, G., Johnson, S., Fong, Y. H., Stevens, R., Bowman, L. A., Degiacomi, M. T., Yan, J., Wise, A., Friede, M. E., Benesch, J. L., Deane, J. E., Tang, C. M., Robinson, C. V., and Lea, S. M. (2016) Characterisation of Shigella Spa33 and Thermotoga FliM/N reveals a new model for C-ring assembly in T3SS. *Mol Microbiol* **99**, 749-766
64. Bzymek, K. P., Hamaoka, B. Y., and Ghosh, P. (2012) Two translation products of Yersinia yscQ assemble to form a complex essential to type III secretion. *Biochemistry* **51**, 1669-1677
65. Lara-Tejero, M., Qin, Z., Hu, B., Butan, C., Liu, J., and Galan, J. E. (2019) Role of SpaO in the assembly of the sorting platform of a Salmonella type III secretion system. *PLoS Pathog* **15**, e1007565
66. Lam, K. H., Xue, C., Sun, K., Zhang, H., Lam, W. W. L., Zhu, Z., Ng, J. T. Y., Sause, W. E., Lertsethtakarn, P., Lau, K. F., Ottemann, K. M., and Au, S. W. N. (2018) Three SpoA-domain proteins interact in the creation of the flagellar type III secretion system in Helicobacter pylori. *J Biol Chem* **293**, 13961-13973
67. Notti, R. Q., Bhattacharya, S., Lilic, M., and Stebbins, C. E. (2015) A common assembly module in injectisome and flagellar type III secretion sorting platforms. *Nat Commun* **6**, 7125
68. Yu, X. J., Liu, M., Matthews, S., and Holden, D. W. (2011) Tandem translation generates a chaperone for the Salmonella type III secretion system protein SsaQ. *J Biol Chem* **286**, 36098-36107
69. CDC. (2016) Salmonella [PDF file] https://www.cdc.gov/salmonella/pdf/CDC-Salmonella-Factsheet.pdf Accessed: 13 April 2020.
70. Ramos-Morales, F. (2012) Impact of Salmonella enterica Type III Secretion System Effectors on the Eukaryotic Host Cell. *ISRN Cell Biology* **2012**, 36
71. Hardt, W.-D., Chen, L.-M., Schuebel, K. E., Bustelo, X. R., and Galán, J. E. (1998) S. typhimurium Encodes an Activator of Rho GTPases that Induces Membrane Ruffling and Nuclear Responses in Host Cells. *Cell* **93**, 815-826
72. Boyle, E. C., Brown, N. F., and Finlay, B. B. (2006) Salmonella enterica serovar Typhimurium effectors SopB, SopE, SopE2 and SipA disrupt tight junction structure and function. *Cellular Microbiology* **8**, 1946-1957
73. Cascales, E. (2017) Inside the Chamber of Secrets of the Type III Secretion System. *Cell* **168**, 949-951
74. Bernal, I., Börnicke, J., Heidemann, J., Svergun, D., Horstmann, J. A., Erhardt, M., Tuukkanen, A., Uetrecht, C., and Kolbe, M. (2019) Molecular Organization of Soluble Type III Secretion System Sorting Platform Complexes. *Journal of Molecular Biology* **431**, 3787-3803
75. Picking, W. L., Nishioka, H., Hearn, P. D., Baxter, M. A., Harrington, A. T., Blocker, A., and Picking, W. D. (2005) IpaD of Shigella flexneri Is Independently Required for Regulation of Ipa Protein Secretion and Efficient Insertion of IpaB and IpaC into Host Membranes. *Infection and Immunity* **73**, 1432-1440
76. Battesti, A., and Bouveret, E. (2012) The bacterial two-hybrid system based on adenylate cyclase reconstitution in Escherichia coli. *Methods* **58**, 325-334

77. Geisbrecht, B. V., Bouyain, S., and Pop, M. (2006) An optimized system for expression and purification of secreted bacterial proteins. *Protein Expression and Purification* **46**, 23-32
78. Ménard, R., Sansonetti, P. J., and Parsot, C. (1993) Nonpolar mutagenesis of the ipa genes defines IpaB, IpaC, and IpaD as effectors of Shigella flexneri entry into epithelial cells. *Journal of Bacteriology* **175**, 5899-5906
79. Hueck, C. J. (1998) Type III Protein Secretion Systems in Bacterial Pathogens of Animals and Plants. *Microbiology and Molecular Biology Reviews* **62**, 379-433
80. Abrusci, P., McDowell, M. A., Lea, S. M., and Johnson, S. (2014) Building a secreting nanomachine: a structural overview of the T3SS. *Current Opinion in Structural Biology* **25**, 111-117
81. Portaliou, A. G., Tsolis, K. C., Loos, M. S., Zorzini, V., and Economou, A. (2016) Type III Secretion: Building and Operating a Remarkable Nanomachine. *Trends in Biochemical Sciences* **41**, 175-189
82. Diepold, A., and Armitage, J. P. (2015) Type III secretion systems: the bacterial flagellum and the injectisome. *Philos Trans R Soc Lond B Biol Sci* **370**
83. Deng, W., Marshall, N. C., Rowland, J. L., McCoy, J. M., Worrall, L. J., Santos, A. S., Strynadka, N. C. J., and Finlay, B. B. (2017) Assembly, structure, function and regulation of type III secretion systems. *Nature Reviews Microbiology* **15**, 323-337
84. Jouihri, N., Sory, M.-P., Page, A.-L., Gounon, P., Parsot, C., and Allaoui, A. (2003) MxiK and MxiN interact with the Spa47 ATPase and are required for transit of the needle components MxiH and MxiI, but not of Ipa proteins, through the type III secretion apparatus of Shigella flexneri. *Molecular Microbiology* **49**, 755-767
85. Barta, M. L., Tachiyama, S., Muthuramalingam, M., Arizmendi, O., Villanueva, C. E., Ramyar, K. X., Geisbrecht, B. V., Lovell, S., Battaile, K. P., Picking, W. L., and Picking, W. D. (2018) Using disruptive insertional mutagenesis to identify the in situ structure-function landscape of the Shigella translocator protein IpaB. *Protein Sci* **27**, 1392-1406
86. Yoshida, M., Muneyuki, E., and Hisabori, T. (2001) ATP synthase — a marvellous rotary engine of the cell. *Nature Reviews Molecular Cell Biology* **2**, 669-677
87. Yasuda, R., Noji, H., Yoshida, M., Kinosita, K., and Itoh, H. (2001) Resolution of distinct rotational substeps by submillisecond kinetic analysis of F1-ATPase. *Nature* **410**, 898-904
88. Gamez, A., Mukerjea, R., Alayyoubi, M., Ghassemian, M., and Ghosh, P. (2012) Structure and Interactions of the Cytoplasmic Domain of the Yersinia Type III Secretion Protein YscD. *Journal of Bacteriology* **194**, 5949-5958
89. Tong, Y., Tempel, W., Wang, H., Yamada, K., Shen, L., Senisterra, G. A., MacKenzie, F., Chishti, A. H., and Park, H.-W. (2010) Phosphorylation-independent dual-site binding of the FHA domain of KIF13 mediates phosphoinositide transport via centaurin α1. *Proceedings of the National Academy of Sciences* **107**, 20346-20351
90. Bergeron, J. R. C., Worrall, L. J., Sgourakis, N. G., DiMaio, F., Pfuetzner, R. A., Felise, H. B., Vuckovic, M., Yu, A. C., Miller, S. I., Baker, D., and Strynadka, N. C. J. (2013) A Refined Model of the Prototypical Salmonella SPI-1 T3SS Basal Body Reveals the Molecular Basis for Its Assembly. *PLOS Pathogens* **9**, e1003307
91. Greenfield, N. J. (2006) Using circular dichroism spectra to estimate protein secondary structure. *Nature Protocols* **1**, 2876-2890

92. Pallen, M. J., Bailey, C. M., and Beatson, S. A. (2006) Evolutionary links between FliH/YscL-like proteins from bacterial type III secretion systems and second-stalk components of the FoF1 and vacuolar ATPases. *Protein Science* **15**, 935-941
93. Imada, K., Minamino, T., Uchida, Y., Kinoshita, M., and Namba, K. (2016) Insight into the flagella type III export revealed by the complex structure of the type III ATPase and its regulator. *Proceedings of the National Academy of Sciences* **113**, 3633-3638
94. Minamino, T., and Macnab, R. M. (2000) FliH, a soluble component of the type III flagellar export apparatus of Salmonella, forms a complex with FliI and inhibits its ATPase activity. *Molecular Microbiology* **37**, 1494-1503
95. Auvray, F., Ozin, A. J., Claret, L., and Hughes, C. (2002) Intrinsic Membrane Targeting of the Flagellar Export ATPase FliI: Interaction with Acidic Phospholipids and FliH. *Journal of Molecular Biology* **318**, 941-950
96. Morita-Ishihara, T., Ogawa, M., Sagara, H., Yoshida, M., Katayama, E., and Sasakawa, C. (2006) Shigella Spa33 Is an Essential C-ring Component of Type III Secretion Machinery. *Journal of Biological Chemistry* **281**, 599-607
97. Au - Shah, N. B., and Au - Duncan, T. M. (2014) Bio-layer Interferometry for Measuring Kinetics of Protein-protein Interactions and Allosteric Ligand Effects. *JoVE*, e51383
98. Lyons, B. J. E., and Strynadka, N. C. J. (2019) On the road to structure-based development of anti-virulence therapeutics targeting the type III secretion system injectisome. *MedChemComm* **10**, 1273-1289
99. Diepold, A., Amstutz, M., Abel, S., Sorg, I., Jenal, U., and Cornelis, G. R. (2010) Deciphering the assembly of the Yersinia type III secretion injectisome. *The EMBO Journal* **29**, 1928-1940
100. Wagner, S., Königsmaier, L., Lara-Tejero, M., Lefebre, M., Marlovits, T. C., and Galán, J. E. (2010) Organization and coordinated assembly of the type III secretion export apparatus. *Proceedings of the National Academy of Sciences* **107**, 17745-17750
101. Orfanoudaki, G., and Economou, A. (2014) Proteome-wide Subcellular Topologies of E. coli Polypeptides Database (STEPdb). *Molecular & Cellular Proteomics* **13**, 3674-3687
102. Lara-Tejero, M., and Galán, J. (2019) The Injectisome, a Complex Nanomachine for Protein Injection into Mammalian Cells. *EcoSal Plus*

Appendix

Appendix A: Buffers and reagents

Buffers

Phosphate-buffered saline (PBS)
10 mM Phosphate pH 7.4
136.9 mM Sodium chloride
2.7 mM Potassium chloride

His-tag strip buffer
20 mM Tris pH 7.9
500 mM Sodium chloride
100 mM EDTA

His-tag charge buffer
200 mM Nickel (II) sulfate hexahydrate

IMAC binding buffer
20 mM Tris pH 7.9
5.0 mM Imidazole
500 mM Sodium chloride

IMAC elution buffer
20 mM Tris pH 7.9
400 mM Imidazole
500 mM Sodium chloride

Q binding buffer for Spa33
20 mM Tris pH 7.5

Q elution buffer for Spa33
20 mM Tris pH 7.5
1.0 M Sodium chloride

Size exclusion chromatography (SEC) buffer for Spa33
20 mM Tris pH 7.5
200 mM Sodium chloride

IMAC binding buffer for the MxiK-T4L fusion proteins
20 mM Tris pH 7.9
5.0 mM Imidazole
500 mM Sodium chloride

0.1 % (v/v) LDAO (N,N-Dimethyldodecylamine N-oxide solution)

IMAC elution buffer for MxiK-T4L fusion proteins

20 mM Tris pH 7.9
400 mM Imidazole
500 mM Sodium chloride
0.1 % (v/v) LDAO (N,N-Dimethyldodecylamine N-oxide solution)

SEC buffer for MxiK

20 mM Tris pH 7.5
200 mM Sodium chloride
1.0 mM EDTA
1.0 mM TCEP (tris(2-carboxyethyl)phosphine hydrochloride)
0.1 % (v/v) LDAO (N,N-Dimethyldodecylamine N-oxide solution)

Buffer for MxiK CD spectroscopy

0.1 % (v/v) LDAO in PBS

SEC buffer for MxiN

20 mM Tris pH 7.0
300 mM Sodium chloride
1.0 mM TCEP
15 % (v/v) Glycerol

SEC buffer for preparing the MxiN-Spa33 complex

50 mM Sodium citrate pH 7.0
150 mM Sodium chloride
1.0 mM TCEP
10 % (v/v) Glycerol

BLI buffer for measuring the MxiN-Spa33 interaction

34.42 mM Sodium phosphate dibasic anhydrous pH 7.0
15.58 mM Potassium phosphate monobasic
150 mM Sodium chloride
10 % (v/v) Glycerol

NMR buffer for MxiN

50 mM Sodium citrate pH 7.0
150 mM Sodium chloride
10 % (v/v) Glycerol
1.0 mM TCEP

10% SDS-PAGE resolving gel (for two gels)

4.0 mL diH_2O
2.5 mL 1.5M Tris pH 8.8
3.33 mL 29:1 % (w/v) Acrylamide:bis-acrylamide

100 µL 10 % (w/v) SDS
150 µL 10 % (w/v) Ammonium persulfate (APS)
13 µL TEMED

15% SDS-PAGE resolving gel (for two gels)

2.5 mL diH_2O
2.5 mL 1.5M Tris pH 8.8
5.0 mL 29:1 % (w/v) Acrylamide:bis-acrylamide
100 µL 10 % (w/v) SDS
150 µL 10 % (w/v) Ammonium persulfate (APS)
13 µL TEMED

5.0% SDS-PAGE resolving gel (for two gels)

2.85 mL diH_2O
1.25 mL 0.5M Tris pH 6.8
1.0 mL 29:1 % (w/v) Acrylamide:bis-acrylamide
50.0 µL 10 % (w/v) SDS
88.0 µL 10 % (w/v) Ammonium persulfate (APS)
10 µL TEMED

Coomassie brilliant blue stain

0.1 % (w/v) Coomassie R250
50 % (v/v) Methanol
10 % (v/v) Acetic acid

Coomassie blue destain solution

30 % (v/v) Methanol
10 % (v/v) Acetic acid

3× SDS-PAGE sample buffer

210 mM Tris pH 6.8
100 mM Sodium chloride
3.0 mM EDTA
6.0 % (w/v) SDS
30 % (v/v) Glycerol
3.0 mM Sodium azide
0.03 % (w/v) Bromophenol blue
3.0 mM DTT

Blotting buffer for immunoblotting

60 mL diH_2O
20 mL 100 % (v/v) Ethanol
20 mL Trans-Blot Turbo 5× Transfer Buffer (from Bio-red Laboratories)

Tris-buffered saline (TBS)

25 mM Tris pH 7.5

150 mM Sodium chloride

TBS with Tween 20

25 mM Tris pH7.5
150 mM Sodium chloride
0.05 % (v/v) Tween 20

Immunoblot blocking buffer

10 mL of TBS
10 mL of Odyssey Blocking Buffer (TBS) (from LI-COR)

Bacterial Growth Medium

LB (pre-mix)

10 g/L Tryptone
5.0 g/L Yeast extract
10 g/L Sodium chloride

LB Agar (pre-mix)

10 g/L Casein peptone
5.0 g/L Yeast extract
10 g/L Sodium chloride
12 g/L Agar

TSB (pre-mix)

17.0 g/L Peptone from casein
3.0 g/L Peptone from soymeal
2.5 g/L D-(+)-glucose
5.0 g/L Sodium chloride
2.5 g/L Dipotassium hydrogen phosphate

TSA (pre-mix)

15.0 g/L Peptone from casein
5.0 g/L Peptone from soymeal
5.0 g/L Sodium chloride
15.0 g/L Agar

Congo red agar plates

40 g/L TSA
0.25 g/L Congo red

MacConkey agar base (pre-mix)

17.0 g/L Peptone
3.0 g/L Proteose peptone
1.5 g/L Bile salt No.3

5.0 g/L Sodium chloride
13.5 g/L Agar
0.03 g/L Neutral red
0.001 g/L Crystal violet

MacConkey agar plates with maltose

40 g/L MacConkey agar base
1.0 % (w/v) D-(+)-Maltose Monohydrate

M63 minimal medium agar plates with X-gal

2.0 g/L Ammonium sulfate
13.6 g/L Potassium phosphate monobasic
0.5 mg/L Ferrous sulfate heptahydrate
15.0 g/L Agar
1.0 mM Magnesium sulfate heptahydrate
0.2 % (w/v) Maltose
0.0001 % (w/v) Thiamin
0.1 mM IPTG
40 µg/mL X-gal (5-Bromo-4-chloro-3-indolyl- β-D-galactopyranoside)

M63 minimal medium

2.0 g/L Ammonium sulfate
13.6 g/L Potassium phosphate monobasic
0.5 mg/L Ferrous sulfate heptahydrate

10x M9 minimal medium

30 g/L Potassium phosphate monobasic pH 7.2
66.52 g/L Sodium phosphate dibasic
5 g/L Sodium chloride

Cai trace element (in 100mL)

60 mg Calcium chloride
7.0 mg Zinc sulfate heptahydrate
60mg Ferrous sulfate monohydrate
3.0 mg Cupric chloride dihydrate
50 mg EDTA
2.5 mg Ammonium heptamolybdate tetrahydrate
11.5 mg Manganese (II) chloride tetrahydrate
0.2 mg Boric acid
8.0 mg Cobaltous chloride hexahydrate

M9 minimal medium

4.0 g/L Glucose
1.5 g/L ^{15}N labeled ammonium chloride
10 mL BME Vitamins solution 100×
4.0 mM Magnesium sulfate

0.2 mM Calcium chloride
2.0 mL/L Cai trace element
100 mL/L 10× M9 minimal medium

Appendix B: Table of primer sequences

Name	Direction	Sequence (5'- to -3')	Purpose
T4L Linker	Fw	GGTTCAATGAACATCTTCGAAATGC TGCGTATCGACGCTG	Amplify T4L for insertion
	Rev	TGAACCCCTGTAAGCGTCCCAGGTT CCG	
MxiK_T4L_25	Fw	GCTTACAGGGGTTCACGGTTGAATT TGCCTTCTGAACTGTTAGAAAATG	To prepare insertion site at residue 25 in MxiK
	Rev	GATGTTCATTGAACCATTTCTATTT ATATAGAACGCTGGATCAAAAATT ATTGAAAGA	
MxiK_T4L_55	Fw	GCTTACAGGGGTTCAGATATTGAAC CTTTAAGCGGGGTAA	To prepare insertion site at residue 55 in MxiK
	Rev	GATGTTCATTGAACCGCAATTTAGA TCATATTTATTAATTATGAGATTAT TAATC	
MxiK_T4L_136	Fw	GCTTACAGGGGTTCATTTAATCCAA TTGCTTTGGAGGGAAATTATAC	To prepare insertion site at residue 136 in MxiK
	Rev	GATGTTCATTGAACCTAATAAGTTT ATTCTTTCATATATACCAACAGAT	
MxiK_BACTH	Fw	AAAAAAGGATCCCATGATAAGAAT GGATGGA	For cloning MxiK for BACTH
	Rev	AAAAAAGGTACCATTAGGCATGAT GTCTGGATACCGGTAAAGTG	
MxiK_T4L_C_BA CTH	Rev	TTTTTTGGTACCCCTGTAAGCGTCC CAGGTT	For cloning MxiK-T4L-C for BACTH
MxiK.3.1	Fw	AAAAAAGGATCCATGATAAGAATG GATGGA	For cloning of MxiK into pT7HMT
MxiK.3.175.NotI	Rev	TTTTTTGCGGCCGCTAGGCATGATG TCTGGAT	
MxiK_Stop_175	Fw	TTTACCGGTATCCAGACATCATGCC TATAATAAGCACTCGAGCACCAC	Introducing stop codons after MxiK
	Rev	GTGGTGCTCGAGTGCTTATTATAGG CATGATGTCTGGATACCGGTAAA	
MxiK_51A55	Fw	GCTGCAGCAGCTGCTGATATTGAAC CTTTAAGC	Introduce five Ala between 51 and 55
	Rev	AGCAGCTGCTGCAGCTTTATTAATT ATGAGATTATTAATCTCAC	

MxiK_51A60	Fw	GCTGCAGCAGCTGCTAGCGGGGTAACCGCTATGTTTGTT	Introduce 10 Ala between 51 and 60
	Rev	AGCAGCTGCTGCAGCAGCAGCTGCTGCAGCTTTATTAATTATGAGATTATTAAT	
MxiK_Y51A	Fw	CATAATTAATAAAGCAGATCTAAATTGCGATATTGAACCTTTAAGC	Introduce Ala at residue 51 in MxiK
	Rev	GCTTAAAGGTTCAATATCGCAATTTAGATCTGCTTTATTAATTATG	
MxiK_D52A	Fw	CATAATTAATAAATATGCACTAAATTGCGATATTGAACCTTTAAGC	Introduce Ala at residue 52 in MxiK
		GCTTAAAGGTTCAATATCGCAATTTAGTGCATATTTATTAATTATG	
MxiK_L53A	Fw	TTAATAAATATGATGCAAATTGCGATATTGAACCTTTAAGC	Introduce Ala at residue 53 in MxiK
	Rev	GCTTAAAGGTTCAATATCGCAATTTGCATCATATTTATTAA	
MxiK_N54A	Fw	CATAATTAATAAATATGATCTAGCATGCGATATTGAACCTTTAAGC	Introduce Ala at residue 54 in MxiK
	Rev	GCTTAAAGGTTCAATATCGCATGCTAGATCATATTTATTAATTATG	
MxiK_C55A	Fw	CATAATTAATAAATATGATCTAAATGCAGATATTGAACCTTTAAGC	Introduce Ala at residue 55 in MxiK
	Rev	GCTTAAAGGTTCAATATCTGCATTTAGATCATATTTATTAATTATG	
MxiK_D56A	Fw	GATCTAAATTGCGCAATTGAACCTTTAAGCG	Introduce Ala at residue 56 in MxiK
	Rev	CGCTTAAAGGTTCAATTGCGCAATTTAGATC	
MxiK_134Ala138	Fw	GCTGCAGCAGCTGCTCCAATTGCTTTGGAGGGAAATTATA	Introduce five Ala between residues 134 and 138 in MxiK
	Rev	AGCAGCTGCTGCAGCTATTCTTTCATATATACCAACAGATATATTTTCCTT	
MxiK_134_Ala	Fw	ATGAAAGAATAGCATTATTATTTAATCCAATTGC	Introduce Ala at residue 134 in MxiK
	Rev	GCAATTGGATTAAATAATAATGCTATTCTTTCAT	
MxiK_135Ala	Fw	ATGAAAGAATAAACGCATTATTTAATCCAATTGC	Introduce Ala at residue 135 in MxiK
	Rev	GCAATTGGATTAAATAATGCGTTTATTCTTTCAT	
MxiK_136_Ala	Fw	ATGAAAGAATAAACTTAGCATTTAATCCAATTGC	Introduce Ala at

	Rev	GCAATTGGATTAAATGCTAAGTTTATTCTTTCAT	residue 136 in MxiK
MxiK_137_Ala	Fw	ATGAAAGAATAAACTTATTAGCAAATCCAATTGC	Introduce Ala at residue 137 in MxiK
	Rev	GCAATTGGATTTGCTAATAAGTTTATTCTTTCAT	
MxiK_138_Ala	Fw	ATGAAAGAATAAACTTATTATTTGCACCAATTGC	Introduce Ala at residue 138 in MxiK
	Rev	GCAATTGGTGCAAATAATAAGTTTATTCTTTCAT	
MxiG_18Ala22	Fw	GCCGCAGCCGCTGCCGGGGATGAGTTTCCGTTATATTATGGGAATAACTTAATT	Introduce Ala between residue 18 and 22 in MxiG
	Rev	GGCAGCGGCTGCGGCTTTCACTAATAACCTGAATGGTGCAAGATTTGA	
MxiG_47Ala52	Fw	GCAGCCGCCGCTGCCGCAGAAAATATTATTCCTGTAACAGATAGTAAATCGGAT	Introduce Ala between residue 47 and 52 in MxiG
	Rev	TGCGGCAGCGGCGGCTGCAAACTCAAGTGTTTCTATCGTCCGT	
MxiG_61Ala66	Fw	GCTGCAGCGGCTGCTGCAATTTATTTGACCATAAGCAAAGATAATATCTGTCAATTTAGT	Introduce Ala between residue 61 and 66 in MxiG
	Rev	TGCAGCAGCCGCTGCAGCATCTGTTACAGGAATAATATTTTCTGGGAAATTGTCGTTTCC	
MxiG_81Ala85	Fw	GCTGCAGCAGCTGCGCAAATTGATATCAATTCACAATTTAATTCATTTGAATATGAC	Introduce Ala between residue 81 and 85 in MxiG
	Rev	CGCAGCTGCTGCAGCACTAAATTGACAGATATTATCTTTGCTTATGGTCAAATA	
MxiG_86Ala94	Fw	GCAGCTGCTGCCGCTGCAGCAGCTGCTTCATTTGAATATGACGGGATTTCTTTTCACCTT	Introduce Ala between residue 86 and 94 in MxiG
	Rev	AGCAGCTGCTGCAGCGGCAGCAGCTGCCTCACCTTTTTCATCACTAAATTGACAGATATT	
MxiG_D99N	Fw	TTTGAATATAACGGGATTTCTTTTCACCTTAAAAATATGAGGGAGGATAAATCGAGAGGC	Introduce Asn at residues 99 in MxiG
	Rev	GCCTCTCGATTTATCCTCCCTCATATTTTTAAGGTGAAAAGAAATCCCGTTATATTCAAA	

MxiG_D99K	Fw	TTTGAATATAAGGGGATTTCTTTTCACCTTAAAAATATGAGGGAGGATAAATCGAGAGGC	Introduce Lys at residues 99 in MxiG
	Rev	GCCTCTCGATTTATCCTCCCTCATATTTTTAAGGTGAAAAGAAATCCCCTTATATTCAAA	
MxiG_Linker_Add_5Gly	Fw	GGTGGGGGAGGTGGGCACTCGGTGTTTTTTTTCTTTGCTGTTATT	Insert five Gly at MxiG Linker
	Rev	CCCACCTCCCCCACCGTTCTTATACATTCCGTTTAGTATATGGCCTCTCGA	
MxiG_Linker_Add_10Gly	Fw	GGTGGGGGAGGTGGGGGTGGGGGAGGTGGGCACTCGGTGTTTTTTTTCTT	Insert 10 Gly at MxiG Linker
	Rev	CCCACCTCCCCCACCCCCACCTCCCCCACCGTTCTTATACATTCCGTTTAGTATAT	
MxiG_Linker_Del_G115_and_120	Fw	GAGGGAGGATAAATCGAGACATATACTAAACATGTATAAGAACCACTCGG	For $MxiG^{d115\ and\ 120}$ cloning
	Rev	CCGAGTGGTTCTTATACATGTTTAGTATATGTCTCGATTTATCCTCCCTC	
MxiG_Linker_Del_115_to_120	Fw	ATGTATAAGAACCACTCGGTGTTTTTTTTCTTTGC	For $MxiG^{d115\text{-}120}$ cloning
	Rev	GTGGTTCTTATACATTCTCGATTTATCCTCCCTCATATTTTT	
MxiG_Linker_Del_110_120_R	Rev	GTGGTTCTTATACATCCTCATATTTTTAAGGTGAAA	For $MxiG^{d110\text{-}120}$ cloning
MxiG_d108_124	Fw	CACTCGGTGTTTTTTTTCTTTGCTGTTATTG	For $MxiG^{d108\text{-}124}$ cloning
	Rev	AAAAAACACCGAGTGATTTTTAAGGTGAAAAGAAAT	
MxiG_d111_124_R	Rev	AAAAAACACCGAGTGCTCCCTCATATTTTTAAGG	For $MxiG^{d111\text{-}124}$ cloning
MxiG_d108_120_R	Rev	GTGGTTCTTATACATATTTTTAAGGTGAAAAGAAATCCCGTC	For $MxiG^{d108\text{-}120}$ cloning
MxiG_T4L_115_F	Fw	GCTTACAGGGGTTCACATATACTAAACGGAATGTATAAG	To prepare insertion site at residue 115 in MxiG
	Rev	GATGTTCATTGAACCGCCTCTCGATTTATCCTCCCT	
MxiG_2X_Link_F	Fw	TTTCACCTTAAAAATATGAGAGAGGATAAA	

	Rev	AAAGAAAAAAAACACCGAATGGTT	To amplify two length of MxiG Linker
PrgH_116_140_F	Fw	ATTTCTTTTCACCTTAGCGAGCCGTGGGTGCCCGA	To amplify PrgH Linker
	Rev	AAAGAAAAAAAACACAATTCCGTTTTTAAAACGCGGCTCGTTCTTTTTTGCAGA	
MxiG_127_Fw	FW	GTGTTTTTTTTCTTTGCTGTTATTGTTGTGTTAATTATAATT	To prepare insertion site in MxiG for PrgH Linker and 2x Linker
MxiG_105_Rev	Rev	AAGGTGAAAAGAAATCCCGTCATATTCAAA	To prepare insertion site in MxiG for PrgH
MxiG_107_Rev	Rev	ATTTTTAAGGTGAAAAGAAATCCCGTCATATTCAAA	To prepare insertion site in MxiG for 2x Linker

Appendix C: List of abbreviations

CDC – Centers for Disease Control and Prevention

NARMS – National Antimicrobial Resistance Monitoring System

LB – Luria Bertani medium

TSB – Tryptic Soy Broth

TSA – Tryptic Soy Agar

kb – kilo base

kDa – kilo Dalton

MW – Molecular weight

g – Gravity

spp. – species

T3SS – Type III Secretion System

T3SA – Type III Secretion Apparatus

SP – Cytoplasmic Sorting Platform

IR – Inner membrane ring

Ipa – Invasion plasmid antigen

Spa – Surface presentation of invasion plasmid antigen

Mxi – Membrane expression of invasion plasmid antigen

Sct – Secretion and cellular translocation

IPTG – Isopropyl β-D-1-thiogalactopyranoside

TCEPT – Tris (2-Carboxyethyl) phosphine Hydrochloride

IMAC – Immobilized metal affinity chromatography

Q – Anion exchange chromatography

SEC – Size exclusion chromatography

Cryo-ET – Cryo-Electron tomography

Cyt – Cytoplasmic domain

Peri – Periplasmic domain

SpoA – Surface presentation of antigen

FHA – Forkhead-associated

T4L – T4 Lysozyme

BACTH – Bacterial adenylate cyclase two-hybrid

BLI – Biolayer Interferometry

CD – Circular dichroism

NMR – Nuclear Magnetic Resonance

HSQC – Heteronuclear single quantum coherence spectroscopy

MS – Mass Spectrometry

SPI – Salmonella Pathogenicity Island